

9-16-2011

Characterization, modeling, and simulation of multiscale directed-assembly systems

Ryan Molecke

Follow this and additional works at: https://digitalrepository.unm.edu/nsms_etds

Recommended Citation

Molecke, Ryan. "Characterization, modeling, and simulation of multiscale directed-assembly systems." (2011).
https://digitalrepository.unm.edu/nsms_etds/2

This Dissertation is brought to you for free and open access by the Engineering ETDs at UNM Digital Repository. It has been accepted for inclusion in Nanoscience and Microsystems ETDs by an authorized administrator of UNM Digital Repository. For more information, please contact disc@unm.edu.

Ryan A. Molecke

Candidate

Nanoscience and Microsystems

Department

This dissertation is approved, and it is acceptable in quality and form for publication:

Approved by the Dissertation Committee:

C. Jeffrey Brinker, Ph.D.

Chairperson

Susan Atlas, Ph.D.

P. Randall Schunk, Ph.D.

Stanly Steinberg, Ph.D.

**CHARACTERIZATION, MODELING, AND SIMULATION OF
MULTISCALE DIRECTED-ASSEMBLY SYSTEMS**

BY

RYAN A. MOLECKE

Bachelor of Science in Computer Engineering

DISSERTATION

Submitted in Partial Fulfillment of the
Requirements for the Degree of

**Doctor of Philosophy
Nanoscience and Microsystems**

The University of New Mexico
Albuquerque, New Mexico

May, 2011

DEDICATION

In loving memory of my grandmother, Miriam, I dedicate this work to my niece,
Tigerlily Miriam, whose love has given me strength.

ACKNOWLEDGEMENTS

I would like to acknowledge my parents, who instilled me with a respect for nature, science, and a love for learning. My mother is a natural leader who sets goals most would never dream of and overcomes any obstacle to accomplish them. My father is a self-made and sincere man who followed his own path to become a world-class scientist through hard work and immense dedication. I will always strive to emulate them and to make them proud.

I would like to acknowledge my advisors, Dr.'s Stanly Steinberg, Susan Atlas, P. Randall Schunk, and C. Jeffrey Brinker, for their countless hours of mentoring and super-human patience. Their work is profound and important. They have challenged me with their sheer intelligence and shown me a higher level of research standards.

Finally, I would like to acknowledge my close friends, Raquel, Renée Garcia, Katrina, Ginger, Nick, Maximillian, and Renée Brown. Most of them probably belong in a mental institution, but I love them anyway. My brother Greg and his wife Lesley are OK too, I suppose. I acknowledge them begrudgingly, even though they are extremely annoying and they smell bad.

**CHARACTERIZATION, MODELING, AND SIMULATION OF
MULTISCALE DIRECTED-ASSEMBLY SYSTEMS**

BY

RYAN A. MOLECKE

Bachelor of Science in Computer Engineering

Doctor of Philosophy in Nanoscience and Microsystems

ABSTRACT OF DISSERTATION

Submitted in Partial Fulfillment of the
Requirements for the Degree of

**Doctor of Philosophy
Nanoscience and Microsystems**

The University of New Mexico
Albuquerque, New Mexico

May, 2011

**CHARACTERIZATION, MODELING, AND SIMULATION OF
MULTISCALE DIRECTED-ASSEMBLY SYSTEMS**

By

Ryan A. Molecke

**BACHELOR OF SCIENCE IN COMPUTER ENGINEERING
DOCTOR OF PHILOSOPHY IN NANOSCIENCE AND MICROSYSTEMS**

ABSTRACT

Nanoscience is a rapidly developing field at the nexus of all physical sciences which holds the potential for mankind to gain a new level of control of matter over matter and energy altogether. Directed-assembly is an emerging field within nanoscience in which non-equilibrium system dynamics are controlled to produce scalable, arbitrarily complex and interconnected multi-layered structures with custom chemical, biologically or environmentally-responsive, electronic, or optical properties. We construct mathematical models and interpret data from direct-assembly experiments via application and augmentation of classical and contemporary physics, biology, and chemistry methods.

Crystal growth, protein pathway mapping, LASER tweezers optical trapping, and colloid processing are areas of directed-assembly with established experimental techniques. We apply a custom set of characterization, modeling, and simulation techniques to experiments to each of these four areas. Many of these techniques can be

applied across several experimental areas within directed-assembly and to systems featuring multiscale system dynamics in general. We pay special attention to mathematical methods for bridging models of system dynamics across scale regimes, as they are particularly applicable and relevant to directed-assembly. We employ massively parallel simulations, enabled by custom software, to establish underlying system dynamics and develop new device production methods.

TABLE OF CONTENTS

<i>Chapter / Section Title</i>	<i>Page/s</i>
I Introduction, Background, Methods and Motivations	1 - 7
I.i Introduction and Background	1 - 4
I.ii Methods and Motivations	4 - 7
II Directed-Assembly of Crystal Growth	8 - 38
II.i Introduction to Directed-Assembly of Crystal Growth	8
II.ii Wulff's Construction of the Equilibrium Crystal Shape	8 - 14
II.iii Modeling Bounded Crystal Growth Via "Dynamic Wulff Progressions"	15 - 25
II.iv Atomic Models and Quantum Density Functional Theory of Crystals	25 - 29
II.v Simulation of the Evolution of Solvated Nanoparticle Morphology via Augmented Wulff Constructions and Bezier shapes	29 - 37
II.vi Summary on Directed-Assembly of Crystal Growth	38
III LASER Tweezers Optical Trapping	39 - 52
III.i Introduction to LASER Tweezers Optical Trapping	39 - 40
III.ii Force Measurement via Laser Tweezers Optical Trapping	40 - 50
III.iii Conclusions on LASER Tweezers Optical Trapping	50 - 52
IV Directed-Assembly of Nanoparticle Colloids	53 - 116
IV.i Introduction to Colloid Science: Methods and applications	53 - 61
IV.ii Soft-Particle Colloids: The Vincent Model	61 - 73
IV.iii Characterization Methods for Soft-Particle Colloids	74 - 85
IV.iv Interface-Driven Order in Soft-Particle Colloids	85 - 93
IV.v 2D Array Rearrangement using a Stimuli-Responsive Substrate	94 - 108
IV.vi Characterization of Binary Nanoparticle Superlattices	109 - 116
V Summary and Conclusion	117 - 118
V.i Summary	117
V.ii Conclusion	117 - 118
VI Bibliography	119 - 128
VII Appendices	129 - 168
(A) Cellspan: A Graphical User Interface to Protein-Pathway Mapping via Statistical Tests for Spatial Randomness	129 - 146
Appendix (B) Table of Contents	147
(B) LAMMPS software source code	147 - 168

Chapter I. Introduction, Background, Methods and Motivations

I. i. Introduction and Background

A new field of science is emerging around the idea that atoms, molecules and nanoscale particles can be controlled and directed across a *range* of scales to produce devices smaller than traditional lithography can achieve, all the way up to macroscale objects with nanoscale or better feature precision. The field of **multiscale directed-assembly** represents a fundamental advancement to manufacturing and information technology, resulting from generations of incremental advances and a modern fusion of the physical sciences. The applications and benefits of such technology could be limitless, and the implication is that mankind is reaching a new level of control over matter and energy altogether.

We investigate directed-assembly in three main technical areas: crystal growth, LASER tweezers optical trapping, and colloid processing. We find that statistical methods developed for studying protein interaction and chain-reaction “pathways”, a directed-assembly system seen in nature, can also be applied to colloid processing. The focus of the document is on characterization, modeling, and simulation methods which capture the multiscale nature of these systems and which can be applied across research disciplines, with the goal of defining and advancing the science of direct-assembly. We describe empirical, semi-empirical, and theoretical approaches to directed-assembly systems including experiments, laboratory techniques, and multiscale modeling and simulation methods.

Chapter II describes an extension of existing crystallographic theory to characterize, model, and simulate directed-assembly of crystal growth. First we describe how classical crystallographic theory and classical thermodynamics units can be applied

to model and meter crystals of any size or geometry. We then cover a method for augmenting classical crystallography theory, developed to model crystals grown in bounded conditions, which enables simulations of the evolution of crystal growth morphology and identification of surface energy values. We follow this up with a comparison to surface energy values calculated from first-principles using quantum density functional theory, with the goal of correlating data and creating a ‘mesoscale’ theoretical bridge between crystallography and quantum physics. Finally, we describe a method for extrapolating surface energy shape from equilibrium crystal shape which we use to simulate / investigate of the evolution of solvated nanoparticle morphology (a case of unbounded crystal growth).

Chapter III is a case study which uses modern mesoscale physics methods to characterize system dynamics in LASER tweezers optical trapping experiments. We describe the physical LASER tweezers optical trapping apparatus and associated software / hardware systems. We display examples of raw data and explain how it is processed to derive the positions of two interacting microscale particles, and subsequently the interparticle force. We then show how measurements of interparticle potentials from optical trapping experiments can be correlated to measurements of particle surface potential and fitted to modern mesoscale physical theory. We conclude with a critical analysis of the results, error approximation methods, and drawbacks of our experimental method and suggestions for improving future results.

Chapter IV describes the application of modern rheological and mesoscale particle theory for the characterization, modeling, and simulation of directed-assembly of nanoparticle colloids. We describe modern polymer-solvent theory for soft-particle

colloid interparticle interaction potentials, and we implement this theory as software code in a simulation engine to verify our model, match simulations to experiment, and identify underlying colloid system dynamics. Two experiments are discussed in separate sections. The first experiment uses evaporation-induced self-assembly (EISA) to create a free-standing, transferable film of hexagonally-packed nanoparticles at a solvent-air interface. We characterize the EISA process via analysis of Fourier transforms and X-ray spectrographic signatures of simulations and experiment to show that the solvent-air interface is the driving / dominant force interaction in the system. The second experiment starts with the same evaporation process but also includes a subsequent irradiation step which causes the film to retract from a coverslip edge and the nanoparticles in the film to coalesce into nanorods. We apply custom software methods to tune simulations of irradiation of the film and generation of nanorod structures to experiment and capture the essential physical attributes of the system. Finally, we demonstrate how simulated X-ray spectroscopy and Fourier transforms can be valuable in verifying the geometry and structure of binary nanoparticle superlattices formed by directed-assembly of colloid processing.

At first glance the topics of crystal growth and colloid processing may seem unrelated, but they are actually representative technologies, in their respective fields, of the emerging science of multiscale directed-assembly. Directed-assembly systems feature not only scalability, but distinctly multiscale physical processes which control the system dynamics. In both crystal growth and colloid processing, there is an extreme of scale between the physical dynamics underlying the system (or controllable experimental parameters) and the devices to be produced. Controlling quantum dot and nanocrystal

shape, in the present case via selective plasma-enhanced chemical vapor deposition (PECVD) onto interferometrically patterned substrates, is a promising area of solid-state physics with applications in photonics^{1,2}, computing³⁻⁶, and solar energy⁷. Colloid processing is an established industry which continues to evolve with modern advances in nanoparticle production⁸⁻¹⁰, active biopolymer coatings¹¹⁻¹⁵, sol-gels^{16,17}, evaporative self-induced assembly^{18,19}, new theoretical paradigms²⁰, and exponentially growing computational resources available for simulations and modeling²¹.

I. ii. Methods and Motivations

In this section the two topics of crystal growth and colloid processing are broken down into a summary of controllable effects, assembly direction methods, and verification methods between experiment, models, and calculations or simulations. The term “mesoscopic physics” is a relatively new and apt jargon for the methods used in multiscale directed-assembly. The McGraw-Hill Dictionary of Scientific and Technical Terms defines **mesoscopic physics** in the following way:

A sub-discipline of condensed matter physics focusing on the properties of solids in the intermediate range between atoms or molecules and bulk materials. Generally, systems with dimensions on the order of 100nm are studied, and the field has primarily dealt with artificial structures of metals and semiconductors.

Additionally, the mesoscale is one which *bridges* two or more magnitudes of scale, and the study of molecular biological systems has also been included in recent years. A common theme of “bottom-up” design in mesoscopic physics, i.e. controlling small-scale dynamics to produce larger scale devices, is mirrored within the fields of crystallography and colloid science. Directed-assembly is a bottom-up manufacturing method in which

non-equilibrium system dynamics are controlled for the fabrication of structures not accessible by other means. A central concept in multiscale directed-assembly is the idea of overcoming natural ordering or affecting local entropy to produce ordered structures which can be scalable over several orders of magnitude (from nanoscale to macroscale), produced in parallel, and connected to macroscale outputs or effects.

In the case of crystal growth and design, ordered structures are formed through bounding geometries, plasma effects and beam orientation with respect to an underlying atomic crystal lattice orientation. Recent publications also demonstrate crystal growth enhancement using vapor-liquid-solid interface effects²². The underlying characteristic being controlled in these experiments is the *surface energy* of the crystal facets, which is a function of atomic lattice and facet orientations and molecular orbital energies based on elemental composition. We describe how a classical crystallographic theory, Wulff's constructions for equilibrium crystal shape²³, can be augmented to account for non-equilibrium effects and even enable predictive modeling of crystal growth. We describe a new spatial algorithm for defining the surface energy shape of any crystal, a central concept in the classical Wulff theory never before modeled or visualized in a scientific way. We demonstrate several new modeling techniques for performing mathematical progressions or "evolutions" of spatial coordinate sets to describe the morphology of anisotropic crystal growth in both bounded and unbounded systems. The Wulff theory fits our definition of a "mesoscopic" model and is easily scalable to microscopic / macroscopic dimensions since we do not explicitly account for individual atomic effects.

In quantum physics, the principle of correspondence²⁴ states that quantum physics should reduce to classical (macroscale) physics in the limit of large numbers of particles

in the system. This can be viewed as a classical description of mesoscale physics, and applied to all mesoscale models by pursuing models which smoothly link physical descriptions of systems across scale and those which are inherently scale-invariant. For completeness, and to satisfy the principle of correspondence, we pursue a mathematical or physical model linking Wulff theory down to the smaller scales at which molecular, atomic, and subatomic particle (quantum) physics cannot be ignored. In this pursuit, we compare and correlate results from modern quantum density functional theory²⁵ (QDFT) calculations and experiment to simulations based on augmented Wulff theory²⁶, and describe a method for linking Wulff equilibrium crystal shapes and surface energy shapes to theorized chemical properties and the toxicology of nanoparticles.

In the case of directed-assembly via colloid processing, ordered structures are formed through evaporative, vapor-liquid-solid (VLS) interface dynamics, polymer/solvent interactions, and shear or irradiation (physical deformations). We describe methods for applying classical Derjaguin-Landau-Verwey-Overbeek (DLVO)^{27,28} potentials, fast-lubrication dynamics²⁹, and Newtonian multi-body physics to correlate models / simulations to experiments in laser tweezers optical trapping systems and directed-assembly via colloid processing. We discuss statistical methods for analyzing multi-particle systems and error quantification in measurements, as it relates to laser tweezers optical trapping systems. As in the crystal case, where we pursue linkages between the smaller-scale molecular chemistry / quantum physics and the larger-scale mesoscopic Wulff theory, in colloids we attempt to characterize how the smaller-scale individual particle properties can effect and determine the larger-scale dynamics of the colloid system as a whole. A running emphasis on multiscale techniques reflects the

nature of directed-assembly systems as we develop a description of the essentials of directed-assembly in crystallography and colloid science.

Chapter II. Directed-Assembly of Crystal Growth

II. i. Introduction to Directed-Assembly of Crystal Growth

The ability to control the evolution of morphology during crystal growth and direct the final shape of crystals is a research topic with the potential to fundamentally alter production methods and augment the capabilities of opto-electronic / photonic devices. By augmenting classical theory, we can visualize and simulate evolutions of crystal morphology in both bounded and unbounded crystal growth systems, investigate the underlying system dynamics, and establish new avenues for device production. As a case study of bounded crystal growth, we investigate the experimental system of GaAs nanopillars and nanopyramids formed by selective plasma-enhanced chemical-vapor deposition (PECVD) onto patterned GaAs substrates. As a case study of the unbounded case, we describe a new method for visualizing surface energy shapes and show that it can be applied to the characterization and simulation of evolution of morphology in solvated nanoparticle growth. By characterizing evolution of morphology of solvated nanoparticles, we show that Wulff theory can be useful in predicting the toxicology of nanoparticles.

II. ii. Wulff's Construction of the Equilibrium Crystal Shape

In this section, we describe the classical Wulff's construction for equilibrium crystal growth. This sets up a mathematical basis for later sections in which we augment and functionalize Wulff's constructions in order to characterize, model, and simulate directed-assembly of crystal growth in the bounded and unbounded cases. Visualizations of Platonic, Archimedean, and related crystal shapes and associated surface energy shapes are included.

Wulff's classical theory is a (static) energy minimization algorithm which yields the lowest energy crystal shape defined relative to an outer surface energy shape which is governed by reconstructed atomic lattice surface energies and unique to a given chemical composition. The surface energy at angle θ , $\gamma(\theta)$, is related to the expected crystal shape by the following equation³⁰:

$$W = \left\{ x \in R^d : x \cdot \theta_u \leq \gamma(\theta), \forall \theta_u \in S^{d-1} \right\} \quad (\text{The Wulff Shape}) \quad (2.1)$$

where θ_u is a unit vector in the θ direction, R^d is the real domain of d dimensions containing all vectors x , and S^{d-1} refers to a surface in polar ($d=2$) or spherical ($d=3$) coordinates. Wulff shapes represent the minimal surface energy orientation for a crystal of a given volume, or equilibrium crystal shape (ECS)²³. The Wulff shape is the convex inner shape bounded by all tangents to an outer surface energy shape (SES). While a single, convex inner ECS is implied by a given SES, there are an infinite number of SES shapes that can correspond to any ECS shape, i.e. the Wulff construction represents an irreflexive, geometric set relation.

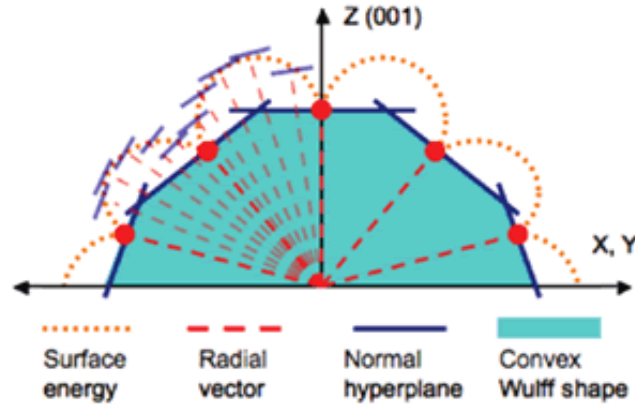


Figure 1.1) Geometric construction of the Wulff shape based on anisotropic surface energy shape.

Figure 1.1 is a schematic drawing in 2D of an arbitrary SES, the tangent vectors to that shape, and the convex ECS formed by minimization of all the tangent vectors. The blue convex shape is the crystal shape that an element is expected to form when grown under equilibrium conditions, i.e. faceting is determined completely by the surface energy

ratios of the facets and not affected by limited surface transport of adatoms. Figure 1.2 is a computer-generated mapping of the ECS of a cube and a corresponding SES shape in 3D, using software developed in the MATLAB programming language by Ryan Molecke (detailed in section I.iii). The outer SES shape is ‘false-colored’ according to the facet orientation energy (red

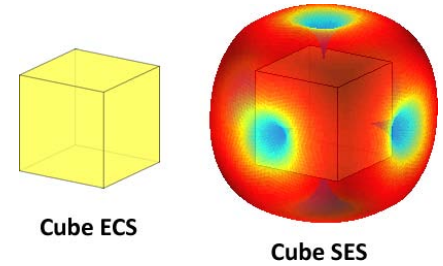


Figure 1.2) Cube equilibrium crystal shape (left) and a corresponding surface energy shape (right) with transparency so that the inner ECS cube can be seen within the SES shape

being higher energy, and blue being lower energy facet orientations), and displayed with transparency so that the inner ECS shape can be seen within. The blue funnel shapes pointing inwards towards the facets indicate minima in the SES corresponding to facets in the ECS, and the red regions indicate high-energy orientations in the SES where facets are excluded from forming in the ECS. This (figure 1.2) demonstrates just one of an infinite number of possible SES shape mappings to the given cube ECS shape, designed for clarity in demonstrating the geometric relationship between SES/ECS and for visual appeal.

To further illustrate the Wulff constructions and the relationship between ECS and SES, Figure 1.3 is a visual 3D catalog of Platonic / Archimedean / related polyhedral crystal shapes and corresponding surface energy shapes. Using the conventional Miller index notation, facets with (001), (011), and (111) orientations and tetrahedral symmetry are displayed in yellow; those with icosahedral symmetry are displayed in blue. Notable shapes include the Buckminster fuller (cuboctahedron), and Buckminsterfullerene (regular truncated icosidodecahedron), the latter of which is the known shape of the C60

“Bucky ball” molecule. The blue icosahedral shapes are common among virii, while the simpler cube, tetrahedron, and octahedron are observed in solvated nanoparticle growth. A ‘semiconductor’ shape is included which features (113)-indexed facets with tetrahedral symmetry, shown in green (see next page)

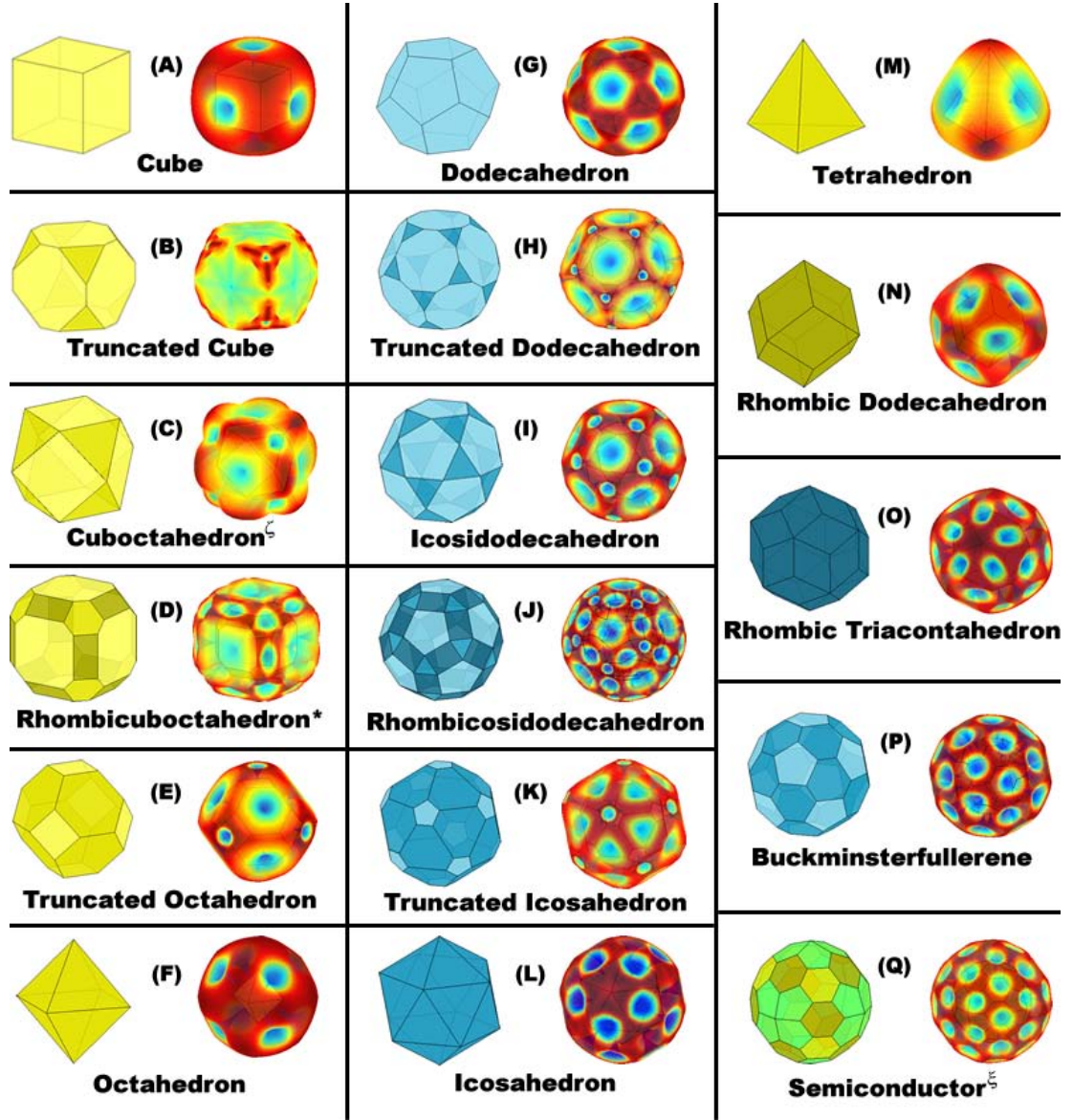


Figure 1.3) Visual catalog of Platonic polyhedra (A,F,G,H,M), Archimedean polyhedra (B,C,E,G,H,I,J,P), and related polyhedra (D,K,N,O), and a regular “semiconductor” polyhedra featuring (113)-indexed facets with tetrahedral symmetry. To the right of each polyhedron, a corresponding surface energy shape is displayed.

The (113)-indexed facets correspond to the orientations of energy minima theorized to exist in the surface energy shape for semiconductor crystals, based on analysis in the next section.

Wulff constructions are the standard basis for theoretical and computer models involving crystal faceting during equilibrated crystal growth, and can even be linked to mathematical systems for describing phase equilibria and solution thermodynamics. The NIST software project WULFFMAN is an example of the application of the Wulff constructions to visualize crystal shapes. In 1995, Cahn et al. showed that the Wulff construction can be written in parallel form to the tangent construction on the molar Gibbs free energy, and demonstrated a means to apply solution thermodynamic units to crystal shapes. We define a very similar system for applying standard units / metrics to Wulff shapes. The total surface energy, γ , of a Wulff ECS or SES shape is the sum of the surface energies of the facets:

$$\gamma = \sum_{i=1}^n \gamma(f_i) \quad (2.2)$$

for n facets. In the case of the SES shape, which is a curved, not faceted shape, the SES can be thought of as broken into i discrete facets approximating the shape. The surface energy of a facet, $\gamma(f_\theta)$, is the area of the facet, $a(f_\theta)$, times the energy associated with the facet's orientation, $\gamma(\theta)$, from the surface energy shape, where θ is the direction of a unit normal to the facet surface. The energy associated with a facet orientation, $\gamma(\theta)$, can be set equal in magnitude to the distance from the facet to the center of the crystal, $d(f_\theta)$, since the energy ratios among facet orientations, $R(\gamma(\theta))$, in the SES is the same as the length ratios among distances from the origin to the facets in the ECS, $R(d(f_\theta))$:

$$R(\gamma(\theta)) = \left\{ \gamma(\theta_i) / \gamma(\theta_j) \forall i \neq j, 1 \leq i \leq n, 1 \leq j \leq n \right\} \quad (2.3)$$

$$R(d(f_\theta)) = \left\{ d(f_i) / d(f_j) \forall i \neq j, 1 \leq i \leq n, 1 \leq j \leq n \right\} \quad (2.4)$$

Then:

$$\gamma(\theta) \equiv d(f_\theta) \quad (2.5)$$

The molal energy of an ECS or SES shape, $G(S^m)$, can be defined as the surface energy of the crystal over the surface area:

$$G(S^m) \equiv \gamma / \sum_{i=1}^n a(f_i) \quad (2.6)$$

using Eq. 2.5 for the surface energy terms. A Euclimolar, or “free energy” of the crystal, $G(W^{Eu})$, is then defined as the molal energy evaluated on a unit sphere:

$$G(S^{Eu}) = G(S^m) / (\sum_{i=1}^n d(f_i)^2)^{1/2} \quad (2.7)$$

These metrics are useful for comparisons to crystal surface energies calculated from first-principles and for studying the growth thermodynamics and toxicology of nanoparticles, which will be topics of discussion in the next two sections. The Wulff constructions and ECS / SES shapes will be a basis for studying the evolution of morphology in bounded growth of nano-pyramids/pillars and the unbounded growth of solvated nanoparticles. Many of the crystal shapes displayed in this chapter have direct analogues among nanoparticles formed using colloid processing, because the geometries depend on similar geometric space-filling properties which are invariant over scale. The Wulff constructions represent a theoretical “stepping stone” to studying crystallographic systems and a tool in the industry of directed-assembly which exhibits the signature feature of scalability.

II. iii. Modeling Bounded Crystal Growth via “Dynamic Wulff Progressions”

In this section we describe an augmentation to the Wulff constructions and its application to characterize, model, and simulate directed-assembly of crystal growth in the case of bounded crystal growth. We describe a functionalization of the Wulff theorem which enables full simulation of the evolution of nanopillar and nanopillar crystal growth and the identification of anisotropic surface energies. A semi-empirical fitting process is used, as we fit energy ratios from augmented Wulff theory to TEM images of nanocrystals grown by selective PECVD of GaAs onto patterned GaAs substrates. This process elucidates the effect of bounding on evolution of nanocrystal morphology. This augmentation to the Wulff theory is also applicable for determining surface energy values which are difficult to obtain in any other way and useful in the manufacturing of optoelectronics and photonics devices.

Selective area growth of quantum dots (QDs) on nanopatterned substrates have recently drawn much scientific attention due to the extensive application potential in nanoscale electronic, optoelectronic, and photonic devices³¹⁻³⁷. These applications take advantage of quantum electronic and optical behavior in nanopillars and nanopillars formed by PECVD of GaAs with controlled size, dimension, and lithographic integration onto masked GaAs (001) substrates with nanopatterned openings. In the formation of these pyramidal structures under a certain set of growth conditions, an equilibrium crystal shape (ECS) will be assumed, which is determined by minimum surface free energy and thermodynamic equilibrium stability by atomic reconstruction and faceting in the microscopic scale^{38,39}. Nanocrystal growth by selective area PECVD is an example of multiscale directed-assembly, referred to as ‘bounded’ evolution of nanocrystal

morphology since the crystal geometries evolve as the crystals grow on a plane and in a circular bounding well formed in interferometric-lithography patterned SiO_2 on the surface of the GaAs substrate.

Classical Wulff theory of static equilibrium crystal shapes can be augmented to provide a theoretical model to explain observed evolutions of bounded nanocrystal morphology. By adding the concept of *effective* versus *final* surface energy for any facet, and extending Wulff's theorem with a new dynamic geometric construction (by Ryan Molecke), we can simulate entire evolutions of crystal shape which closely match observed bounded crystal growth, given only a list of minima (in the surface energy shape) and the epitaxy beam direction. By allowing the surface energies of the facets to change over according to a given function, $F(\gamma(f_\theta))$, we can model observed evolution in nanocrystal morphology during growth / equilibration. We show that this method can be used as a tool for empirically estimating surface energies that are otherwise extremely difficult to determine. We demonstrate models of static shapes and simulations of the evolution of morphology in nano-pyramids/pillars using classical and augmented Wulff theory, and compare our empirically estimated surface energies to energy calculations from first-principles QDFT calculations for verification.

In experiments performed by Ping-Show Wong at the UNM Center for High Technology Materials²⁶, GaAs nanopyramids and nanopillars were grown by selective area epitaxy onto nano-patterned GaAs substrate and characterized by scanning electron microscope, shown in Figure 1.4. The nanopyramid images (right) shows an evolution in shape between lesser-formed pyramids that received a lower density of adatoms from the epitaxy beam (center of beam) to fully formed pyramids in areas that received a higher

density of adatoms from the beam (edge of beam). Once the pyramids reached the final shapes seen in the bottom row (edge of beam images), further exposure to the beam no longer produced any noticeable change in nanopyrnmid geometry. Since these nanopyrnmidns are grown in temperatures higher than the annealing point of GaAs (annealing at 600-800° C, experiment at approximately 1300° C), and since adatoms are being energetically projected towards the growth planes of the crystals (in an As-rich environment), the crystal structures are small enough that the facet formation is theorized to not be limited by adatom mobility. This means these final (edge of beam) crystal shapes are the equilibrium crystal shapes for GaAs, determined only by the lattice anisotropic surface energy shape and boundary conditions, according to the Wulff construction theory. Equilibrium crystal

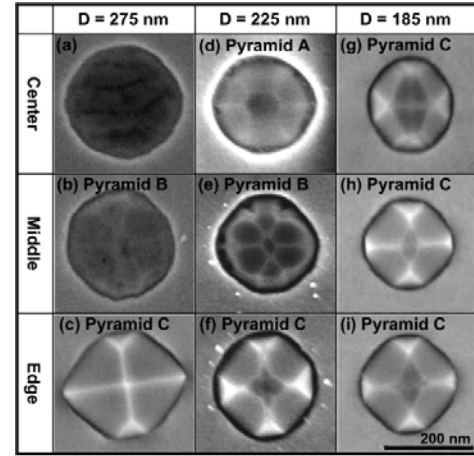


Figure 1.4) Nanopyramids produced by covering a (001) substrate of GaAs with a 25nm layer of SiO₂ by dielectric evaporation. Circular holes were patterned into the SiO₂ layer using interference photolithography by literature methods¹⁹. The SiO₂ patterned was etched with CHF₃ by reactive ion etch for four minutes. The patterned substrate was placed in a Thomas Swan vertical MOCVD chamber using a 12.5 V/III ratio (As/Ga) in 1 Å/s planar growth mode for 10 seconds. Images produced by SEM.

growth, however, is actually rare except in very small particles and hard to achieve experimentally because surface transport of matter must be artificially facilitated for the lowest energy atomic surface orientations to be reached⁴⁰. However, high-temperature growth conditions and extremely small crystal size are ideal conditions for equilibrated crystal growth⁴¹, and this is aided by the fact that semiconductors are known to

aggressively trade energy gained in bond formation with energy lost in elastic distortion in search of the lowest free energy geometrical configuration⁴².

We model evolution of Wulff shapes using custom software with 3D visualization tools written in the MATLAB language⁴³. A program generates 3D multifaceted objects using a list of facet indices and correlated surface energies, by performing a vertex minimization and convex-shape construction algorithm. The surface energies are adjusted accordingly for fitting after being visually compared to the experimentally observed bounded crystal shapes A, B, and C.

The best-fitted simulation results are shown in Figure 1.5. The simulated Wulff pyramids, Figure 1.5a-c in bird-eye view and plan-view, strongly resemble the GaAs ECS in the SEM images, Figure 1.4a-c. The small discrepancies in the shape and size of the facets near the edge of circular openings might come from the deviation of the GaAs pyramids from the optimal equilibrium crystal epitaxial growth conditions due to the existence of boundary conditions, including the SiO₂ mask and the GaAs substrate.

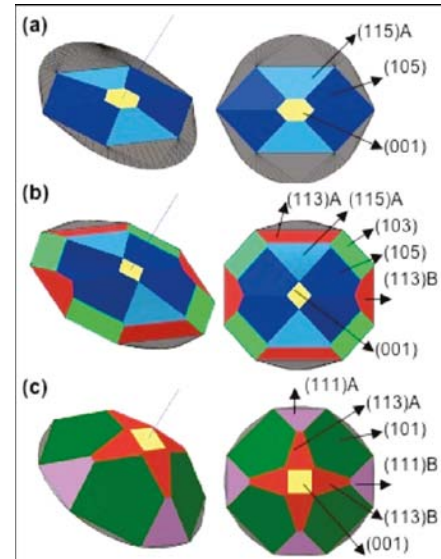


Figure 1.5) Simulations of Wulff-fit pyramid shapes. The facet indices are expressed by plane family in Miller index format. A/B designations indicate complementary plane alignments within a family, i.e. a Miller index has been switched in order not just in sign, so (113)B is a [131] or [311] group plane.

Each static model yields a set of facet surface energies relative to the top (001) facet for pyramids A, B, and C. The static models illustrate that the {10n} and {11n} facets gradually progress to become dominant,

while $\{103\}$ facets gradually regress and disappear from the crystal shape as the ECS evolves from Pyramid B to Pyramid C. The surface energies of ECS facets, including the (001) plane, may change when formed under different growth environments or with different neighboring facets. This indicates that the relative anisotropic surface energy function can be different for various stages of the ECS evolution, and also suggests that the surface bonding and the atomic surface dynamics of a certain nano-facet may change in the continuous epitaxial process. The Wulff constructions thus provide a computational tool to study the GaAs ECS facet surface energy hierarchy and the surface dynamics.

By fitting crystal shapes to observed nanopyramid morphologies over their growth periods, we obtain sets of surface energy values which depend on beam orientation and which change over a crystal's growth progress. A functionalization of the Wulff constructions for ECS enables full simulations of the evolution of nanocrystal morphologies and empirical fitting to the observed dynamics of surface energy and crystal morphology. This augmentation of Wulff's theorem (Eq. 2.1) links the orientation of a facet surface (with respect to the substrate normal / beam direction) to its surface energy growth rate over a period of growth progress, p .

$$\gamma(f_\theta)_{eff} \equiv F(\gamma(f_\theta)) = |\bar{n} - \bar{l}(1-p)| = |\bar{v}| \quad (2.8)$$

For (growth progress) $p : 0 \rightarrow 1$

Figure 1.6 is a schematic of the geometric construction described by Eq. 2.8. The *effective* surface energy, $\gamma(f_\theta)_{eff}$, is the energy that a facet displays at any given amount of progress, and the rate of effective surface energy growth is a linear function of facet angle to the beam. The effective surface energies grow until they reach their final values, $\gamma(f_\theta)$, corresponding to the ratios measured for the “final shape” shown in Figure 1.4 (pyramid C). This results in an accurate model of the evolution of crystal shape, concluding with the final shape posited to correspond to the equilibrium crystal shape for GaAs given our growth conditions.

The “bounded crystal growth function” (eq. 1.8) can be used to estimate actual anisotropic surface energies by fitting to observation, which are difficult to obtain experimentally (via crystal fracture), or theoretically (via first-principles calculation). This model can be also used to predict the evolution of surface shapes in bounded crystal growth,

which makes it a unique and potentially very powerful tool for device design based on custom-shaped crystal growth.

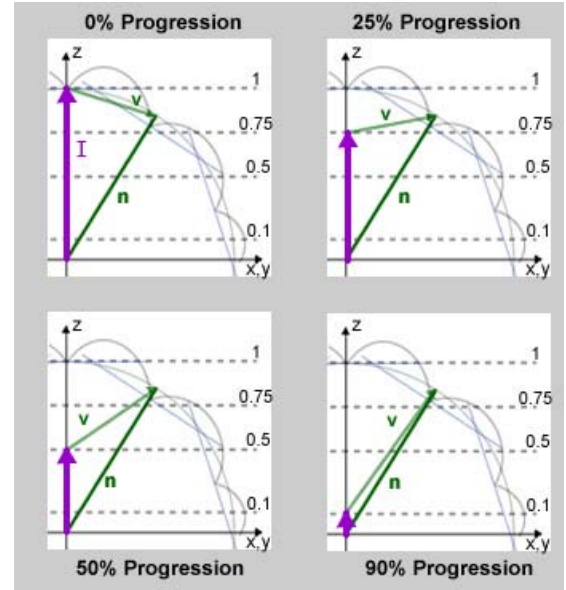


Figure 1.6) Geometry of equation 1.8.

\bar{n} represents a unit vector in the θ direction, \bar{I} represents a unit vector in the growth direction, which contracts from length 1 to length 0, and \bar{v} represents the vector formed by subtracting \bar{I} from \bar{n} . The length $|\bar{v}|$ is a fraction by which a given surface energy $\gamma(f_\theta)$ is scaled, which grows to 1 as the progression completes. The outer blue arcs are the surface energy shape and the straight blue lines outline the inner equilibrium crystal shape.

A 3D plot, Figure 1.7, can be constructed showing a surface representation of Eq. 2.8. The dotted lines represent the experimental data: facet energy values at each stage of growth progress from fitted SEM images of the nanopylramids in terms of effective versus final observed energy value per facet. A close correspondence (less than 5% overall average error) between the actual fitted values and theory values is found.

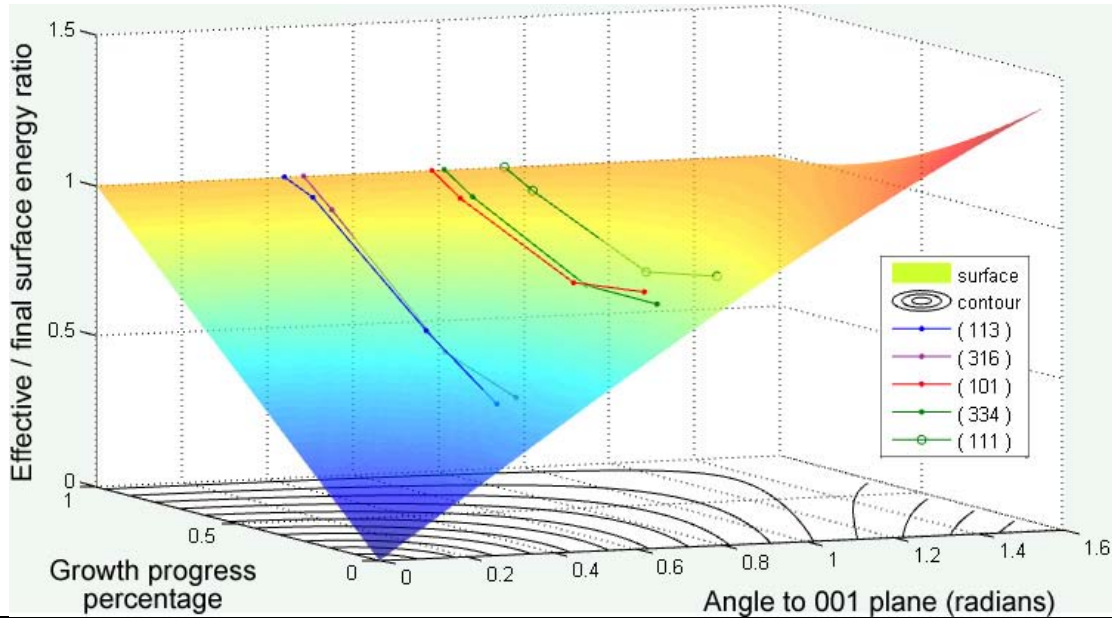


Figure 1.7) Observed surface energy ratios for crystal fit (to Fig. 1), plotted against surface energy ratios predicted by the Wulff progression equation. Note that 1.6 radians is 90 degrees, so this graph covers the entire space of facet orientations (facet orientations facing directly into the beam through facet orientations facing perpendicular to the beam).

Using Eq. 2.8, full animations of crystal growth can be generated from only a set of energy minima and the beam direction. The animation is generated by calculating / displaying the Wulff shapes described by the effective surface energies across intervals of the progress variable, and saving the images as sequential frames of a movie (using MATLAB software by Ryan Molecke, see Appendix A). Frames from such an animation are shown in Figure 1.8. The accuracy of Eq. 2.8 and validity of the fitted minima in the GaAs surface energy shape are demonstrated by how closely the animations resemble the

actual evolution of shape during crystal growth shown in the SEM images. This dynamic simulation of the ECS shows how the evolution of ECS morphologies is linked to the evolution of effective surface energies during nanocrystal growth. Eq. 2.8 is also versatile and modifiable in the sense that it can also be applied to model nanopillar growth.

Nanopillars over 1 μ m in length (6:1 aspect ratio) were demonstrated in Wong's growth experiments. The shape of the anisotropic surface energy of GaAs is such that there is a strong minima along the (111) direction, so that if the substrate and beam are aligned to (111), pillars will be produced instead of pyramids because the neighboring facet energies will never be low enough to "pinch off" growth of the top facet. Figure 1.9 shows the SEM images and Wulff shape models of nanopillars

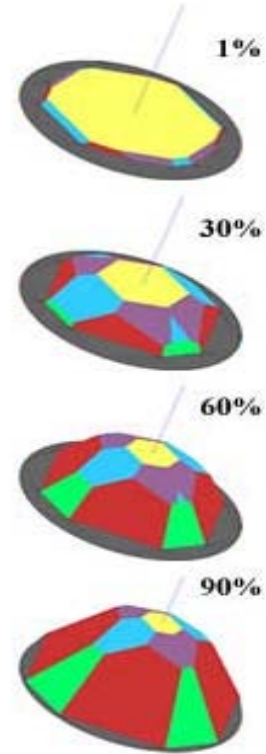


Figure 1.8) Frames from a crystal growth animation based on equation 1.8, fitted to resemble shapes from Fig. 1.4 as closely as possible. Frames are rendered at indicated percentages of growth progress towards the final shape (Fig. 1.4 pyramid C)

grown in a similar fashion to the above nanopyramids (except the substrate / beam direction was $\langle 111 \rangle$ in this case). This requires not only updating the surface energy ratios and beam direction (the input values), but also a modification to the MATLAB software so that the crystal pillar shape can continue to elongate even after the equilibrium crystal shape has been reached (the end shape is no longer changing). By allowing the final nanopillar "head" shape to move upward upon the side plane "stalks"

after it is fully formed, a growth animation from a flat to a pillar of arbitrary length can be produced.

The close correspondence between our animations of the evolution of crystal

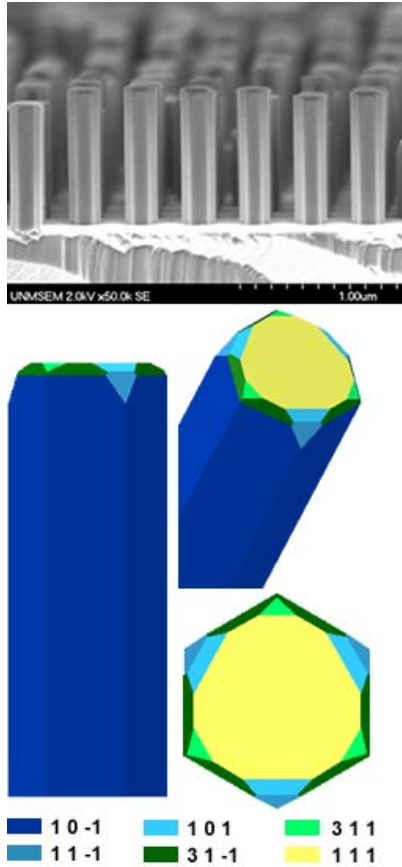


Figure 1.9) Observed SEM vs. Wulff-fit nanopillar shapes. In this example, the modeled pillar-like crystal shown includes facets observed among several nanopyramids and nanopillars of different heights grown on (111) substrate. Planes and key colored by Miller index family.

morphology and the observed evolution of morphology in these two examples may be used as the basis for a method of determining the actual surface energy shape for GaAs, including minima that may not appear in the final crystal shape. By using the final observed surface energy value of the beam-aligned facet as a key for the energy ratios in the Wulff construction, we can estimate the surface energy values of the crystal facets from the observed evolution of shape in the SEM images (Figure 1.4 a-c). Table 1 lists the orientation and energy ratios of the minima in the anisotropic energy shape of GaAs derived from our models.

Table 1: Comparison of Wulff-theory Surface Energy Estimation to QDFT calculation

	Miller Index	θ <i>angle to growth plane</i>	fitted $\gamma(\theta) / \gamma(001)$ <i>energy ratio</i>	fitted $\gamma(\theta) / \gamma(111)$ <i>energy ratio</i>	Estimated value: $\gamma(\theta)$ (present case) (meV/Å ²)	From QDFT calculations: $\gamma(\theta)^{38}$ (meV/Å ²)
(001) substrate nano- pyramid models	001	0	1		65*	≈ 65
	113	25.24	0.958		62.27	
	316	27.79	0.958		62.27	
	101	45	0.909		59.09	52 – 57
	334	46.69	1.018		66.17	
	111	54.74	1.018		66.17	51 – 63, ≈ 90
(111) substrate nano- pillar models	113	29.50		1.34	72.68	
	101	35.26		1.32	72.17	52 – 57
	-113	58.52		1.3	70.51	
	11-1	70.53		1.22	66.17	51 – 63, ≈ 90
	10-1	90		1	(NA)	52 – 57

* Key value taken from reference 34

Final surface energy ratios correlate well with the values of for (001) and (111) surfaces determined from first-principles by Moll, et al³⁸., although the crystal shapes differ from their calculated ECS for GaAs, likely because we took into account more anisotropic surface energy minima (minima in more directions) than their model accounted for. The nanopillar models show higher predictions for actual surface energies along the (101) and (113) facets, meaning those facets get less of a chance to grow when they are neighboring a (111) growing plane than when they are neighboring a (001) growing plane. This suggests that neighboring growing planes with strong surface energy minima can have an effect on relative surface energies. In effect, since the planes grow in proportions to their energies, the lowering of the (111) effective energy causes nearly aligned facets to have inflated effective energies. The actual energies predicted by the present nanopyramid models are thus expected to be more accurate.

A major advantage of using Eq. 1.8 over static Wulff shape theory is that the actual surface energies for facets can be (speculatively) determined even if that facet does not occur in the final growth shape. In the case of the nanopillar growth, the structures form somewhat non-uniformly until they reach high aspect ratios, and the top ring of facets is very fine and difficult to capture with SEM imaging. The dynamic model was able to predict the final nanopillar “head” morphology based on known surface energy value ratios, even though they were not clear in the SEM images. In conclusion, we demonstrate an advanced simulation and surface energy fitting of GaAs nanopyramids and nanopillars on nanopatterned GaAs substrates grown with varying pattern diameters and growth conditions, including the growth time and the growth rate. The ECS growth variation from the center to the edge region of the sample due to adatom diffusion is observed and explained. Across different regions of all samples under varying growth environments, three distinct types of GaAs ECS are identified, and they are defined by crystal plane families including $\{11n\}$, $\{10n\}$, and (001) . The simulation results based on Wulff’s theory show close similarity with the observed ECS and successfully demonstrate the dynamic evolution of these GaAs ECS. These experimental data and theoretical simulation results have thus laid the fundamental groundwork in understanding the formation mechanism of GaAs pyramidal and pillar ECS and the subsequent controlled nucleation of crystals on nanopatterned substrates.

II. iv. Atomic Models and Quantum Density Functional Theory of Crystals

In order to fully understand the dynamics of crystal growth and the effects of changing surface energies, the chemical bonding and surface reconstructions within the crystal lattice must be described at the atomic level. This will allow a full set of first-

principles surface energy values (for the far right column of Table 1) to be calculated and compared to the experimentally fit and Wulff's theory values. A novel and efficient method for building lattice atomic models is proposed, which has several specific advantages over classical atomic lattice models for zinc-blende structures in particular, and can also be applied to any crystal lattice geometry in a general way. In this approach, GaAs atomic crystal lattices are cut into periodic boxes along a given surface and QDFT methods are applied to determine the surface energy difference between the bulk and the cut box structure, which is posited to closely correspond to the actual surface energy. Tying together the experimental data fit from SEM images, the mesoscale simulations, and the atomic lattice QDFT results would be considered a multiscale bridging of the mesoscale Wulff theory to the smaller scale of molecules and atomic lattice geometries, and thus increase the applicability of the Wulff theorem in directed-assembly.

The traditional model shown in many textbooks for a GaAs (or any generic) crystal zinc-blende structure is shown in Figure 1.10. There are several problems with this image. First, there are unequal numbers of Ga and As atoms in the image, requiring that one count fractional atoms to determine that there are actually the same number of Ga and As atoms in the structure. Second, if this box is periodically repeated in 3D using these atomic coordinates, one must remove atoms on the edges (the fractional atom problem again, now in a different form). Finally, it is not clear from the image that every Ga atom is attached to 4 As atoms, and vice versa, in a (hextetrahedral) regularly-spaced and oriented manner.

The problems addressed in the classical model can be fixed by translating the classic 2-atom basis in face-center cubic (F43M) for zinc-blende structures into an 8-atom basis in the simple cubic system (PM3M). The resulting 8-atom basis is shown in Figure 1.11. This basis structure for GaAs more clearly shows the linkage geometry with equal atoms, and can be periodically repeated in all 3 (shown in Figure 1.12) directions with perfect tessellation. All bond lengths, bond angles and dihedrals are included in the structure in a minimal fashion, but this is specific to the zinc-blend system. Other crystal structures can be modeled by changing their basis number and translating to a set of orthogonal basis vectors, but the advantages are not as clear with other structures. This was performed for the body-centered cubic (Im3m) and α -quartz (P3₂21) crystal structures, for verification (not shown) using ‘crystal’, a shell sub-program in the TINKER molecular modeling package.

Large cube structures (10x10x10 basis cells) were constructed and cut along relevant surface planes to simulate large periodic surfaces of GaAs, (example surface shown in Figure 1.12). These

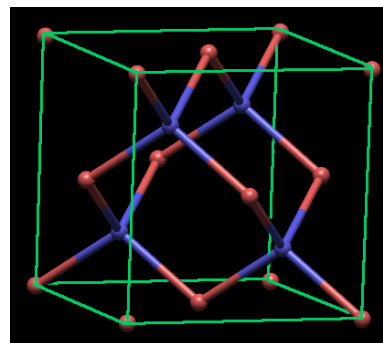


Figure 1.10) Traditional model of a zinc-blende crystal lattice basis cell

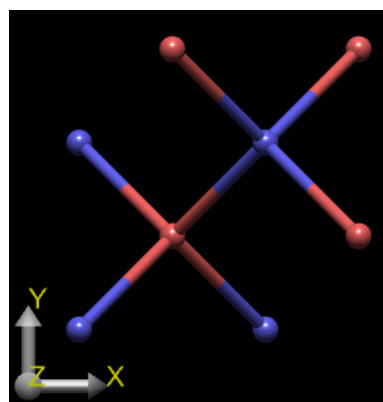


Figure 1.11) new 8-atom basis for zinc-blende structures, translated to simple cubic.

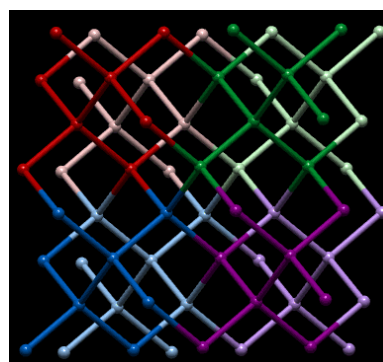


Figure 1.12) 8 instances of the basis structure (fig 9), colored, repeated in space, and linked together.

surfaces are cut again to form smaller periodic units which extend 6 to 8 layers into the substrate, and these smaller periodic boxes are used as the first input structures for the QDFT surface energy calculations. The periodic surface wedges built in this manner can be placed into similarly-shaped periodic boxes (with one elongated side) so that there are at least 4 lattice lengths of free space between opposing

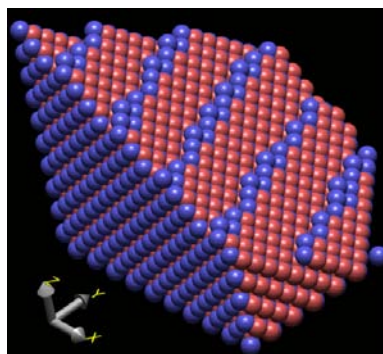


Figure 1.12) Large GaAs cube cut along the 457 plane reveals an interesting periodic zig-zag groove pattern on the surface

surfaces in the geometry minimization step of a QDFT surface energy calculation. Geometry minimization is performed on this periodic, cut structure (and on the bulk lattice structure), and the difference in total atomic energy between the bulk and cut surface structures (over the periodic surface area) is regarded as the surface energy. Literature examples add pseudohydrogens to one of the cut surfaces (which can help restore the condition of all As atom valence shells filled and all Ga atom valence shells empty, and thus maintain the electrical properties of a semi-conductor) and selectively freezing atoms in place^{44,45}. Pseudohydrogens cannot be added to the more exotic surfaces yielded from cutting higher-indexed planes into GaAs, cut surfaces with a mix of Ga and As, since there is no clear rule for how to add the pseudohydrogens (nor any way to maintain the electrical properties of a semiconductor). The completion and analysis of such QDFT experiments on periodic GaAs surfaces are ongoing research projects which represent just one avenue for connecting mesoscopic Wulff theory to physics at the molecular/atomic scale. We will show in the next section that analysis of Wulff SES shapes in relation to the evolution of solvated (unbounded) nanoparticle morphology can

also be used as a prospective means of correlating Wulff theory to physics at the molecular/atomic scale.

II. v. Simulation of the Evolution of Solvated Nanoparticle Morphology via Augmented Wulff Constructions and Bezier shapes

Nanoparticles formed via solvated catalysis represent a case of unbound crystal growth where the small particle size and equilibrated growth conditions lead to crystal with shapes which can be described by the classical Wulff constructions for ECS and SES, and by spheres. We have shown that Wulff theory can be used to estimate surface energies by visual fitting of TEM images of crystals grown under bounded equilibrium growth conditions during epitaxy, and that those energy estimates can be correlated to surface energy calculations from first-principles. Modeling solvated nanoparticles via Wulff shapes offers another avenue for estimating surface energies and correlating to the case of bounded nano-pyramid/pillar growth which has the advantage of *not* requiring special knowledge of QDFT or massive amounts of computational processing. We outline a spatial algorithm for defining and visualizing Wulff surface energy shapes developed by Ryan Molecke. Linear spatial progressions between spheres, SES shapes, and ECS shapes, represent an evolution of morphologies which mirrors the underlying physical processes and observed evolution of morphologies for solvated nanoparticles. This link between the Wulff theory and unbounded nanoparticle growth represents a conceptual avenue for defining the molar and free energies of nanoparticles, and for making basic statements about the shapes and chemical properties of the nanoparticle surfaces.

The Wulff theory states that an SES shape must follow the rule that the inner convex shape be the given ECS shape. We can define such a surface (or infinite sets of such surfaces) using Bezier curves and “control points”. Although this newly-constructed SES will be just one of many non-unique surfaces that may satisfy the Wulff theory for a given ECS, we define general rules that will make the SES most closely resemble the smoothly graded shapes observed during solvated nanoparticle growth. This indicates that such reconstructed surface energy shapes closely correspond to the actual surface energy shapes for the crystal systems which they are visually matched to.

Bezier’s classical method for defining curvilinear coordinate systems and curved shape is a common tool in computer graphics. It is a vector-based spatial algorithm for dividing lines or surfaces into sub-elements so that a smooth gradient is generated among all the sub-elements, according to a number of “control points”. Figure 1.14 shows an example of a Bezier line and the four control points. In the case of a line, two endpoints

and any number of control points may be specified, and any number of sub-divisions of the line may be specified, such that any linear shape can be defined by a Bezier line, with a customizable level of resolution.

Similarly, in the case of a

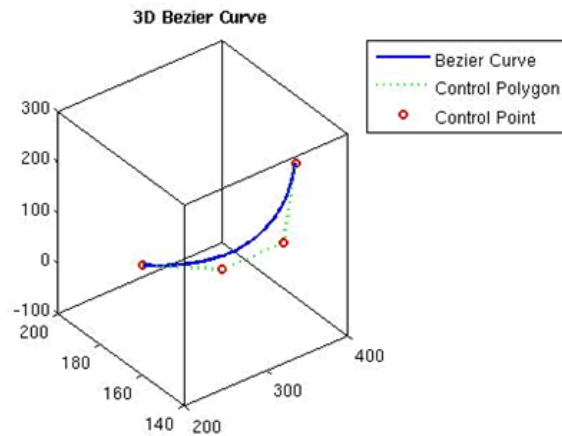


Figure 1.14) 3D Bezier line (blue) and control points (red)

surface, any square number of control points can be specified, and any 3D surface can be defined with a customizable level of resolution.

Figure 1.15 shows a 3D Bezier surface defined by nine control points.

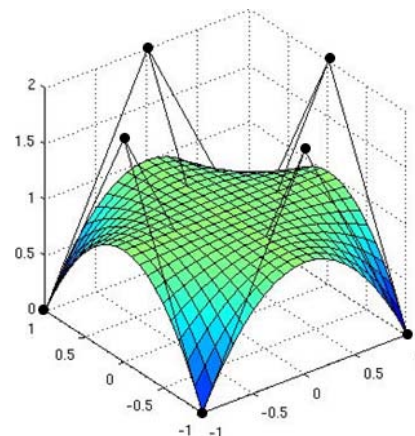


Figure 1.15) 3D Bezier surface (multicolored) and control points (black dots)

Any curved or faceted shape can be matted with Bezier control points and approximated with an any number of spatial subdivisions, for any desired degree of spatial resolution. We describe a method for extrapolating SES shapes from given

ECS shapes using common Bezier control points between the two shapes. The plotting algorithm and software that uses it is referred to as *surface extrapolation by reverse-plotting of energy trajectories* (or SERPENT), because the SES shape is extrapolated from the ECS shape, such that the Wulff construction is solved in reverse, and the resulting shape defines an energy surface with sub-divided energy gradient “trajectories”

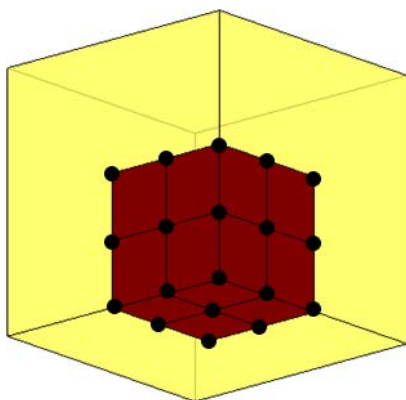


Figure 1.16) Matting of Bezier control points onto a cube, showing a single vertex matted with control points to the three adjacent facet centers.

defined by the Bezier control points. A SERPENT plot is a Bezier surface approximation to one of many non-unique surface energy shapes associated with a given ECS shape.

For any faceted shape, a Bezier grid can be drawn between each vertex and the centers of their adjacent facets, as shown in Figure 1.16. By adjusting the geometry of the control points, a surface energy shape can be defined. Figure 1.17

shows the same cube with adjusted two of the control-points adjusted inwards towards the facet center points. We use a master *anisotropy* variable which pushes the control points outwards from their matted position to produce a SERPENT plot which approximates a surface energy shape. Sets of control points (edge points, vertex points, and the central control point) are defined to conserve symmetry in the final SES shape, and the coordinates for each set are computed via empirically-fitted forms which include the master *anisotropy* variable and yield a first approximation to the surface energy shape for any given ECS. There are also “tuning” variables which allow the control point sets to be manually adjusted to achieve smoothly graded surfaces customized for a given ECS shape (see MATLAB SERPENT code, appendix 1).

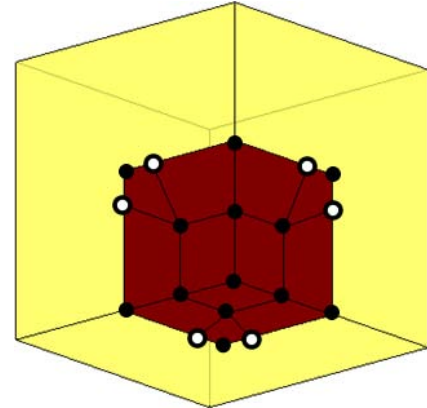


Figure 1.17) Matting of Bezier control points onto a cube, with one set of control points adjusted towards the facet centers (indicated by white outlined circle)

Figure 1.18 shows the Bezier control points after they have been adjusted to a certain level of anisotropy and tuned for the cube ECS shape. The control points at the facet centers always remain pinned to the ECS facets, so that the inner shape always remains the ECS shape. The control points which lie on the vertices and edges could also be pinned in place following this same rule, but are not necessarily required to be pinned, and allowing

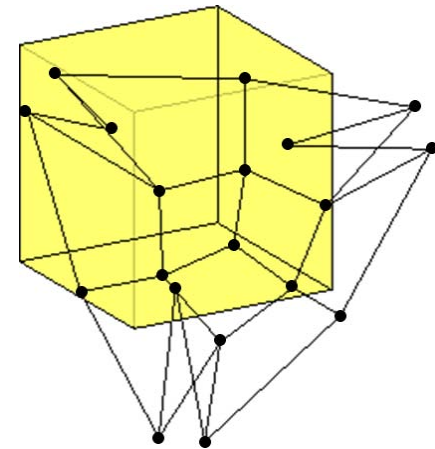


Figure 1.18) Final positions of the Bezier control points after SERPENT algorithm and tuning adjustments are applied.

them to move outwards from the center enables a more smoothly-graded final SERPENT plot / SES shape to be generated.

Figure 1.19 shows the Bezier surface generated by the control points shown in Figure 1.18 where the surface is displayed in false-color according to the facet orientation energy (red being higher energy, and blue being lower energy facet orientations).

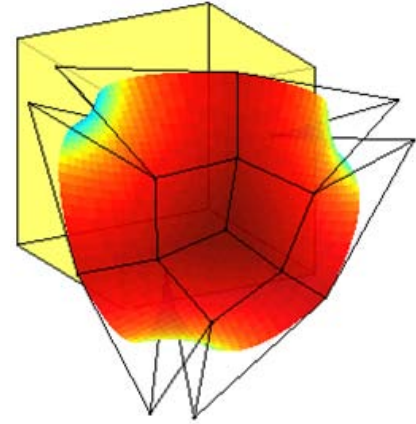


Figure 1.19) Bezier shape generated from control points (shown in Fig. 1.18) in false-color, and the Bezier control grid

Figure 1.20 shows a SERPENT plot / ECS surface with four vertices mapped to their adjacent facets

with Bezier control points, rotated and shown behind the cube ECS shape (which has been made transparent for a better view). The inward pointing funnel shapes in the SERPENT / SES shape intuitively and visually show how the inner cube ECS shape is the minimal shape formed by all tangents to the outer SES shape.

For a full catalog of common ECS shapes and their corresponding SERPENT / SES shapes, please refer back to Figure 1.3. The final SERPENT / SES shape for a cube ECS shape is repeated, for clarity, in Figure 1.21. The regions of the SERPENT / SES shapes which are non-minimal have been rounded over the vertexes and edges of the ECS shape, however they could theoretically be pinned there (as discussed) or contain extra non-primary minima

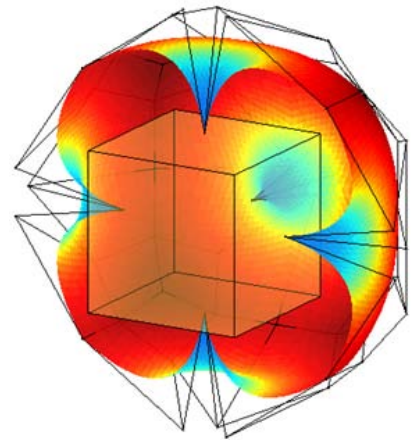


Figure 1.20) SERPENT plot / ECS shape cut in half and shown behind the transparent cube ECS shape to which it correlates

which correspond to higher-energy facets that are not seen in the ECS (minima which may exist but do not appear in the ECS after convex shape minimization).

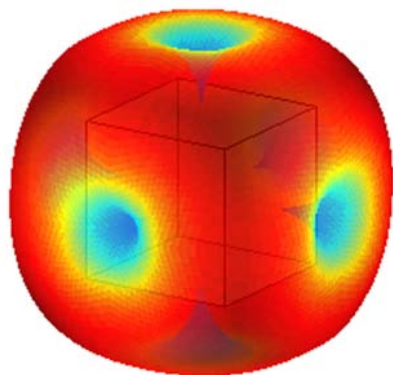


Figure 1.21) Full SERPENT / SES shape shown in false-color and made transparent so the inner cube ECS shape is visible.

In order to more completely describe the evolution of solvated nanoparticle morphology using Wulff shapes, a third type of shape is examined, which is the approximation of a sphere generated by projecting the SERPENT Bezier control points onto a sphere. The spherical shape represents the morphology of nanoparticles grown in non-equilibrium conditions, where adatom

mobility is severely limited, and the effective surface energy shape is also a sphere for this case. The sphere is a competing morphology to the ECS shape as nanocrystals grow and equilibrate to the solvent conditions. The surface energy shape is a transitory shape on the energy minimization path between sphere and ECS shapes, which we theorize to be a generalization for the morphology of quasi-equilibrated nanoparticles. Figure 1.22 shows a spherically-projected SERPENT / SES shape for the cube ECS shape. This sphere is slightly non-uniform due to the discretization caused by the Bezier control points, however this effect is reduced in shapes with more facets and vertices, and is a close approximation to the sphere for most shapes (except tetrahedrons octahedrons).

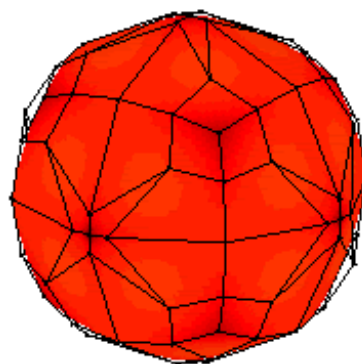


Figure 1.22) Spherical projection of the SERPENT / SES plot shown in Fig. 1.21

By performing a linear progression between the sphere shape and the SES shape, we can simulate a nanoparticle undergoing internal and surface minimization of molecular structure and surface energy as it equilibrates in solution after a period of non-equilibrated growth, i.e. nanocrystal seed growth. By performing a linear progression between the SES shape and the ECS shape, we complete the simulation of nanoparticle equilibration or solvated growth, ending with ECS shapes that correspond to nanoparticle morphologies demonstrated in literature. Figure 1.23 shows a series of images from such linear progressions (perform using custom MATLAB software included in code Appendix B), which can be generated at any number of intervals along the linear spatial progressions and collated to form animations of solvated nanoparticle growth morphologies, similar to how animations of bounded crystal growth were produced. Similar progressions of shape can be performed for any given ECS shape and thus animations of nanoparticle crystal growth can be generated for any theorized nanoparticle morphology.

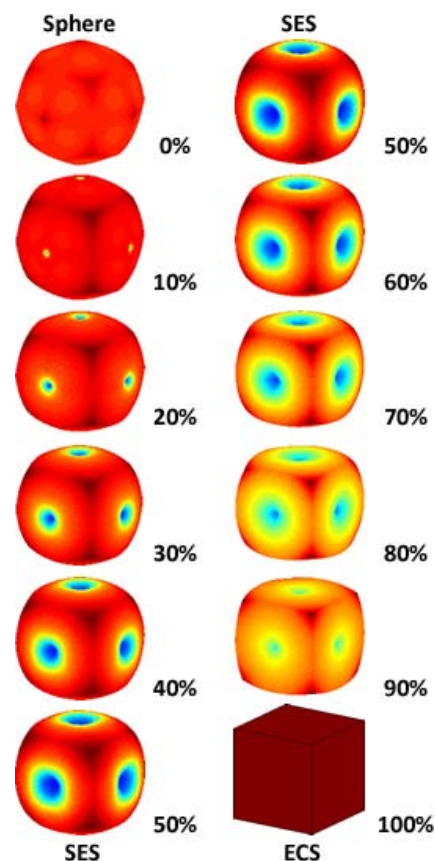


Figure 1.23) Progression of the sphere to SES shape, and the SES shape to ECS shape enabled by SERPENT plotting. Progression percentages from sphere to final ECS shape are indicated.

In order to completely link spheres and Wulff SES / ECS shapes, and thus Wulff theory to the smaller-scale atomic/molecular regime, a molecular model would need to be preassembled, with bonded atoms cut into regions bounded by the spheres or Wulff ECS

/ SES shapes modeled here. An algorithm for determining regions of crystal order and jumbled (less ordered) regions of atoms at any given stage of the evolution of nanoparticle shape would need to be defined, and the orientation of those regions with respect to the bounding sphere / SES / ECS could be found based on surface energy minimization rules, such as a postulation that surfaces composed of one element versus another would have the lowest energies. Even without performing the above-listed tasks, some general statements about the surface chemistry can be deduced from their postulated correspondence to SES shapes.

From a visual analysis of the spheres / SES / ECS shapes, it is clear that only once the nanoparticle morphology reaches the final ECS shape will it have large flat faceted regions corresponding to exposed atomic lattices and thus regular broken-bond geometries on the surface. Spherical and SES shaped nanoparticles will have a predominance of highly stepped regions and thus irregular molecular broken-bond geometries on the surface. This means that any particle able to bond to any broken-bond “docking site” geometry of surface atoms may find a binding spot on the spherical or SES shaped, less equilibrated nanoparticles. The fully-equilibrated ECS-shaped nanoparticles will present only certain broken-bond docking-site geometries on their surfaces and thus should bind only those molecules which can fit into those docking sites, i.e. the fully equilibrated ECS-shaped nanoparticles are theorized to have *less* chemically or biologically active surfaces than the not-fully-equilibrated spherical or SES-shaped nanoparticles. This is also supported by the observation that the fully equilibrated nanoparticles should be at the lowest internal and surface molecular spatial configuration, and thus be somewhat passivated against further reactions in other

solvents, particularly in solvents with similar chemical properties to those which they are formed in.

This section demonstrates that Wulff SES shapes can be extrapolated from given ECS shapes, and that spherical projections, SES, and ECS shapes can be transformed into one another through linear spatial progression, posited to correspond to the evolution of solvated nanoparticle morphologies. By comparing energies estimated from Wulff shape fitting to bounded versus unbounded nanoparticles and QDFT first-principles calculations, the effects of epitaxial beam orientation on bounded crystal growth and the effects of solvent composition on unbounded (solvated) crystal growth may be further characterized, and this work provides the methods and tools for such further research. We have refined and augmented tools for modeling Wulff shapes in several ways, and demonstrated the correspondence of Wulff shapes to nano-pyramid/pillar/particle shapes and the evolution of nanoparticle morphologies, and their usefulness as a tool for estimating surface energy values. We have discussed methods for metering Wulff shapes using classical solution thermodynamics units, and for correlating surface energy measurements between Wulff models and QDFT calculations, thus making significant progress on the path towards the goal of bridging the mesoscopic and scalable Wulff theory to the smaller molecular/atomic regime of physics. Several goals have been accomplished by this research, including the development of advanced crystallographic modeling software, the development of new theories regarding crystal growth dynamics, the discovery of a method for linking the mathematical constructs underlying the fields of classical crystallography and QDFT, and the proposal of a method for investigating the chemical and bio-activity of unbound nanoparticles.

II. vi.) Summary of Directed-Assembly of Nanocrystal Growth

We have presented a description of the role that crystal growth can play in multiscale directed-assembly, along with potential applications. New research avenues for investigating the crystallography, thermodynamics, and surface chemistry of nanoparticles have been uncovered. Experimental data demonstrating GaAs nanocrystal growth was summarized, and classical crystallographic theory including a modern augmentation was applied to visually fitting static crystal images and dynamically simulating evolution of crystal shape during PECVD. Analytical methods for determining crystal facet surface energies from classical crystallographic theory were explained, along with the role of these surface energies in crystal growth. Quantum density functional theory methods for determining the surface energy values from first-principles were discussed, and preliminary surface energy data from all three methods (experimental fitting, augmented crystallographic theory, and QDFT) was compared in table form and evaluated critically. This concludes the section on crystal growth in multiscale direct-assembly.

Chapter III. LASER Tweezers Optical Trapping

III. i. Introduction to Directed-Assembly via Colloid Processing

The goal of colloid processing is to overcome normal ordering and local entropy vis-a-vis assembly to produce ordered structures. In the crystal growth section, crystallographic theory, atomic, and QDFT methods were used to explain the underlying physics of the system, an approach which drilled down through scale regimes until picoscale electronic densities were being approximated in attempt to fully explain the multiscale physics of the system. In colloid processes, mesoscale simulations and measures of thermodynamics and aggregate behavior are used to explain the underlying multiscale physics of the system. This approach pans out through the scale regimes for massive (microscale) simulations and bulk order parameters in attempt to create emergent functional properties.

In the current chapter on we describe the measurement of position, diffusivity and displacement of particle held in LASER tweezers optical traps, and a method by which the interparticle potentials can be calculated from those measurements. In the next chapter on soft-particle colloids, we show that interparticle potentials and Stokesian fluid dynamics underpin the aggregate behavior of groups of particles, and described methods for modeling these potentials for simulations of directed-assembly system. In these two chapters, we apply coarse-grained interparticle potentials to investigate the effects of “soft” biopolymer coatings on the behavior of nano- or microparticles. We show that non-equilibrium environments such as evaporating films or irradiation processes can drive assembly, and describe methods for matching simulations of directed-assembly of soft-particle colloids to experiment. We propose prospective nanoscale-featured devices

and conceptual production methods, and discuss advanced measures of cluster, randomness, and order in colloid systems.

It is worth noting at this point that the direction, methods, and motivations for this research have evolved over the course of two years. The initial motivations for laser tweezers optical tracking studies were to investigate the effect of lipid / peptide coatings on microparticles and their interactions with live cells for drug delivery applications. The optical trapping research laid the groundwork in biochemistry, coarse-grained interparticle potentials and nanofluidics necessary for the next phase of research addressing soft-colloid processing, which is motivated by thin films, photonics, and nanoelectronics applications.

III. ii. Force Measurement via Laser Tweezers Optical Trapping

Laser tweezers optical trapping was first demonstrated in a seminal paper by Ashkin and Chu⁴⁶ in 1986. Over the last 25 years, researchers have advanced the technical capabilities of these systems and accomplished some astonishing feats, such as the

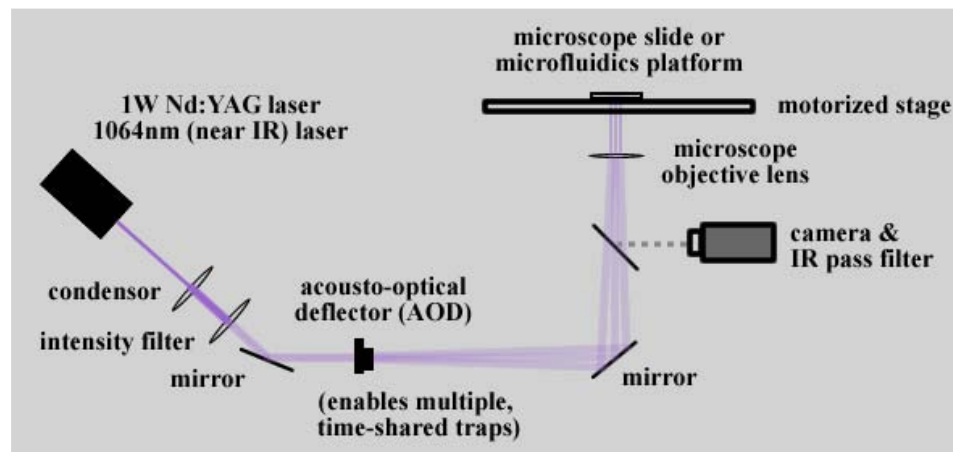


Figure 3.1) Schematic of the optical trapping system used for research presented in this paper. Omitted are desktop computer control systems for the opto-acoustic deflector, stage motors, and camera.

force and step-size measurement of a kinesin protein walking down a microtubule⁴⁷, the force required to unzip DNA using a helicase protein⁴⁸, and the first Bose-Einstein condensate⁴⁶ (this last example led to the award of a Nobel prize in 1997).

Figure 3.1 illustrates the major components in the optical tweezers setup used in this work. An Nd:YAG (neodymium-doped yttrium aluminum garnet) laser with wavelength 1064nm and maximum power of 1 Watt is sent through a condenser (backwards), intensity filter, and into the acousto-optical deflector, which can split the beam into multiple time-shared beams. This allows multiple optical traps to be formed on the microscope stage using a high numerical aperture lens. The microscope itself houses up to 10,000x magnification strength, high-framerate CCD camera, monochromatic light sources and filter cubes for fluorescence resonance excitation and imaging, and linear response worm-drive stage motors. Momentum is transferred from photons in the beam when the index of refraction difference between the particle and the solvent causes their paths to bend, forming a stable 3-dimensional trap on the microscope stage, as shown in Figure 3.2.

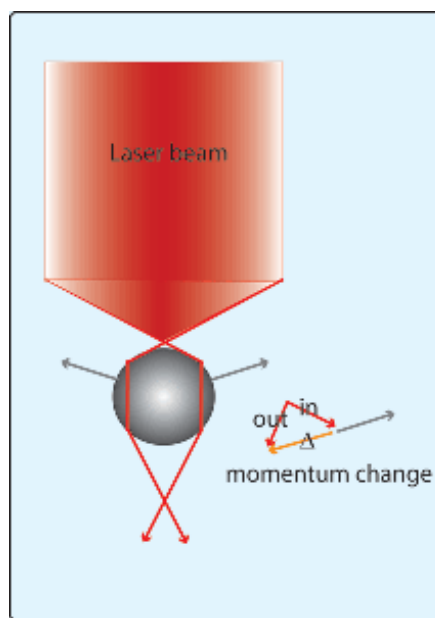


Figure 3.2) Momentum diagram for laser tweezers optical trap.

Two distinct methods of measuring interparticle force in laser tweezers were implemented in this study. The first is termed the “blinking tweezers” technique and consists of repeatedly capturing and releasing the particles in close proximity and measuring the interparticle force based on their relative diffusivity over time. The second

is termed the “direct force” test, which consists of measuring the force based on instantaneous displacements of the particle from the center of the beam. Both tests require imaging the particle with high-resolution and averaging the results over many thousands of frames (3 minutes or more at each separation interval) to get a statistically valid force measurement through the noise created by the Brownian motion of the particles. The center of both particles must be identified for each frame of the video before their diffusivity can be determined. In practice, a variety of artificial-vision algorithms are used among LASER-tweezers labs for the purpose of finding the centers of the particles at each frame, and this software is generally proprietary (and not shared among research labs), customized to the specific hardware profile of a given laboratory’s equipment, and can vary greatly in speed and accuracy depending on the skill and experience of the artificial-vision software-development team.

The first task in measuring the interparticle forces is to calibrate the force of the trap on the particle, in terms of a spring constant. This will also illustrate the complexity of the artificial-vision center-finding task and the implications of that issue on final error estimation. Figure 3.3 shows the relative movement of the microscope stage and LASER beam movement relative to the particle, which drags

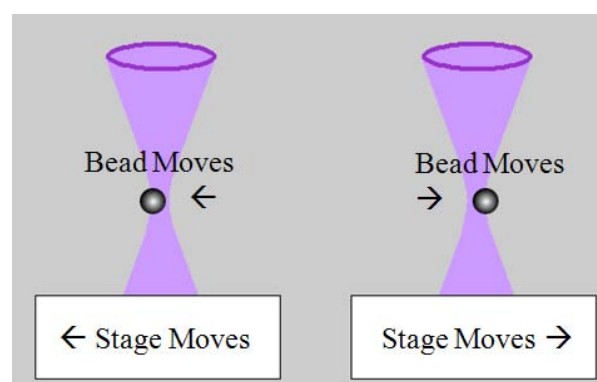


Figure 3.3) Schematic drawing of the stage and LASER beam movement relative to the particle

the particle through a solvent as the particle is held in the moving optical trap. The spring force is calibrated by dragging particles through the medium by moving the microscope

stage at a known velocity, and measuring displacement from rest position in the center of the beam, illustrated by Figure 3.4 and described by the following equations.

$$F = 6\pi\eta va \quad (\text{Stokesian drag}) \quad (3.1)$$

$$F = k_{trap} d_{cal} \quad (\text{Hookean Spring rule}) \quad (3.2)$$

$$k_{trap} = \frac{6\pi\eta va}{d_{cal}} \quad (\text{Optical trap spring constant}) \quad (3.3)$$

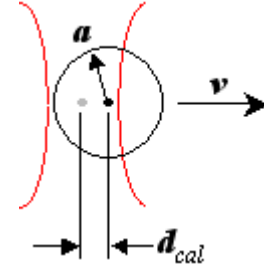


Figure 3.4) Trap calibration by Hookean spring rule

where η is the viscosity of the fluid (water in this work), v is the velocity of the stage and consequently the velocity of

the particle relative to the medium, a is the radius of the particle, and d_{cal} is the distance the particle displaces from beam center caused by the force of the drag against the medium.

Figure 3.5 shows a greatly magnified view of a still-frame image taken of an approximately 2.4 μm particle using CCD camera at 10,000X

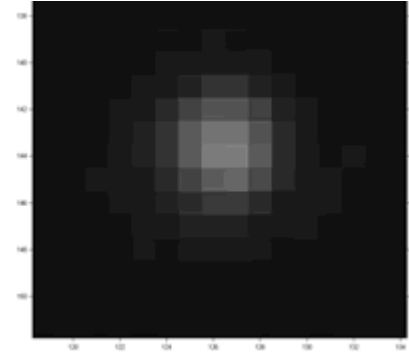


Figure 3.5) CCD image of a 2.4 μm SiO_2 silica bead held in an optical trap and imaged at 10,000X

magnification. At this resolution, during this experiment, our camera had an image capture resolution of 3 pixels / μm , as shown by the particle appearing as approximately 10-12 pixels wide in the image. A quadratic curve-fitting of the pixel intensities across a detected “bright spot” can locate the particle centers to within $1/10^{\text{th}}$ of a pixel, or 300nm in this case. This amounts to a poor resolution if you are trying to measure nanometer-scale force interactions occurring among biopolymer layers on the particle surface. In the best case, we were able to achieve a resolution of the particle center to within an 80nm minimum diameter spot.

Another complication can be seen when we plot particle position over time during calibration. Figure 3.6 shows a plot of particle center-positions over a time-period of 25 seconds, where position in this case is a 1-dimensional distance from the corner of the image. The upward peak on the left indicates the particle deflecting in one direction as the stage move for 5 seconds, while the downward peak on the right indicates the particle deflecting in the other direction as the stage moves (in the other direction also) for another 5-second interval.

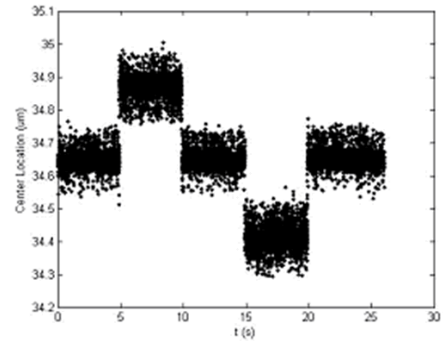


Figure 3.6) Plot of particle center position (vertical-axis) over time (horizontal-axis)

When we transform this position data into actual x-y position data and zoom in on the time axis, we get a plot like that in Figure 3.7, where we can clearly see that the position data is not a single line or curve indicating a smooth particle movement, but a broad band of positions over a 200-300nm indicating thermal agitation (or stray movement cause by solvent hydrodynamic / lubrication forces), and data banding caused when the normal curve-fitting of the center-position shifts across pixel boundaries. These problems are again solved by quadratic curve fitting of the particle positions, but this time we are curve-fitting a histogram of the particle positions over time, meaning we are now averaging multiple data points over time and losing temporal resolution against our CCD framerate.

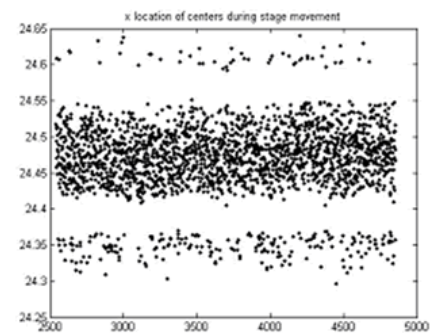


Figure 3.7) Data from Fig. 3.6, calculated x-coordinate of a particle center

Figure 3.8 shows a histogram of particle position data for a 30ms interval, and the quadratic curve which is fitted to the data. The particle center for that interval is taken as the top of the read peak, however the curve is not always so clearly normal-shaped, and the spatial inaccuracy caused by the artificial-vision pixelated-spot problem are still included in this extrapolated particle center position.

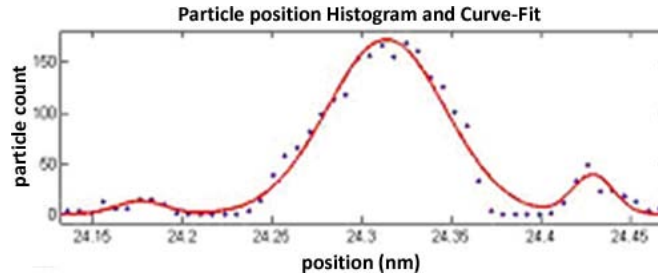


Figure 3.8) Particle position histogram (blue dots) and quadratic curve fit (red line) for a 30 ms interval of particle positions.

In the “blinking tweezers” method, two traps are split from the AOD, and they both blink simultaneously, trapping and releasing the particles with 30ms rate in each state (shown in figure 3.9). This is repeated at a range of particle separations so that a force “curve” can be plotted, with force being determined from relative diffusivity by the following set of equations:

$$v = \langle \Delta r \rangle / t \quad (3.4)$$

$$D_0 = \langle \Delta r^2 \rangle / t \quad (3.5)$$

$$D = 2D_0 \left(1 - \frac{3a_h}{2r} \right) \quad (3.6)$$

$$F = k_b T v / D \quad (3.7)$$



Figure 3.9) Images from a blinking tweezers force measurement.

v (velocity), r (separation), t (time) , D_0 (relative diffusivity), D (diffusivity)
 a_h (hydrodynamic radius), T (temp), K_B (Boltzmann's constant), F (interparticle force)

In “direct force measurement”, the restoring force of the trap on the bead is treated as a Hookean spring, and the interparticle force is simply calculated as the Hookean spring force times the displacement distance.

The goal of the first series of experiments was to measure force curves for bare particles across pH and salt concentration and to verify the force curves with known theory for coarse-grained interparticle potentials (in ionic solvent), i.e. DLVO theory. Preliminary results were successful, using the classical DLVO theory for sphere interactions in monovalent ionic solutions as described by Israelachvili (shown in Figure 3.10). The experimental values in this graph appear to follow the theoretical curve for separations above Debye length, under which van der Waals (vdW) attraction⁴⁹ is thought to be negated by steric and electrofluidic forces. This was a successful experiment, by itself, and the task at this point was to correlate further experiments across ionic strength and pH.

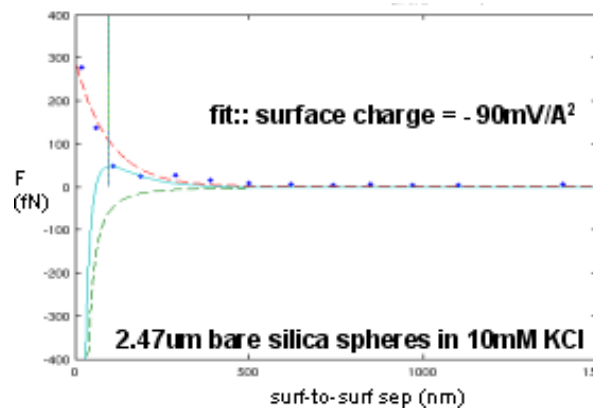


Figure 3.10) Force versus separation curve, blue dots are experimental values, red dotted line electrostatic repulsion term, green line is vdW attraction, blue line is net force, green vertical line is Debye length for this system. (blinking tweezers method)

The following equations from Israelachvili²⁰ describe the Derjaguin “weak overlap” force approximation for interparticle force between charged spheres in a monovalent electrolytic solution, using a variation on classical DLVO theory known as the Debye-Huckel approximation to the Gouy-Chapman theory (lines shown in fig 3.10).

$$F_{electrostatic} = (64\pi R k_b T \rho_{\infty} \gamma^2 / \kappa) e^{-\kappa D} \quad (3.8)$$

$$\gamma = \tanh\left(\frac{ze\phi_0}{4k_b T}\right) \quad (3.9)$$

$$F_{VDW} = \left(\frac{-AR}{12D}\right) \quad (3.10)$$

$$F_{DLVO} = F_{Electrostatic} + F_{VDW} \quad (3.11)$$

For particle radius R , Debye length κ , ionic concentration (far from the particle surface) ρ_{∞} , ion valence z , electronic charge e , electrostatic surface charge ϕ_0 , Hamaker constant A , and surface-to-surface particle separation D .

This formulation is one of several (historical and modern) coarse-grained potentials for interparticle force in ionic solvents. Newer models generally attempt to correct for the “coulombic screening” of the vdW attractive term at particle separations below the Debye length (which represents a distance into the solution in which the ions are affected electrically by the presence of the particle). In practice, it was more difficult to fit the collective results to a newer model, and the classical theory was deemed practical enough for plotting theory against experimental force curves, keeping in mind this coulombic screening effect when interpreting the data.

An important aspect of these experiments and fitting models is the changing potential of the particle based on the pH of the solvent. This investigation depends on

fixed solutions prepared with a set amount of NaOH. The Good's buffer⁵⁰ MES, 2-(N-morpholino)ethanesulfonic acid, was slowly added until a desired pH was achieved. Then, particles were added to each solution for Zeta potential measurement (Zeta potential is a unit metric which is directly proportional to surface charge), and the results are shown in Figure 3.11. The bare silica particles show a gradually increasing magnitude of surface charge as pH increases, which is expected since silica has a very low pK (the solvent pH at which the particle would have zero chemical / surface potential). For 1-palmitoyl-2-oleoyl-sn-glycero-3-phosphocholine (POPC) lipid-coated silica

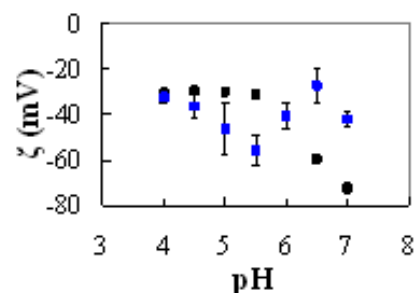


Figure 3.11) Particle Zeta potential across pH for bare silica particles (black) and POPC-coated silica particles (blue)

particles of the same dimension, the surface potential is expected to exhibit the pK of the lipid coating. POPC is a lipid with a “zwitterionic” head group, meaning it has spatially separated anionic and cationic regions. This zwitterionic head group means the particle will exhibit the opposite charge as expected near its pK value, which is approximately 6, as anionic regions are neutralized by the abundance of hydrogen atoms in acidic solutions and cationic regions are neutralized by the lack of free hydrogen atoms in basic solutions. This expected zwitterionic behavior in the coated particle is demonstrated by the blue points in Figure 3.11, which shows that the POPC-coated particle has an opposite slope (of surface potential vs. solvent pH) at the pK value of POPC, so this was considered a successful experiment and the data (Zeta / surface potential) was incorporated into our curve-fitting of observed interparticle potentials to DLVO theory.

Figure 3.12 shows variance of measured interparticle force across pH, in a set of experiments with POPC coated 2.47 μm silica beads. The theoretical lines (fitted for changing electrostatic surface charge) and the experimental results roughly line up. Unfortunately, the overall repeatability and resolution of this method was insufficient to resolve the effect of the lipid coating.

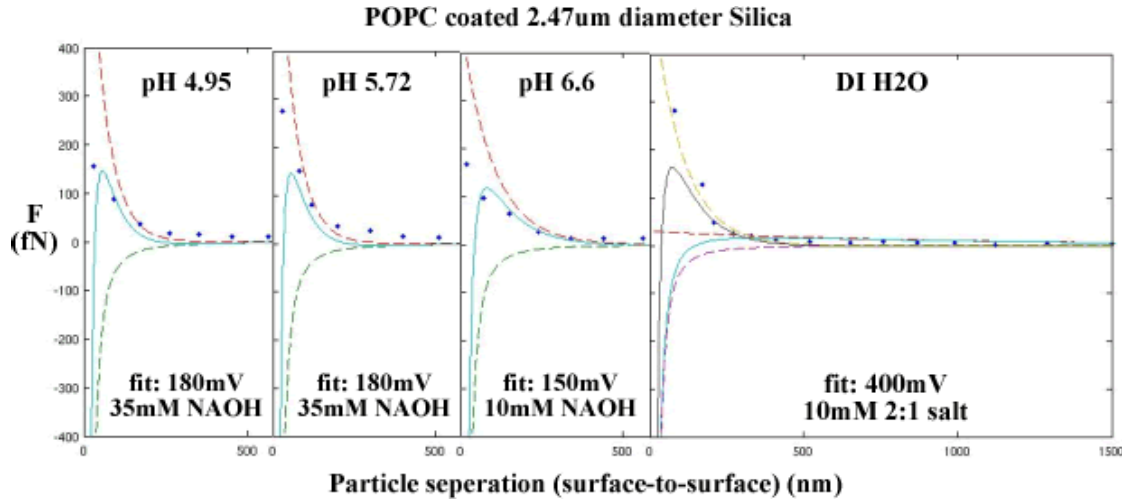


Figure 3.12) Graph overlay of a series of experiments with POPC coated particles across pH

One difficulty in fitting the observed interparticle potentials to DLVO theory arose from the difficulty of establishing ‘error bars’, or accurate error estimates in general for the experimental data. The method described above for artificial-vision center-finding and time-interval averaging of particle position use successive quadratic curve-fitting which can have unique error margins for each single frame, and also for each time-averaged interval of frames, depending on how thermally ‘noisy’ the system is from moment to moment and even on how a (not-perfectly spherical) particle reflects light as it turns with respect to the camera (which can happen at high frequency). A compounding difficulty was the long duration of experiments. With longer experiments, more frames (and thus particle position coordinates) were collected, and the apparent resolution of the

interparticle force-measurements was increased, however since we did not have a real-time system for executing the center-finding and subsequent force-calculating routines, long periods of post-processing data were required. Long duration-experiments also have the drawback that stray particles are more likely to enter the optical trap with at least one of the particles, which can ruin a long experiment and require a restart of the entire experiment, in worst case all the way back from the sample-preparation stage. All of the above problems can be alleviated by higher optical resolution, faster frame-rate and better pixel-count cameras, and better artificial-vision software. This highlights the need for incredibly expensive optical components and great artificial-vision middleware developers in the field of LASER tweezers optical trapping.

The “direct force method” was not able to offer any significant improvement in accuracy over the “blinking tweezers method”, however, it may be preferable because once particles “snap” together, the laser tweezers are often not strong enough to pull them back apart. For this reason it can be better to hold the particles apart while measuring the interparticle forces, in the case of net attractive forces, since a “blinking tweezers” experiment can end prematurely with the freely diffusing particles joining together.

Other experiments aimed at characterizing lipid behavior on the microparticle surface were performed, with limited success, and they are briefly summarized below. Large unilamellar vesicles (LUV) of varying phospholipids were created by electroformation as described in many previous efforts⁹⁻¹⁵. Multilamellar vesicles were held in the trap and observed fusing, but controlled fusion of LUV was not achieved. Fluorescence recovery after photobleaching⁵¹ (FRAP) was performed to characterize the lateral mobility of lipid-anchored and non-anchored lipid fluorophores on the silica

surface, however both types of lipid fluorophore ended up having such a high mobility on the surface of the bead that FRAP could not measure the speed (however this does confirm high lateral lipid / fluorophore mobility). Tests were performed in attempt to track the transferred of lipid from one bead to another, however finding fluorophores with high enough photostability for a confirmation of this effect was a challenge that went unsolved. Tests were also performed in attempt to measure forces on live cells, however a large problem here is computationally finding the center of mass of a non-spherical object for every frame, and also the live cells (*Saccharomyces cerevisiae*, or baker's yeast) had a tendency to tumble in the trap.

III. iii. Conclusions on LASER Tweezers Optical Trapping

To maximize the information from optical trapping, even if the main goal of characterizing lipid-coatings was not achieved, we analyzed the source of the errors and suggest ways for improving the methods for future reference. A more complete statistical analysis of the error in computational areas is abbreviated below.

The experimentally controllably sources of error are generally related to the chemical laboratory preparations, the resolution of the camera (spatially and temporally), and duration of the experiment. Our liposome coating techniques were tested and confirmed via confocal fluorescence imaging of lipid fluorophore coated silica particles, and our LUV formation methods were confirmed by fluorescence microscopy (the LUV vesicles actually disappear without the excitation light source because they are so thin that they are invisible in optical wavelengths). Water reserves were specially stored in attempt to limit CO₂ dissolving in a larger reservoir or ionic concentration changing over time. The salt / pH balance method implemented was non-trivial, and might be improved

upon or performed with greater precision by a professional lab chemist. New methods may be devised instead of the blinking tweezers and direct force tests that could possibly be more efficient, and new computational center-finding algorithms are always tailored to the hardware available and software expertise of group members.

Overall, the main limitation to laser tweezers right now is the minimum particle size which can be manipulated: which is about 1 micron. This size limitation affects resolution in such a way that it is difficult to characterize nanoscale surface coatings with laser tweezers. Whether this type of research can be performed with an atomic force type microscope remains to be seen. This clearly motivates soft-particles as an area where modeling and simulations can be of particular value in understanding interparticle potentials and colloid dynamics. Optical trapping is still a developing field with very much promise, and the above experiments demonstrate experiments with laser tweezers can encompass bio-chemistry, hardware and software design, optics, statistics, and nanofluidics.

Chapter IV. Directed Assembly of Nanoparticle Colloids

IV. i. Introduction to Colloid Science: Methods and Applications

Customization and functionalization of the electronic, magnetic, optical, stimuli-responsive, and bio-active properties of nanoparticles (NPs) is a large research field with applications in medicine⁵²⁻⁵⁶, sensors⁵⁷⁻⁵⁹, opto/electronics⁶⁰⁻⁶³, and materials science⁶⁴⁻⁶⁶. A variety of shapes and sizes of NPs composed of a core and sometimes several shells of metal, semiconductor, and bio-molecules have been demonstrated^{52,53,67-69}. Strict controls over pressure, temperature, and chemical composition during solvated catalytic reactions is a common route to customization of particle shape, size, and core/shell composition⁵²⁻⁶⁹. Inorganic multi-shell particles can be specialized for desired energy gaps in the electronic states of the constituent materials and desired crystal phonon spectra on the surfaces, leading to customization of electromagnetic and optical properties of NPs for applications such as medical imaging or hyperthermic therapy^{52-56,60-63}. Often a secondary shell or biopolymer material is used to passivate the core against bio-activity, such as in magnetic or fluorescent NPs, with SiO₂, gold, lipids, and polyethylene-glycol (PEG) being common choices for the outer layer^{52,53}. Antigens designed to target NPs to bind or transfect specific cells within the body, heat-sensitive poly-(NIPAM) shells designed to release drugs, and bi-fluorescent quenching of drug molecules for medical imaging have all been demonstrated⁷⁰⁻⁷². NPs composed of viral phage capsids modified to display cancer-cell-specific antigens can also transfect cells and deliver a payload of drug molecules^{73,74}.

Ordered structures such as lattices and superlattices of NPs are relatively modern research topics which fall into the paradigms of bottom-up and directed-assembly, and are geared more towards applications in environmental sensors, opto/electronics, and thin

films^{75,76}. Coffey, et al., demonstrated custom long-range order in NP colloids via specialized bonding geometries in segments of surface-attached DNA⁷⁷, and Murray, et al., have recently shown that geometrically complex superlattices can be formed from colloids containing more than one size or shape of particle⁷⁵. A main focus of this chapter is the assembly and control of final geometries in structures formed from “soft”-NPs at or near the surfaces of thin films. “Soft”-NP colloids, those grafted with polymer-chains, are of particular interest because both core/shell and outer coating properties are greatly variable and tunable.

A key goal in directed-assembly of colloids is to induce the formation of lattice, chain, branch, or network structures which are amenable to nanoscale solid-state physics and bio-chemistry methods yet able to interface with and affect the macroscale. These structures can be formed during the response of a physical system to changing internal and external forces (such as interparticle forces, solvent lubrication forces, interfacial forces, external fields, or induced stresses) over time. Mesoscale simulation, crystallographic analysis, and spatial statistics are tools for understanding and engineering the formation of such structures. Systematic investigation of colloid assembly processes by matching simulation and experiment can help interpret underlying physics and allow a transition from the conceptual experiment phase to a guided device prototyping phase.

Two-dimensional (2D) or three-dimensional (3D) NP lattices represent a scalable mesoscale counterpart to atomic crystals, and concepts from crystallographic theory can often be applied when analyzing such lattices. Classical spatial statistics tests such as the Ripley’s K ^{78,79} and Hopkins’^{80,81} tests (described later in this section and in Appendix A)

can be applied to systems of particle coordinates to describe clustering vs. randomness profiles. We can also borrow from and expand upon classical “non-equilibrium molecular dynamics” (NEMD) methods⁸² to describe and simulate the formation of lattice, chain, branch, and network structures. NEMD is a field of physics which attempts to extrapolate characteristics of micro/macroscale materials or systems from approximations of the time-dependent, quantum-mechanical, many-body problem. NEMD can be applied in many ways to microscale rheology and is described by Hoover as a generalization of Gibbs' statistical mechanics to the non-equilibrium case⁸². Classical NEMD simulations consists of an n-body Newton mechanics solver tracking every particle; however, we can also apply approximations of averaged molecular interactions, flows, boundaries, and other fields effects (a process known as “coarse-graining”) and still accurately fit such simulations to empirical data from real experiments. Through such *successive* approximation and semi-empirical fitting of the time-dependent, quantum-mechanical, many-body problem, we can simulate realistic mesoscale systems without the computational burden of tracking every atom or molecule, which expands the scale of simulations possible on a given hardware device.

As a basis for our simulations of colloids, we can derive mathematical models of the physical attributes of a system, such as particle distribution, shape, orientation, mass, interparticle potentials, hydrodynamics and interfacial potentials, electromagnetic bias, and any other field effect. With the Large-Scale Atomic/Molecular Massively Parallel Simulator (LAMMPS) simulation engine, written in multi-threaded C++ at Sandia National Laboratories⁸³, our models become guidelines for mesoscale simulations of a virtual physical system over time. LAMMPS updates the velocity and position of each

particle in the system according to a Verlet-integration⁸⁴ time-stepping algorithm and our model definitions, with the maximum accuracy possible for a given hardware device (32-bit floating-point accuracy in our case). At each time-step in a simulation, the LAMMPS engine calculates pair-wise interparticle forces, any defined interface/boundary forces on the particles, hydrodynamic forces, and performs a thermostating algorithm which accounts for the thermal effect of Brownian motion. We model this system as an N-body force balance, where the momentum M_i of the i^{th} particle, with position r_i at time t is the sum of the thermal (Brownian), hydrodynamic, and pair-wise interparticle force:

$$M_i \frac{\delta^2 r_i}{\delta t^2} = \sum_j F_{ij}^{pair} \quad (4.1)$$

where each interparticle pair force, F_{ij}^{pair} , is the sum of the vdW, electrostatic, hydrodynamic, and thermal forces:

$$F_{ij}^{pair} = F_{ij}^{vdW} + F_{ij}^{Electro} + F_{ij}^{Hydro} + F_{ij}^{Brown} \quad (4.2)$$

Integrating Eq. 4.2 using the velocity-Verlet algorithm yields the new position, r_i , and velocity, $\frac{\delta r_i}{\delta t} = v_i$, for each particle for successive time-steps. In the next section, we also describe how Vincent's derivation of the Flory/Huggins' polymer/solvent interaction potentials for colloidal particles grafted with polymer coatings can be included in the above pair force such that:

$$F_{ij}^{pair} = F_{ij}^{vdW} + F_{ij}^{Electro} + F_{ij}^{Hydro} + F_{ij}^{Vincent} + F_{ij}^{Brown} \quad (4.3)$$

The above method, where particle position and velocities are explicitly tracked at each time-step, exemplifies modern “discrete-element” modeling/simulation, as opposed to

“finite-element” modeling/simulation in which attribute variables at the nodes of sub-divided spatial regions are used to describe a physical system.

Everaers’ derivation for the pairwise interparticle hydrodynamic and vdW potentials relies on the classical Lennard-Jones theory⁸⁵ which describes the interaction between two charged molecules or atoms. The Lennard-Jones potential, V_{LJ} , is mildly attractive, then becomes sharply repulsive as two atoms/molecules approach each other. As such, the mathematical form of V_{LJ} contains both attractive and repulsive terms:

$$V_{LJ} = 4\varepsilon \left[\left(\frac{\sigma}{r} \right)^{12} - \left(\frac{\sigma}{r} \right)^6 \right] \quad (4.4)$$

where ε is the depth of a potential well, σ is the finite distance at which interparticle potential is zero, and r is the distance between the particles. The r^{-12} term accounts for repulsive interactions at short ranges due to overlapping electron orbitals, an effect of the electron exchange interaction known as Pauli repulsion^{86,87}. The r^{-6} term accounts for the attractive vdW, or “London-dispersion” forces⁸⁸, which results from a short-range (on the order of a few nanometers) complementary quantum polarization in charged atoms/molecules represented as magnetic dipoles. The Lennard-Jones potentials are often referred to as the L-J, or 6-12 potentials due to these attractive/repulsive terms in Eq. 4.4. The Lennard-Jones interparticle force, F_{LJ} , is then derived from the interparticle potential, V_{LJ} as follows:

$$F_{LJ} = \frac{-\delta V_{LJ}}{\delta r} = -24\varepsilon \left[2 \left(\frac{\sigma^{12}}{r^{13}} \right) - \left(\frac{\sigma^6}{r^7} \right) \right] \quad (4.5)$$

Everaers’ derivation for the pairwise interparticle hydrodynamic and vdW potentials includes three sub-potentials between (big) colloidal particles and (small) solvent

particles: the colloid-colloid interaction energy, the colloid-solvent interaction energy, and the solvent-solvent interaction energy. The colloid-colloid interaction energy, U_{CC} , is derived by treating each colloidal particle as an integrated collection of Lennard-Jones particles of size σ , and contains both attractive and repulsive components, U_A and U_R (reflecting the attracting/repulsive components in the Lennard-Jones potentials):

$$U_A = \frac{-A_{CC}}{6} \left[\frac{2a_1a_2}{r^2 - (a_1 + a_2)^2} + \frac{2a_1a_2}{r^2 - (a_1 - a_2)^2} + \ln \left(\frac{r^2 - (a_1 + a_2)^2}{r^2 - (a_1 - a_2)^2} \right) \right] \quad (4.6)$$

$$U_R = \frac{A_{CC}}{37800} \frac{\sigma^6}{r} \left[\frac{\frac{r^2 - 7r(a_1 + a_2) + 6(a_1^2 + 7a_1a_2 + a_2^2)}{(r - a_1 - a_2)^7} + \frac{r^2 + 7r(a_1 + a_2) + 6(a_1^2 + 7a_1a_2 + a_2^2)}{(r + a_1 + a_2)^7} + \frac{r^2 + 7r(a_1 - a_2) + 6(a_1^2 - 7a_1a_2 + a_2^2)}{(r + a_1 - a_2)^7} + \frac{r^2 - 7r(a_1 - a_2) + 6(a_1^2 - 7a_1a_2 + a_2^2)}{(r - a_1 + a_2)^7} \right] \quad (4.7)$$

$$U_{CC} = U_A + U_R, \quad r < r_c \quad (4.8)$$

The colloid-solvent interaction energy, U_{CS} , is derived from the colloid-colloid interaction energy, by letting the size of one of the particles go to zero:

$$U_{CS} = \frac{2a^3\sigma^3A_{CS}}{9(a^2 - r^2)^3} \left[1 - \frac{(5a^6 + 45a^4r^2 + 63a^2r^4 + 15r^6)\sigma^6}{15(a - r)^6(a + r)^6} \right], \quad r < r_c \quad (4.9)$$

The solvent-solvent interaction energy has a more traditional form of the Lennard-Jones formula:

$$U_{SS} = \frac{A_{SS}}{36} \left[\left(\frac{\sigma}{r} \right)^{12} - \left(\frac{\sigma}{r} \right)^6 \right], \quad r < r_c \quad (4.10)$$

with the Hamaker energy prefactor, A_{SS} , set to 144 (assuming $\varepsilon \equiv 1$, such that $144/36 = 4$ and thus Eq. 4.10 matches the Lennard-Jones potential given by Eq. 4.4). The total contribution to the interparticle potential from Everaers' derivation of the hydrodynamic and vdW potentials, U_{Ever} , is then:

$$U_{Ever} = U_{CC} + U_{CS} + U_{SS} \quad (4.11)$$

and the corresponding total interparticle force, F_{Ever} , is derived:

$$F_{Ever} = \frac{-\delta U_{Ever}}{\delta r} \quad (4.12)$$

The Everaers' derivation for the pairwise interparticle hydrodynamic and vdW potentials uses the following variable definitions:

a	particle radius
r	interparticle center-to-center separation
$A_{CC} \equiv 4\pi^2$	colloid-colloid Hamaker energy pre-factor
$A_{CS} \equiv \sqrt{A_{CC}A_{SS}}$	colloid-solvent Hamaker energy pre-factor
$A_{SS} \equiv 144$	solvent-solvent Hamaker energy pre-factor
r_c	cutoff distance

This mathematical model for hydrodynamic and vdW interparticle potentials is already implemented in the LAMMPS simulation engine. Another potential, defined as the ‘‘Yukawa/colloid’’ potential⁸⁹, is also implemented in LAMMPS in order to define the (repulsive) electrostatic interparticle potential, i.e. the spatial separation force caused by two like charges in proximity. The Yukawa/colloid potential, U_{Yuk} , is defined as:

$$U_{Yuk} = \frac{A}{\kappa} e^{-\kappa(r-d)} \quad (4.13)$$

for particle diameter d , where $(r-d)$ is the interparticle surface-to-surface distance, A is the Hamaker constant⁹⁰, and κ is the Debye length²⁰. When the Everaers' colloid potentials and the Yukawa/colloid potentials are used in conjunction within LAMMPS, the (hydrodynamics and) classical DLVO force described in Eq. 3.11 is recovered, with

$$64\pi R k_b T \rho_\infty \gamma^2 \equiv A \quad (4.14)$$

according to the Derjaguin approximation for interparticle interaction free energy in the spherical case, described by Israelachvili²⁰ (p243).

A final contribution to the hydrodynamic force is the (non-conservative) lubrication force, F_{Lub} , described by Bybee²⁹, is defined as follows:

$$F_{Lub} = -R_{FU} (U - U^\infty) + R_{FE} E^\infty \quad (4.15)$$

For particle velocities / angular velocities U , where U^∞ represents the velocity / angular velocity of the undisturbed fluid, E^∞ represents the rate of strain tensor of the undisturbed fluid with viscosity η , and gap variables R . Combining all the interparticle forces, we now see that the total interparticle force, F_{ij}^{Total} , can be described as:

$$F_{ij}^{Total} = F_{Ever} + F_{Yuk} + F_{lub} + F_{Vincent} + F_{Brown} \quad (4.16)$$

Where

$$F_{Ever} + F_{Yuk} + F_{Lub} = F_{Electro} + F_{vdW} + F_{Hydro} \quad (4.17)$$

we recover the definition for total interparticle force given in Eq. 4.3.

For our simulations of soft-particle systems, atomic/molecular interactions and field effects (hydrodynamics, boundary, and interface effects) are “coarse-grained”, approximated or averaged such that we do not explicitly account for the effect of individual atoms or molecules. Everaers’ and Yukawa’s method for coarse-graining electrostatic and van der Waals effects (DLVO) are very accurate descriptions of the known physics of vdW, electrostatics, and hydrodynamics as applied to colloid systems, some aspects of this system, particularly those involving 1) grafted-polymer coatings used in “soft-colloid” processing, and 2) interfacial and hydrophilic/convective/capillary hydrodynamics effects, are still not completely understood or well-described. We apply Vincent’s derivation of the steric and elastic repulsions caused by polymers bound to the NP surfaces, and an attractive depletion force caused by free polymer in a solvent, to cover case 1. We account for the case 2, we employ empirical fitting of simulation parameters based on experimental results. Such “ad-hoc” application of force models and fitting parameters is a means of including the effects of physical interactions which are not yet fully understood into the simulations, and a tool for understanding those aspects of the system. Edge-effects are usually accounted for with periodic boundary conditions, except in special, noted cases. To analyze our simulations, and directed-assembly in colloids in general, we characterize the individual interparticle and field effects, order, clustering, and randomness in the system of particles as a whole.

IV. ii. Soft-Particle Colloids: The Vincent Model

In this section, we describe Vincent’s derivation of the Flory/Huggins’ theory for polymer/polymer and polymer/solvent interactions applied to the case of spherical colloidal soft-particles, i.e. particles grafted with polymer coatings. We describe the

application of a radial buffer distance to the (Everaers/Yukawa) vdW and electrostatic forces in order which accounts for the effect of these forces being mitigated by or “buried” within the polymer interactions at a particle surface. We illustrate the interparticle potentials and forces at each step of the force-buffering process, and an intuitive “heat-map” colored visualization of the interparticle potentials is used to illustrate examples of both bare-particle and soft-particle colloids. The interparticle “Vincent” potentials/forces have been integrated into LAMMPS (by Ryan Molecke), and used to simulate soft-particle colloids in directed-assembly experiments. A working understanding the Vincent potentials/forces is necessary to tune soft-colloid simulations to experiment, and thereby investigate system dynamics and possible device production methodologies in direct-assembly of nanoparticle colloids.

In the 1985, Vincent described a method for approximating soft-particle depletion, steric, and elastic interparticle potentials caused by biopolymer coatings and free biopolymer in solvent⁹¹. Approximations for interparticle van der Waals and electrostatic potentials were derived by Everaers⁹² and Yukawa⁸⁹, and interparticle potentials describing the Stokesian dynamics of particles immersed in a Newtonian fluid can be approximated according to the “fast-lubrication expedient” described by Bybee²⁹ (described in the previous section). All of these potentials have now been implemented in LAMMPS, and we demonstrate simulations of soft-particle colloids equilibrating in solvent and reacting to dynamic environmental conditions which include these potentials, along with Brownian thermostating, boundary conditions, and interface potentials. We analyze experiment and simulations in terms of particle randomness, clustering, and distribution order parameters, and via TEM images, Fourier transforms of particle

positions or TEM intensities, GISAXS intensity plots, and visualizations of the system. Key parameters are tuned (such as polymer profiles, viscosity, Flory χ parameter, etc...) until simulations are stable, computationally within reach, and match experiment as closely as possible.

Vincent used various historical research based on Flory⁹³ and Huggins⁹⁴ classical model for polymer-solvent dynamics, applied to microparticle coatings. Vincent's model contains three distinct sub-potentials, 1) an attractive "depletion" force caused by a gradient in free (bulk) polymer in the solvent when two soft-particles come within the

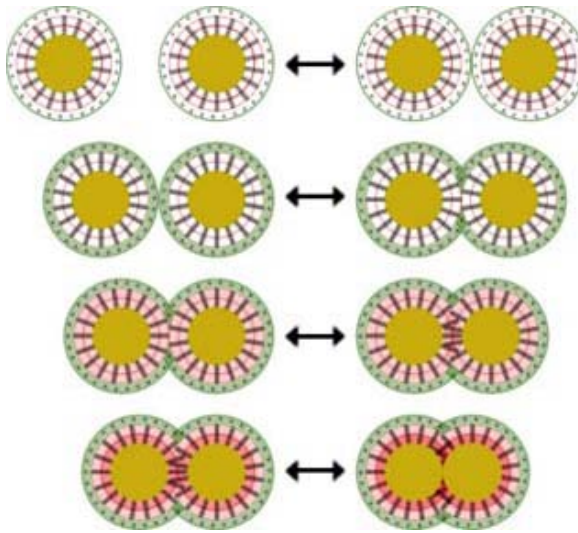


Figure 4.1) Schematic of soft-particles and the range of the three potentials described by Vincent, with green (attractive) depletion range, light red (repulsive) steric mixing range, and dark red (repulsive) elastic mixing range

"depletion distance", 2) a repulsive steric force caused by the biopolymer strands on each soft-particle moving against each other and trying to occupy the same space when the particles are sufficiently close to each other, and 3) a strongly repulsive elastic force which transitions into a hard-sphere potential as the particles grow very close and then touch, this final force is caused by

the bending of polymers as the soft-particles push in very tight next to each other. A schematic drawing of the three interparticle potentials is provided in Figure 4.1.

Below are variable definitions used in Vincent's model:

a = particle radius

d_{buf} = buffer distance which can be added to particle radius

d = particle center-to-center separation

$d_{sep} \equiv (d - 2a - 2d_{buf})$ = particle surface-to-surface separation for spherical particles

p = distance free polymers interpenetrate into adsorbed polymer layer

δ = adsorbed polymer layer thickness

Δ = range of depletion effect

v_1 = molar volume of the solvent

u_1 = chemical potential of solvent at critical flocculation polymer volume fraction

u_1^0 = chemical potential of solvent with no free polymer

$\bar{\phi}_2^a$ = average volume fraction of adsorbed polymer

$\bar{\phi}_2^b$ = average volume fraction of free polymer

$P_2(\bar{\phi}_2^b) \equiv \left(\frac{u_1 - u_1^0}{v_1} \right) \equiv \frac{K_B T}{v_1} (\ln(1 - \bar{\phi}_2^b) + \bar{\phi}_2^b - \chi(\bar{\phi}_2^b)^2)$ = bulk osmotic pressure

χ = Flory-Huggins chi parameter

ρ_2 = adsorbed polymer density

M_2^a = adsorbed polymer molecular weight

Below are the potentials and derived forces for Vincent's model, from longest to shortest range:

1) an attractive “depletion” potential caused by a gradient in free (bulk) polymer in the solvent when two soft-particles come within the “depletion distance”:

where : $2(\delta - p) < d_{sep} < 2(\delta + \Delta - p)$ **(depletion range)**

$$V_{dep} = 2\pi a P_2(\bar{\phi}_2^b) \left(\delta + \Delta - p - \frac{d_{sep}}{2} \right)^2 \text{ for } p < \delta \text{ (depletion potential)} \quad (4.1)$$

$$F_{dep} = 2\pi a P_2(\bar{\phi}_2^b) \left(\delta + \Delta - p - \frac{d_{sep}}{2} \right) \text{ if } p > \delta, p \equiv \delta \text{ (depletion force)} \quad (4.2)$$

where : $0 < d_{sep} < 2(\delta - p), p < \delta$ **(depletion within steric/elastic range)**

$$F_{dep} = 2\pi a P_2(\bar{\phi}_2^b) \Delta \quad (\text{level ‘cutoff’ of depletion force}) \quad (4.3)$$

2) a repulsive steric potential caused by the biopolymer strands on each soft-particle moving against each other and trying to occupy the same space when the particles are sufficiently close to each other:

where : $\delta < d_{sep} < 2\delta$ **(steric mixing only range)**

$$V_{s,mix} = \frac{4\pi a K_B T}{v_1} (\bar{\phi}_2^a)^2 \left(\frac{1}{2} - \chi \right) \left(\delta - \frac{d_{sep}}{2} \right)^2 \quad (\text{steric mixing potential}) \quad (4.4)$$

$$F_{s,mix} = \frac{4\pi a K_B T}{v_1} (\bar{\phi}_2^a)^2 \left(\frac{1}{2} - \chi \right) \left(\delta - \frac{d_{sep}}{2} \right) \quad (\text{steric mixing force}) \quad (4.5)$$

where : $0 < d_{sep} < \delta$ **(steric and elastic mixing range)**

$$V_{s,mix} = \frac{4\pi a \delta^2 K_B T}{v_1} (\bar{\phi}_2^a)^2 \left(\frac{1}{2} - \chi \right) \left(\frac{d_{sep}}{2\delta} - \frac{1}{4} - \ln \left(\frac{d_{sep}}{\delta} \right) \right) \quad (\text{steric mixing potential}) \quad (4.6)$$

$$F_{s,mix} = \frac{-4\pi a \delta^2 K_B T}{v_1} (\bar{\phi}_2^a)^2 \left(\frac{1}{2} - \chi \right) \left(\frac{1}{2\delta} - \frac{1}{d_{sep}} \right) \quad (\text{steric mixing force}) \quad (4.7)$$

3) a strongly repulsive elastic potential which transitions into a hard-sphere potential as the particles grow very close and then touch, this final force is caused by the bending of polymers as the soft-particles push in very tight next to each other:

$$V_{s,el} = \frac{2\pi a K_B T \rho_2 \bar{\phi}_2^a \delta^2}{M_2^a} \left\{ \frac{d_{sep}}{\delta} \ln \left(\frac{d_{sep}}{\delta} \left(\frac{3 - \frac{d_{sep}}{\delta}}{2} \right)^2 \right) - 6 \ln \left(\frac{3 - \frac{d_{sep}}{\delta}}{2} \right) + 3 \left(1 - \frac{d_{sep}}{\delta} \right) \right\} \quad (4.8)$$

(elastic mixing potential) (above)

$$F_{s,el} = \frac{-2\pi a K_B T \rho_2 \bar{\phi}_2^a \delta}{M_2^a} \ln \left(\frac{d_{sep}}{4\delta} \left(3 - \frac{d_{sep}}{\delta} \right)^2 \right) \quad (\text{elastic mixing force}) \quad (4.9)$$

Equations 4.1 through 4.9 assume a uniform polymer density profile and monodisperse spherical particles; the simplest fully examined case from Vincent's paper. The effect of choosing a uniform polymer distribution profile is that the particles might be artificially separated a minute amount more than with other polymer profiles, which can be compensated for by tuning the polymer density variable to a magnitude slightly smaller than the calculated value. For completeness, the Vincent model predicts free diffusion of the particles, i.e. zero interparticle force, where:

$$2(\delta + \Delta - p) < d_{sep} \quad (4.10)$$

At first sight, the sheer number of parameters in this model is daunting, however in practice many of these values are set based on measured or known physical quantities (adsorbed polymer molecular weight and density, Flory χ of the bulk polymer/solvent

pair, solvent molecular volume) and only a few are left to “tune” to the experiment (adsorbed layer thickness, bulk polymer penetration length, range of the depletion effect). The adsorbed/bulk polymer average volume fractions can either be measured (via FTIR or similar means) or approximated to fit an experiment.

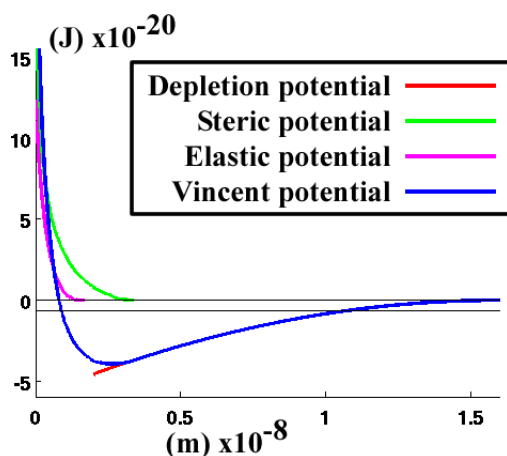


Figure 4.2) Potential vs. surface-to-surface separation for the Vincent model. Particle radius: 10nm, higher coating volume fraction, longer depletion range, higher χ

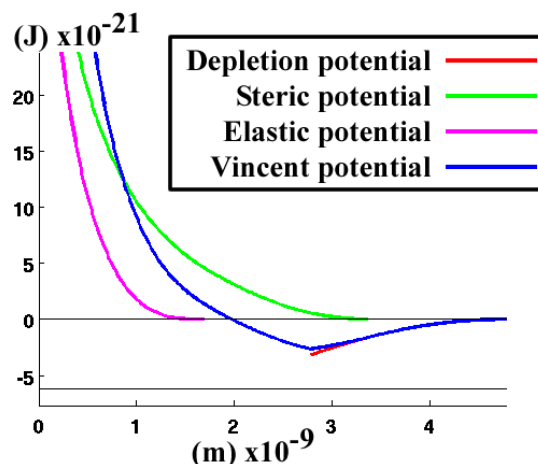


Figure 4.3) Potential vs. surface-to-surface separation for the Vincent model. Particle radius: 5.5nm, lower coating volume fraction, shorter depletion range, lower χ

Figures 4.2 and 4.3 plot the three sub-potentials and their sum, the so-called “Vincent potential” as a function of interparticle surface-to-surface separation. Figure 4.2 corresponds to a 10nm-radius particle with a 12C (26H,1S) alkanethiol coating at 0.14 volume fraction, a 7nm depletion range, and a 0.2 (relatively low) polymer/solvent Flory χ parameter. We assume that the bulk polymer is also an alkane and that the bulk polymer volume fraction is 8%. These are simple test assumptions made to check the model against potential diagrams from Vincent’s paper. Parameters in figure 4.3 correspond to a 5.5nm particle core, with a slightly lower 0.1 adsorbed polymer volume fraction. We have adjusted the Flory χ parameter to match the known value for an alkane/toluene system at 298K, and the depletion range has been changed to 1nm; a

smaller and more reasonable value as it is less than the length of the bulk polymer (1.68nm for 12C alkane). Figure 4.3 shows the dramatic effect of reducing the depletion range. The steric and elastic potentials are generally of similar shape and size in Figure 4.3 (as in Figure 4.2), but the scale of the depletion potential is an order of magnitude smaller, reflected by the need to change y-axis power to “zoom in” on it to capture the full detail.

Tuning the bulk polymer volume fraction, depletion range, and bulk polymer “penetration length” (the length that bulk polymers are allowed to interpenetrate with each other and with adsorbed polymer shells) strongly affects the shape of the attractive potential and thus the overall shape of the cumulative potential. We can make use of this effect to tune the depletion force to almost any theorized shape starting with a light polymer as the “bulk polymer”. We describe how the Vincent potential shown in 4.3 was tailored for use in many of the experiments involving 5.5nm AuNPs in the subsequent sections. Another feature of both Figures 4.2 and 4.3 is the horizontal black line placed beneath the zero on the potential scale, which corresponds to $-\frac{3}{2}K_B T$ (K_B the Boltzmann constant). This energy level corresponds to the average thermal energy of a particle in a homopolar ideal gas at temperature T. Note that in figure 4.3, the net attractive potential is never as large in magnitude as the thermal energy, yet we will see in subsequent sections that even this small potential can strongly influence clustering and ordering across scales. In fact, since the interparticle force is the negative of the *derivative* of the interparticle potential, force doesn’t necessarily depend on the magnitude but only the local slope of the potential curve.

Figures 4.4 and 4.5 demonstrate this point, showing that the force curves corresponding to figures 4.2 and 4.3, respectively. Note that the force is nearly the same magnitude, even though the potentials are of different magnitudes.

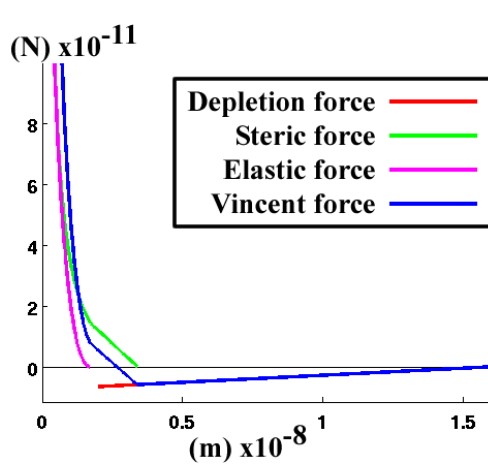


Figure 4.4) Force vs. surface-to-surface separation for the Vincent model. Particle radius: 10nm, higher coating volume fraction, longer depletion range, higher χ

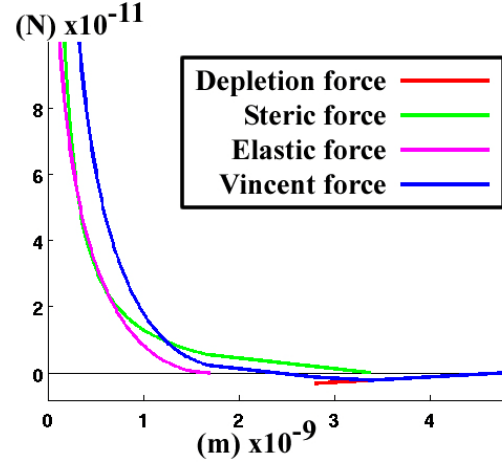


Figure 4.5) Force vs. surface-to-surface separation for the Vincent model. Particle radius: 5.5nm, lower coating volume fraction, shorter depletion range, lower χ

We observe that the forces in these two cases again differ mainly in the range of the depletion effect, noting that figure 4.4 has a distance scale bar one order of magnitude larger than figure 4.5. The apparently linear shape of the force curves is caused by the linear approximation of the adsorbed polymer density profile described by Vincent. Higher orders of the force curve equation could be fully derived, a procedure described by Vincent, but that task is not within the scope of this work. The linear approximations to the force curve are computationally stable and faster to calculate than a higher-order description would, making them sufficient if not ideal for our simulations.

The Vincent potentials/forces describe only the effects of the outer polymer layer and free bulk polymer. For the final simulations, and a more realistic representation of and the actual physical system, the interparticle pair-wise interactions will also include

the electrostatic, van der Waals (vdW), and hydrodynamic forces, which are already integrated into LAMMPS (as described in the previous section). We describe a method for smoothly summing these potentials, where the electrostatic, van der Waals (vdW), and hydrodynamic forces are allowed to interact through, while being mitigated by or “buried” within, the outer polymer.

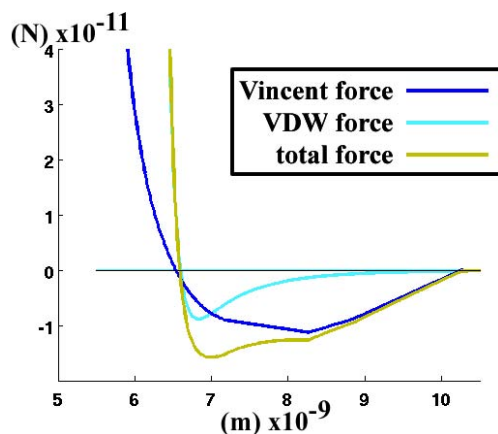


Figure 4.6) Vincent and vdW forces and their sum vs. center-to-center interparticle distance

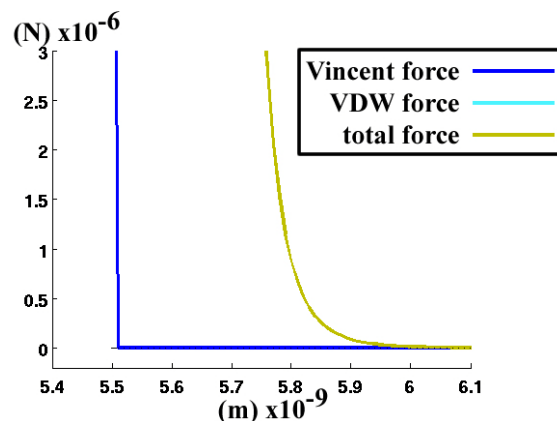


Figure 4.7) Vincent and vdW forces and their sum vs. center-to-center interparticle distance

If we were to just examine figure 4.6, a simple summation of the Vincent force and the (Everaers) vdW force, without considering the shape of the force curve at a different scale, we might conclude that we have done a reasonable job of combining the two radial force curves for our core/shell particle. Both the Vincent and the vdW force curves (Fig. 4.6) cross zero at approximately the same radial distance, and they appear to have the same general magnitude and sum nicely for the total force curve. Once we scale out to the uN force scale, however, things look different. The vdW force dominates the total force curve and creates an artificial hard-sphere-like force asymptote several angstroms outwards from the actual hard-sphere core. To mitigate this effect, we added a variable to buffer the radial distances between the Vincent and vdW forces. This results

in a more realistic physical model where the electrostatic/vdW forces are partially screened by the NP polymer coating and the free bulk polymer. By setting the effective radius of the particle slightly lower than the experimental value, then buffering the Vincent force outwards back to the proper radius, we effectively move the vdW force inwards radially with respect to the Vincent force, changing the relative positions of the cumulative force curves. This procedure “screens” the vdW force, and in some cases completely buries vdW force in the steric/elastic force asymptote of the Vincent force so that the vdW force interaction is negligible.

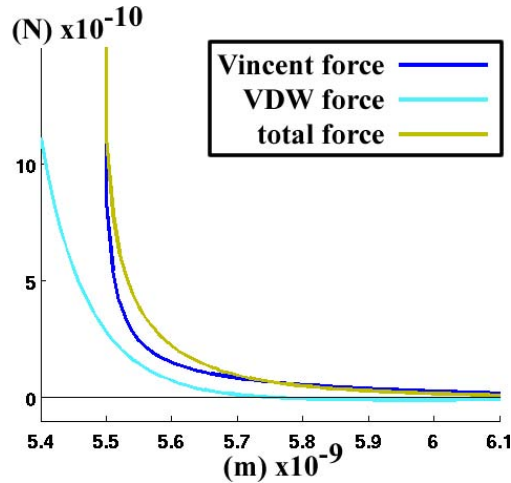


Figure 4.8) Buffered Vincent and vdW forces and their sum vs. center-to-center interparticle distance

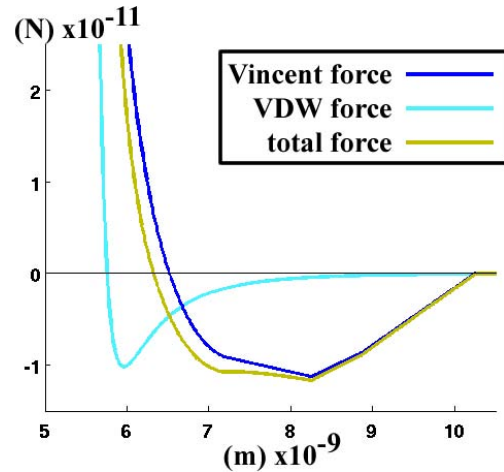


Figure 4.9) Buffered Vincent and vdW forces and their sum vs. center-to-center interparticle distance

Figures 4.8 and 4.9 illustrate the effect of the radial buffering/screening on the vdW force curve. The vdW force curve now reaches only a few hundred pN before the particles would be considered touching (at 5.5nm center-to-center separation, no surface-to-surface separation) because it is buffered inwards into the center of the particle radially. At the hundreds of pN scale, the Vincent and vdW curves are similar in shape and both clearly impact the total particle force shape. The hard-sphere force asymptote

now clearly lies at 5.5nm, the proper/expected radial distance, and is dominated by the Vincent elastic force contribution. In Figure 4.9, at the 10's of pN scale, we can see that the vdW force is somewhat buried into the steric/elastic region of the Vincent force, but still has a clear effect on the total force. Interactions between AuNPs are generally limited to the nN or less range in our LAMMPS calculations because of the high velocities such a force can cause on a single particle in a single time step can cause instability. The 10's and 100's of pN forces are large enough to overtake thermal particle motion and cause clustering/ordering effects in simulation very much like those observed in experiment, supporting the hypothesis that our model approximates the forces of actual interparticle force interactions in NP colloids to within an order of magnitude. This exercise of "buffering" the vdW force against the Vincent soft-polymer core demonstrates clearly the importance of considering the action of all the component forces *across several scales* in order to model accurately colloid systems, and directed-assembly.

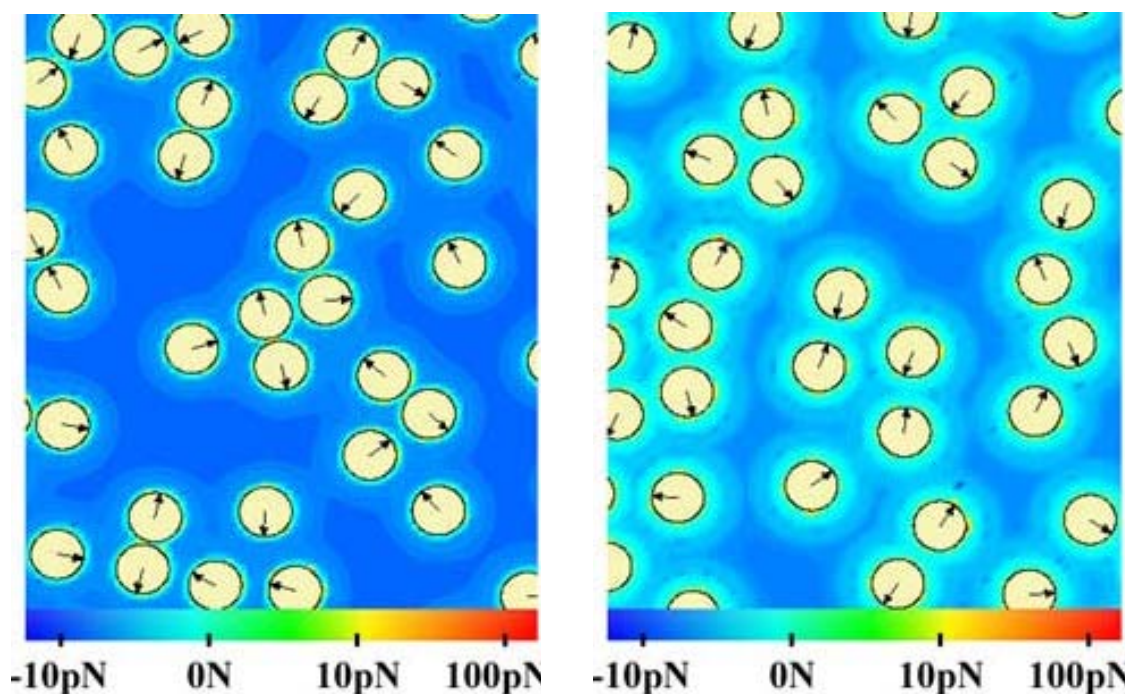


Figure 4.10) Bare particles with vdW potentials heat-mapped into the solvent, with direction (opposing) net force on each particle indicate with arrows

Figure 4.11) Particles with buffered Vincent and vdW potentials heat-mapped into the solvent, with direction (opposing) net force on each particle indicate with arrows

Figures 4.10 and 4.11 are a custom graphical visualization designed to “heat-map” the potential at any given point in the solvent, providing a simple visual verification of the effect of the polymer graft. Figure 4.10 shows the heat-mapped potential for a bare AuNP core, with a narrow ring of interparticle potential around each particle. Figure 4.11 illustrates the potential for alkanethiolated AuNPs (with the force definition from Figures 4.8, 4.9) using to the Vincent model. A much larger ring of interparticle potential exists (viz, a potential of significant magnitude) around each particle. These visualizations are not a scientific tool used to measure any system properties, but just an example of a convenient and visually intuitive way to view the simulated system at any given time step.

IV. iii. Characterization Methods for Soft-Particle Colloids

In order to validate and tune simulations with experiment, several means of characterizing thin films are employed. TEM imaging is an obvious choice, however it is limited by the need for a low-pressure (vacuum) environment, and it is used in stages to view particle positions and sintering/ripening events during the experiment. TEM image intensities can also be transformed via the Fast Fourier Transform (FFT)⁹⁵, implemented as a software tool within the ImageJ program⁹⁶, a freeware Java image processing and analysis applet developed by the NIH *Image* group. Plotting the FFT of an image intensity in 2D space yields 2D “inverse-space” plots, and allows crystal symmetry to be verified and lattice D-spacings (the real-space distances between crystal lattice planes) to be measured very accurately and in a statistically averaged way.

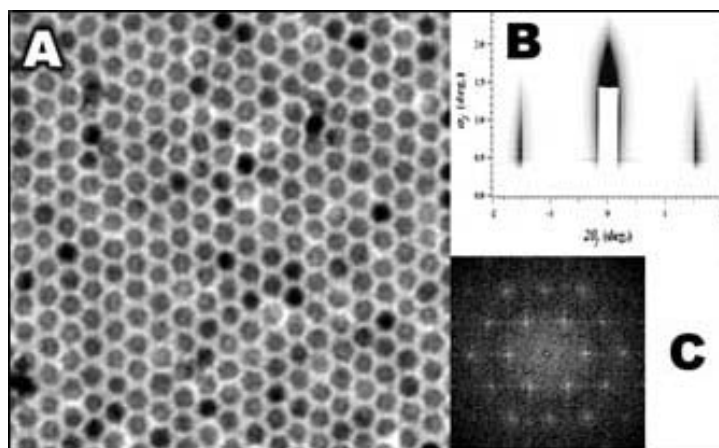


Figure 4.12) A. Section of a TEM image of 5.5nm Au NPs in hexagonal order, B. GISAXS intensity measurement of the film shown in (A), C. FFT of image (A) indicating hexagonal crystal ordering

Grazing-incidence small-angle X-ray scattering (GISAXS) is a characterization method in which X-ray beams are directed at the surface at a small angle of incidence, cause reflection/refraction of the X-rays off any density gradients in a target area, and cast a spatial electromagnetic pattern onto a detector screen in front of the target. GISAXS intensity measurements can be performed in ambient conditions throughout evaporation-induced self-assembly (EISA) of NP lattices within thin-films. We can also calculate GISAXS detector screen intensity patterns via software simulation of GISAXS on arbitrary spatial density profiles, using NANODIFT software developed by the Hillhouse Group at Purdue⁹⁷ (described henceforth as “simulated GISAXS”). Figure 4.12 shows a TEM image and the corresponding GISAXS intensity and FFT plots for a thin film containing a hexagonal lattice of Au NPs at or near the surface. The dark streaks in the GISAXS plot indicate a single monolayer of particles and a sharply defined first peak in the particle distribution, as will become clear when contrasted to simulated GISAXS of similar structures. The bright points in the FFT plot indicate the order of the hexagonal lattice in “real-space”, and their radial distances and orientations can be used to measure and index the average lattice D-spacings. To demonstrate how these plots will change with varying particle structures, we simulate FFT and GISAXS plots using NANODIFT. For any given particle orientation within a cube up to 300x300x300nm on a side, the NANODIFT software takes two to three hours of processor time.

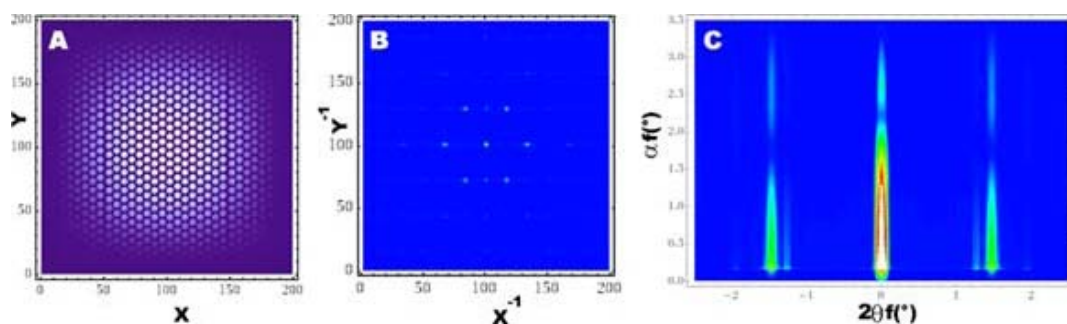


Figure 4.13 A. Real-space density plot showing a single monolayer of particles in hexagonal order (with D-spacing 7nm) B. FFT plot showing hexagonal order, C. Simulated GISAXS intensity plot corresponding to (A)

Figure 4.13 shows a postulated real-space density, with an apodization “window” applied, and the resultant FFT and simulated GISAXS plots, chosen to closely match the TEM image from the experiment described in Fig 4.12. The apodization window is a tapering of intensities near a simulation edge^{98,99} which can be applied to the real-space density plots to reduce edge effects in FFT and simulated GISAXS intensity plots⁹⁷. In the GISAXS plots, α and θ are the angle of X-ray beam incidence with the surface and transverse angle across the detector surface (polar orientation in the Ewald sphere¹⁰⁰), respectively. Figure 4.14 illustrates that increasing the lattice spacing reveals several more peaks in the GISAXS intensity plot. Since the lattice spacing is larger, the peaks in

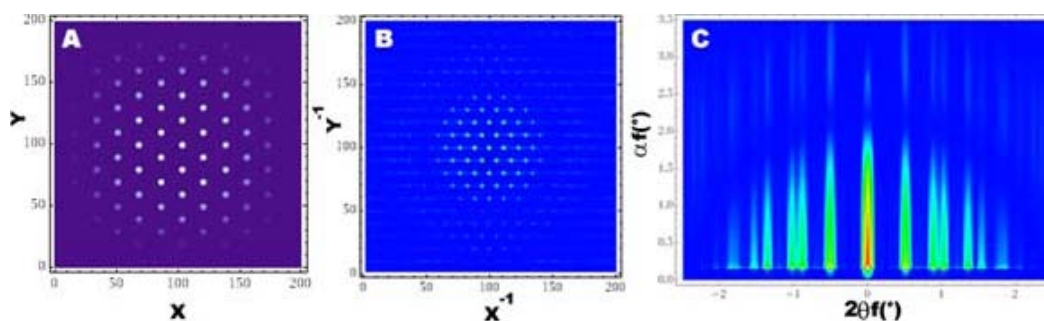


Figure 4.14 A. Real-space density plot showing a single monolayer of particles in hexagonal order (with D-spacing 20nm) B. FFT plot showing hexagonal order, C. Simulated GISAXS intensity plot corresponding to (A)

the GISAXS plot are much closer together and within our simulated detector screen (in an inverse-space relationship).

Transformation with FFT reveals that the structure has not changed in symmetry but now shows the bright points moved closer inwards towards the center, corresponding to a larger D-spacing (in a similar inverse-space relationship).

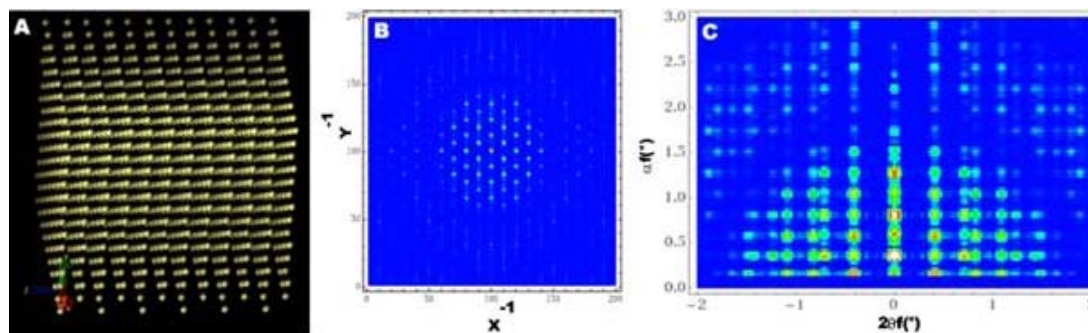


Figure 4.15) A. Real-space density plot showing a 3D array of particles in hexagonal-close packed order (with D-spacing 20nm) B. FFT plot showing hexagonal-close-packed structure C. Simulated GISAXS intensity plot corresponding to (A)

Figure 4.15 shows the effect of adding a 3rd dimension to the crystal structure, with the real-space visualization of a hexagonal-close-packed (HCP) 3D array of particles now generated by Visual Molecular Dynamics (VMD by Humphrey et. al., University of Illinois at Urbana-Champaign¹⁰¹). The FFT now shows two interlaced hexagonal lattices, reflecting the two staggered planes in the HCP crystal structure in real-space. The peaks in the GISAXS plot are now dotted at regular intervals corresponding to angles of beam incidence at which the Bragg condition^{102,103} is satisfied for successive planes in the particle lattice. For reference, Figure 4.16 shows the same particles as in Figure 4.15, after 1ms of virtual ‘equilibration’, which means we allowed thermal diffusion of the 5.5nm particles with buffered Vincent, (Everaers/Yukawa/Bybee) electrostatic,

hydrodynamics, and vdW forces in a toluene solvent in a periodic box at 298K (within LAMMPS).

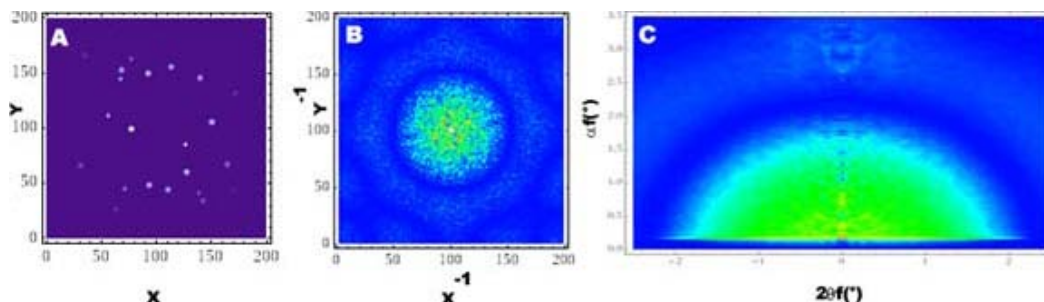


Figure 4.16 A. Real-space density plot showing a 3D box of particles that have undergone equilibration. B. FFT plot showing radial ‘noise’ C. Simulated GISAXS intensity plot corresponding to (A)

The now randomized particle positions are reflected by radial ‘noise’ in the FFT and simulated GISAXS plots, indicating random particle distributions at all distances larger than the particle diameter.

Another tool at our disposal for characterizing particle positions is the Ripley’s K function and associated family of spatial statistical tests for randomness vs. clustering. The Ripley’s K function is essentially the “radial distribution function” (RDF¹⁰⁴) averaged over particle number and the expected radial spatial intensity for a random distribution of particles (see Appendix 2). In Ripley K plots, the bottom curved line represents the K-values for a system with complete spatial randomness among the particles, where the top line represents the K-value calculated from the RDF of the particle coordinates of interest, i.e. the degree of clustering. If the top line sharply turns upwards at a specific radial distance, that means the particles are relatively clustered at that distance. If the top line dips downwards or falls below the bottom (randomness) line at a given radial distance, that means there is a relative absence of particles with that

distance to their neighbors. The diverse and multidisciplinary usefulness of the Ripley's K test is evidenced as we borrow algorithms from software packages for the statistical analysis of protein chain reactions and for mapping neural synapse communication to extend the 2D Ripley's K test into 3D. For the 3D Ripley's K test, the k-function (a normalized measurement in histogram form of how 'clustered' the particles are over increments of radial separation) is squared and the random distribution expectation now grows within spherical shells rather than the 2D analog of circular shells. Figure 4.17 (a) illustrates how the K-value (top line) varies in magnitude for radial distances out to 40nm, for a hexagonally close-packed (HCP) array of 6nm particles in periodic 3-space with a lattice constant of 20nm. The crystal structure is reflected in the jagged K-value line, which indicates regularly spaced neighbors and absences of neighbors among the particles as would be expected in a system with crystalline order.

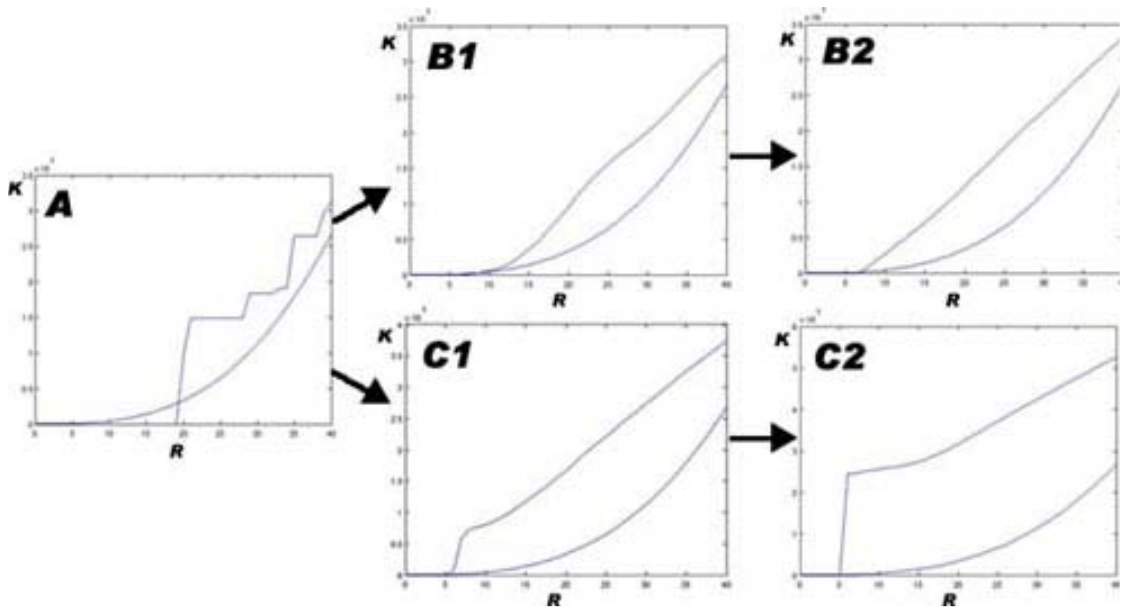


Figure 5.17) A. Ripley K plot for HCP array of NPs B1. Plot for semi-equilibrated system. B1. Plot for equilibrated system. C1. Plot for semi-clustered system. C2. Plot for strongly clustered system

When this system is allowed to equilibrate, it follows path (b) in Figure 4.17, eventually losing the original form and becoming a straight line upwards, indicating a negligible amount of clustering. When this same simulation is run with the conditions of increasing bulk polymer fraction and increasing viscosity (strong attractive interparticle force, limited mobility), it follows path (c) in Figure 4.17, and the K-values become left-shifted and sharply curved, indicating strong clustering of the particles at 6-7nm.

We can plot the RDF of a set of particle coordinates as a histogram and track the RDF over time in a simulation, for an intuitive and easy-to-read plot of average radial particle distances. Figure 4.18 shows the RDF plotted at intervals throughout an “evaporation” simulation in 2D, where a number of 5.5nm diameter particles are compressed very slowly in a contracting box. In this case, the box edge speed over the mobility of the particle represents the Peclet number of the system¹⁰⁵, and this system is set to a relatively low Peclet number (where the edge moves very slowly with respect to the particle mobility) such that the particles are allowed to “equilibrate” to their environment relatively well at each time step. We plot the RDF in blue at the beginning of

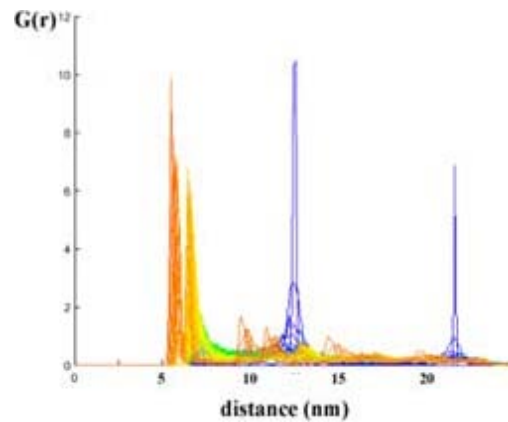


Figure 4.18) Radial distribution function plot of evaporation stage of simulation

the simulation and change color through the rainbow to red as the simulation progresses in time. The red and yellow peaks at the left of this image reflect the phenomenon of the particles assuming hexagonal order. Any defects in the long-range order “zip” together as we very slowly ease the 2D area fraction up to a final value (88%) just a few percent

short of the theoretical “close-packed” limit of 91.6%. As the particles reached closer and closer to the theoretical packing limit, the interparticle force is far up the hard-sphere force asymptote and the Brownian motions cause great differences in the interparticle forces from one time step to the next, with the result that the simulation becomes unstable at or slightly above 88% area fraction.

Another indispensable tool for characterizing thin-film colloids is X-ray reflectivity, where the electric vertical field intensity (EFI) distribution and corresponding electron density profile of a film can be calculated from X-ray intensity as functions of incident angle and film depth. Ellipsometry, a closely related experimental measurement technique, can also be used to measure and verify film thickness measurements from reflectivity. Figure 4.19 shows the graphed data from a paper (reproduced with permission) in which Xiong et al. perform and describe such X-ray reflectivity and ellipsometry measurements. In this experiment, 5.5nm AuNPs with 12C alkanethiol coating in a PMMA/toluene solvent are deposited (by Xiong et al.) at room

temperature onto a water surface and allowed to dry into a thin film, which is then transferrable and even self-supporting over cover-slip notches up to several square centimeters in area. This AuNP/polymer ‘matrix’ film is transferred onto a Si substrate for reflectivity and ellipsometry measurements. The peaks in the reflectivity and

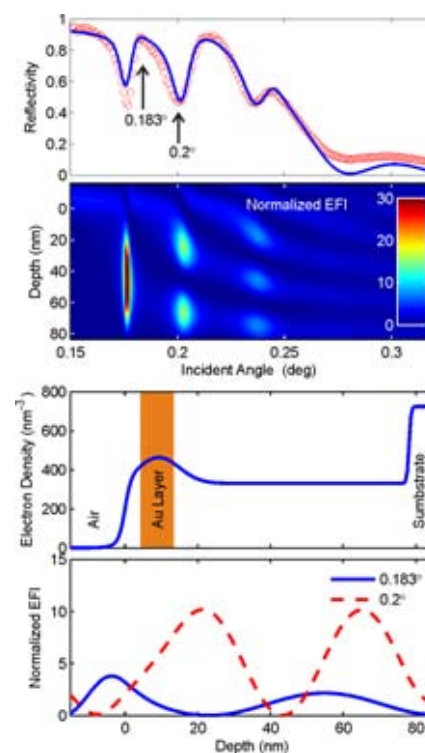


Figure 5.19) Reflectivity for NP/polymer array and fitted EFI

normalized EFI indicate a single layer of AuNPs has formed very near or even in contact with the top air-solvent interface of the film. LAMMPS supports a somewhat crude approach to simulating such interface (flat planes with normal exponential force). In the case of particles trapped in a monolayer, however, we can account for the interface by merely restricting the particles to a 2D plane.

By running thermal equilibrations of particles trapped in 2D planes at varying area fraction, and correlating experimental and simulated GISAXS plots taken at intervals over time, we confirm that a strong attractive interface force exists (this is the subject of section 3) and is dominant over the other forces in the system. The attractive interface force therefore drives the assembly of ordered structures in this system. We postulate that the interface force is the result of evaporation-induced or convective flow of the solvent towards the interface during drying, capillary wetting phenomena in the menisci between the particles at the surface, and a polar/non-polar hydrophobic-like repulsion of mixing between the alkane particle coating and the toluene solvent which causes the particles to become trapped at the air interface once they reach it. These interface forces are theorized to strongly influence clustering and ordering in NP colloids, and a more explicit description of them and programmatic inclusion of them into LAMMPS is a current and future research goal.

We describe our preliminary attempts to extend the simulations to three dimensions and account for interface effects. These simulations attempt to account for the effect of particles “skinning” on the top surface in a single, HCP monolayer. We illustrate the results from a “plowing” simulation in which we move a virtual air interface layer downwards through a field of particles in solvent. We move the air interface downwards

much faster than the mobility of the particles (relatively high Peclet number) causing them to become trapped at the moving wall interface in a layer. This is admittedly a naive method for simulating evaporation since simple plowing does not take into account local evaporative flow currents caused by solvent molecules leaving the liquid system (and driving flow in an uneven way based on local surface geometry) or capillary effects. In fact no surface geometry (other than a flat plane) is currently supported in LAMMPS, but extending it for this purpose is a future research task. Another shortcoming of the plowing method is that particles will only “skin” the top layer in a double-layer, as shown in Figures 4.20 and 4.21, whereas in experiment a single layer forms. Getting a full covered of particles in a top layer (double-layer or not) in the plowing simulations was extremely challenging.

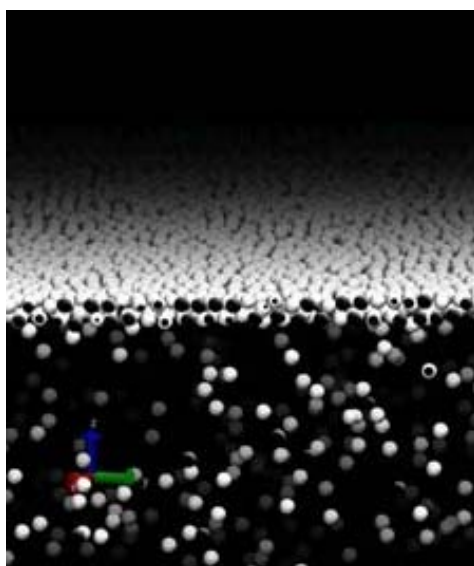


Figure 4.20) 3D Plowing simulation with low viscosity, top-angled view

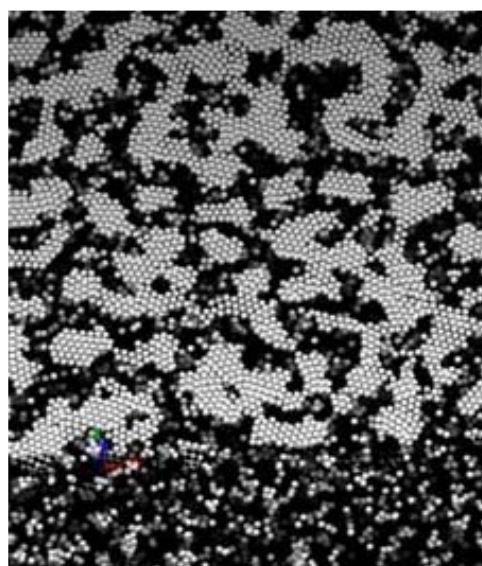


Figure 4.21) 3D Plowing simulation with parabolic viscosity gradient, top-angled view

In 3D plowing simulations with a low viscosity (the book value of toluene) the particle skinned the surface completely with a double-layer; however the packing density was not great enough that the particles were forced into hexagonal order (as in the experiment). In simulations where the viscosity was allowed to rise (as the toluene solvent evaporated and the PMMA set up into a gel-like solid state), the particles would form more dense layers on the surface, however the simulations were very unstable and would crash as a triple-layer would start to form in some places and eventually cause an unstable force interaction with the wall or other boundaries. Although these 3D simulations do not match the experiment, they do demonstrate the ability to run simulations with thousands of soft-particles and microscale box sizes in reasonable amounts of time with LAMMPS. They also show the first steps towards a more fully real 3D simulation of a NEMD colloid directed-assembly experiment, and were used in the development of the relevant characterization tools: RDF, Ripley's K, FFT and simulated GISAXS intensity plots.

This concludes the discussion of the Vincent model for interparticle potential in soft-particle colloids and the description of methods we will employ for characterizing thin-films. The Vincent model has been incorporated into LAMMPS, and several MATLAB, Mathematica¹⁰⁶, and C++ tools have been developed to aid in performing characterization of colloidal thin-films. While a certain level of software mastery is necessary to direct these tools, actually tuning simulations and interpreting them can be an art, and we must define rigorously every process of guiding a given simulation from beginning to end to extract meaningful results. Subsequent sections describe the application of these methods (simulation, visualization, spatial statistics, FFT, and

GISAXS) can be applied to a variety of experiments to investigate colloid and thin-film dynamics and NP ordering phenomena in particular as it relates to directed-assembly.

IV. iv. Interface-Driven Order in Soft-Particle Colloids

In this section, we apply LAMMPS simulations of soft-colloid evaporation-induced self-assembly (EISA) experiments in which long-range HCP order arises among AuNPs at a thin-film surface. By matching GISAXS intensity plots taken at intervals during experiment and simulations, we confirm that a strong attractive interface force exists and show that it is dominant over the other forces in the system and therefore drives the assembly of ordered structures in this system. This is an example of realistic simulation of soft-colloid systems to characterize the dynamics underlying a series of actual EISA experiments performed by Xiong, et al.¹⁸. In the next section we describe characterization and simulation of a similar set of experiments, also by Xiong et al., in which the EISA process is followed up by an irradiation step causing the AuNPs to sinter/coalesce into nano-wires/rods, as an example of directed-assembly of nanoparticle colloids.

So-called “bottom-up” assembly in colloids offers the potential to choreograph the organization of atoms, molecules, and nanoparticles (NPs) and to tailor device functionality across a range of scales. Colloid and thin-film processing is an established science which has evolved with modern advances in NP production⁵²⁻⁵⁵, active biopolymer coatings^{9,10,48,54,65,70,71,73}, sol-gels^{16,64}, EISA^{12,15,18,19,58,75,76}, new theoretical paradigms²⁰, and exponentially growing computational resources available for simulation and modeling²¹. Colloids and thin-film processing are quickly becoming integral fields within nanoscience, driving markets for nanotechnology products. Recently, thin-film

assemblies of nanoparticles superlattices have generated great interest as possible device components with customizable electronic^{2,6,107}, optical^{61,62,69}, bio-active^{10-15,52,53,55,56,58,59,68,71,73}, or catalytic properties^{52,53,60,69} based on particle size/s, composition, and polymer coating.

Recent studies in NP superlattices formed by evaporation-induced self-assembly (EISA) demonstrate robust monolayers, bilayers, and higher-order systems. Xiong et al.'s recent series of experiments with 5.5nm AuNPs in toluene/PMMA solvent¹⁸ are an example of a system for which the Vincent model for soft-particle interparticle interactions within colloids (cf. section V. ii.) is applicable. Xiong's method for evaporation-induced self-assembly (EISA) of self-supporting, AuNP-containing polymer matrix thin films starts with the deposition of a solvent mixture of Toluene/PMMA containing 12C alkanethiolated 5.5nm-diameter AuNPs onto a water surface, where it spreads and dries into a thin polymer matrix film. As the Toluene evaporates and leaves the system, the PMMA molecules within the solvent become partially cross-linked and are also held in place by ionic bonding, allowing the PMMA to "set up" from free bulk polymer in the liquid-phase to a gel-like or rubber-like state. This system is of particular interest for subsequent processing via a release or application of induced stress, or via irradiation with high-energy electron beam since PMMA in this thin-film matrix form is soft, expandable, and stimuli-responsive not only physically to electron irradiation but as a photoresist both positively and negatively for varying UV photon wavelengths. The method of using induced stresses and deformation of a stimuli-responsive polymer matrix substrate with embedded AuNPs can be regarded as a processing step for controlling

geometry and order among colloidal NPs, and a step towards the creation arbitrary designed networks within systems of colloidal NPs.

Figure 4.12 is repeated to illustrate the final structure in one of Xiong's EISA experiments with 5.5nm AuNPs, described above. The AuNPs shown in Figure 4.12 (a) are known to be at or near the air/PMMA interface within the thin film that is formed during the Toluene evaporation by X-Ray reflectivity (inferred from normalized electric field intensity distributions, described in section 2). Figures 4.12 (b) and (c) show the result of a GISAXS experiment and the FFT of the intensity of image (a), respectively, both of which indicate near-perfect hexagonal ordering among the AuNPs.

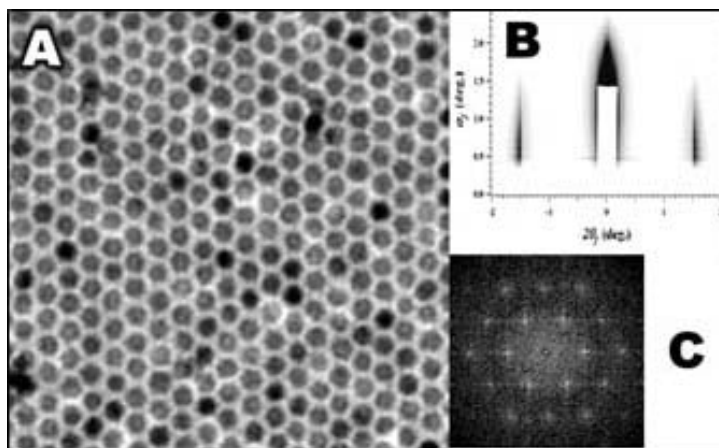


Figure 4.12) A. Section of a TEM image of 5.5nm Au NPs in hexagonal order, B. GISAXS intensity measurement of the film shown in (A), C. FFT of image (A) indicating hexagonal crystal ordering

Figure 4.22 shows a more comprehensive analysis of the GISAXS experiments performed while the Toluene/PMMA/AuNP mixture spread and evaporated on the water surface. The red text near the top of Figure 4.22 indicates the moment that the mixture was deposited from the pipette onto the water surface. From the time-series GISAXS intensity plots, we see that two broad peaks form gradually from a noisy radial pattern

from the moment the particles are released until approximately the 75-second mark, and then quickly become well-resolved into two sharper peaks between 75 and 95 seconds. This indicates that the particles are gradually building up on the surface (with common spatial distributions within clusters of particles) until a saturation point is reached where the particles can be

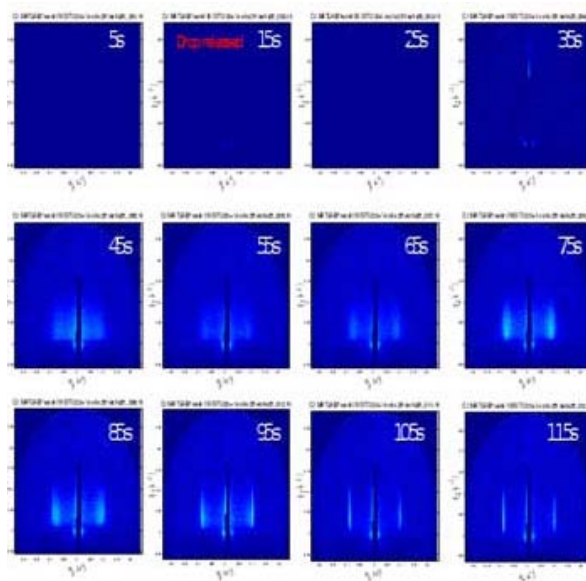


Figure 4.22) Time-series of GISAXS experiments performed on AuNP in Toluene/PMMA-solvent EISA evaporation on water interface (reproduced with permission).

considered hexagonally ordered. The lack of significant lateral movement of the two peaks within the GISAXS intensity time-series indicates that only a small amount of final ordering and compression occurs as top monolayer of particles assume a “saturated” packing density within the 2D hexagonal matrix of AuNPs trapped at the air interface.

Figure 4.23 shows the results from a series of GISAXS simulations performed on particle distributions that represent the end time steps from sixteen LAMMPS simulations of 12C alkanethiolated 5.5nm AuNPs in Toluene/PMMA solvent at 298K. In these simulations the particles are trapped in two dimensions to account for the effect of the strong attraction between the AuNPs and the air-interface caused by polar/non-polar hydrophobic-like repulsion of mixing between the alkanethiols and the Toluene. Each LAMMPS experiment consisted of a simple thermal equilibration of the particles (no dynamic effects) at area fractions ranging from five to eighty percent. There is strong

correlation between the final images in this sequence (area fraction 60% and above) between the simulated GISAXS series and the actual GISAXS time series (for 65 seconds and above). The radial noise in the simulated GISAXS at low volume fractions, and lack of radial noise in the corresponding GISAXS time-series, is caused by the added precision of calculating the GISAXS from known coordinates (and artificially reduced interfacial roughness) in the simulation, however both plots indicate a degree of

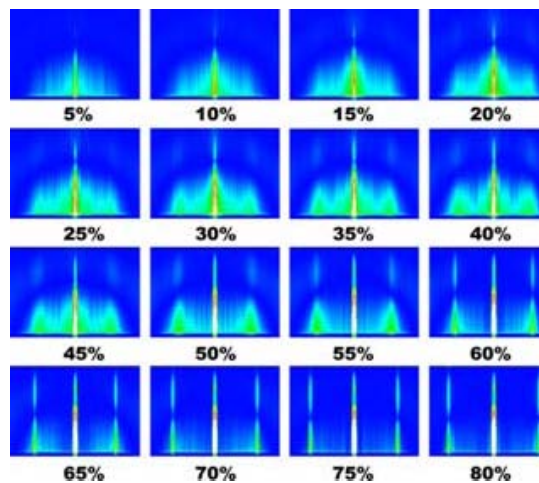


Figure 4.23) Progression of simulated GISAXS performed on virtual alkanethiolated AuNPs in Toluene/PMMA-solvent at varying 2D area fractions

ordered clustering in these states with low area fraction of particles at the interface.

The rising profile and increasing resolution of the peaks in the simulated/experimental GISAXS intensity plots corresponds to particles clustering and ordering at the surface faster than would be expected if the AuNPs were randomly diffusing to the surface and away from the surface at equal rates. This indicates that the area fraction of particles at the air-solvent interface is being driven disproportionately higher than the bulk volume fraction (projected in 2D) by an attractive potential between the interface and the particles. This attractive interfacial potential has already been theorized to exist, and is thought to contain force component contributions from solvent evaporative or convective flow towards the interface, capillary forces in the menisci between the particles at the surface, and polar/non-polar hydrophobic-like mixing repulsion between the alkanethiols and the Toluene solvent. Our LAMMPS simulations

demonstrate the effects of such a force, which indicate validity of the Vincent model for modeling soft-particle colloid systems and interface-driven order in EISA of polymer-matrix thin-films. Close matching between simulated and experiment GISAXS demonstrates that the NANODIFT software can be used to effectively characterize simulations, “tune” simulations to match or reflect experimental measurements, and infer physical forces related to ordering and assembly in colloidal thin-films.

We use MATLAB data visualization to demonstrate the effects of Flory χ parameter and bulk polymer volume fraction on our model for total interparticle force, since these actual system properties are likely to change in Xiong’s EISA experiment as the Toluene evaporates and the PMMA “sets up” into a film. In Figures 4.24 and 4.25, we form surface plots from the total interparticle force versus particle separation, with Flory χ or bulk polymer volume fraction as our third axes, respectively. The total interparticle force includes electrostatic/hydrodynamic forces from Everaers/Yukawa and depletive, steric, and elastic polymer-induced forces from Vincent, with the vdW forces buffered into the core of the particle to account for reduction in the longer-range vdW force effects because of the polymer coating (as described in section IV.ii).

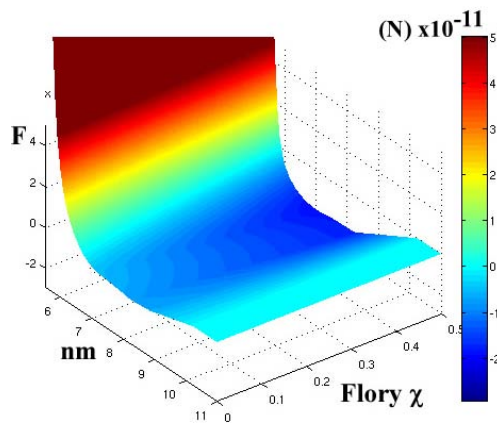


Figure 4.24) Interparticle force versus center-to-center particle separation and Flory χ parameter

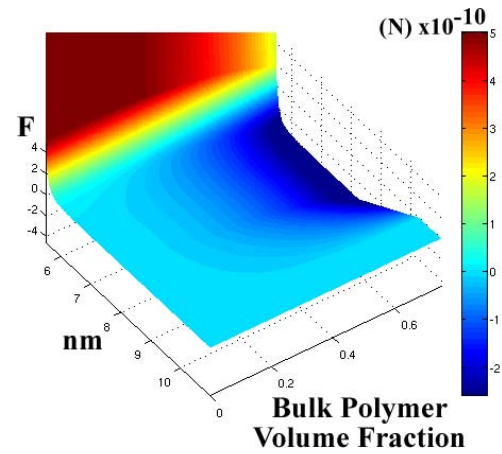


Figure 4.25) Interparticle force versus center-to-center particle separation and bulk polymer volume fraction

Figure 4.24 shows the hard-core interparticle force asymptote (red) and the attractive region (blue) on the force surface as it changes with increasing Flory χ parameter, in the tens of pN range. Figure 4.25 shows that a much stronger attractive region and shorter-range, sharper hard-core force asymptote form with increasing bulk polymer volume fraction, as the forces now have to be plotted in the hundreds on pN range for a similar surface shape. During our series of 2D LAMMPS simulations at increasing area fractions, we set the Flory χ parameter artificially higher than the known value for Toluene-alkane interactions to allow the particles to cluster/order with shorter separations. In this regard, the Flory χ parameter can be considered a tuning variable that allows us to effectively account for some attractive force caused by capillary forces, even though capillary forces are not explicitly included in our models. This artificial increase in Flory χ parameter for surface particles is also supported by the reasoning that the alkanes will have a higher χ parameter as they leave the Toluene/PMMA system and poke out into the air above, and could be bending and interacting with curved capillary surfaces between the particles. The bulk polymer volume fraction was not allowed to increase over our simulation of Xiong's EISA experiment because we found that this resulted in the average particle separations smaller than those observed in the experiment. In light of this result it may be theorized that bulk polymer volume fraction is not changing considerably at the surface or that the model for depletive attraction is not complete / over-predicts interparticle attraction in such systems driven by interface dynamics.

We use the Mathematica NANODIFT package FFT plots for the evolving real-space density of the system as we step through the intervals of increasing area fraction.

Figure 4.26 illustrates the real-space intensity plots, with apodization window applied, and corresponding FFT plots. We observe strong clustering in the particles at 20% area fraction, and can even make out some slight hexagonal shape to the FFT plot at this early stage. By the time we reach 50% area fraction, the FFT indicates a sharp ring implying the particles have assumed a first peak in their common nearest-neighbor distances, but have yet to show strong long-range hexagonal order. Within the 5% interval between 55% and 60% area fraction, the clusters of particle merge or coalescence and the system “locks-in” to long-range hexagonal order, indicated by the appearance of the bright spots in the FFT pattern. At 75% area fraction, which corresponds to the measured distances in Xiong’s experiment, the FFT shows that system has much more defined hexagonal order, and the FFT spots have moved farther from center, indicating that the lattice spacing has been fractionally reduced from that of the original hexagonal lattice formed at 60% area fraction.

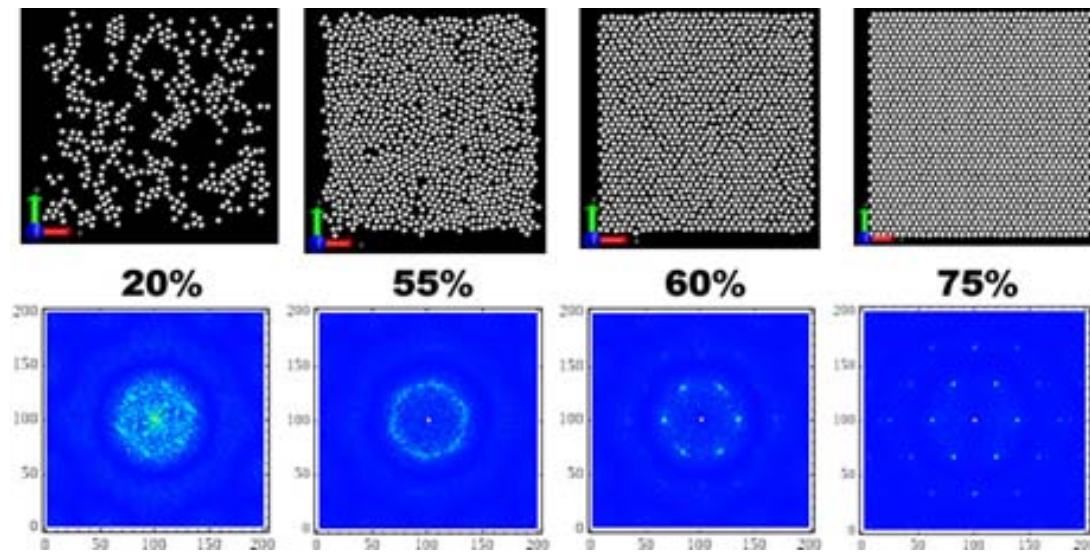


Figure 4.26) Plots of particle positions within a 2D box, real-space (top row) and inverse-space or FFT (bottom row)

In summary, we have implemented Vincent's model for soft-colloid interparticle interactions into LAMMPS and successfully applied it to simulate the 2D case of particles trapped in a monolayer at varying area fractions, reflecting the conditions of Xiong's EISA experiment. FFT, GISAXS, and simulated GISAXS all support the explanation that particles are randomly diffusing to the surface, where they become trapped and experience attractive interparticle forces, causing monolayer clusters of particles to form at the surface. This monolayer of clusters increases in area fraction as new particles diffuse to the surface, until a coalescence of clusters forces the particles into a hexagonally-packed monolayer. Finally, new particles continue to force their way into the grain boundaries in the hexagonal order at the surface until a tightly-packed (HCP) monolayer forms. At high concentrations of particles in the bulk solvent, layers of particles can become trapped above or below the monolayer, or layer "stacking" can occur. We have demonstrated how LAMMPS simulations including Vincent's model, NANODIFT GISAXS intensity plots, and FFT plots can help characterize and explain soft-colloid dynamics under EISA conditions.

IV. v. 2D Array Rearrangement using a Stimuli-Responsive Substrate

In this section, we describe a method of “directing” a solution of biopolymer-coated gold nanoparticles into nanowire formations through evaporation-induced self-assembly followed by unique thin-film transfer and subsequent irradiation steps. We review how ordered nanowire structures are formed through evaporative, vapor-liquid-solid interface dynamics, polymer/solvent interactions, and physical deformation caused by irradiation. We extend this research with device considerations, simulation, characterization, and statistical analysis. We match realistic discrete-element simulations to experiments in directed-assembly of soft-colloids to identify underlying physical system dynamics. Experimental and simulated fast-Fourier transform (FFT) and grazing-incidence small-angle X-ray scattering (GISAXS) intensity plots show in-plane ordering and lattice properties in colloid surface films to sub-nanometer precision and allow characterization of interparticle potentials, including hydrodynamics, electrostatic, vdW, and polymer/solvent potentials, and phase-interface effects. We advance a parallel discrete-element simulation code, LAMMPS, to investigate interparticle and phase-interface potentials and long-range ordering phenomena relevant to directed-assembly of nanoparticle colloids. We employ classical statistical tests to particle coordinates over simulation time-sets to shed light on clustering and ordering phenomena. We describe how experimental and simulated grazing-incidence small-angle X-ray scattering intensity plots allow characterization of soft-colloid particle formations with sub-nanometer precision.

We report the formation of an anisotropic nanorod/nanowire structure by directional aggregation and room temperature sintering of a free-standing 2D close-

packed nanoparticle/polymer array self-assembled and transferred from an air-water interface. Molecular dynamics simulations of alkanethiol capped Au NPs, interacting through the Vincent potential and undergoing 1D Poisson compression accounts semi-quantitatively for the qualitative features of the transformation. Upon E-beam irradiation the suspended PMMA film undergoes uniaxial retraction and breaks the isotropic symmetry of ‘hard sphere’ packing. Moreover, after the capping ligands on nanoparticle surface have been depleted due to mechanical compression, surface tension drives 5.5-nm Au sintering into anisotropic structure at room temperature. The oriented, ordered, and large area nanorod/nanowire array has a critical minimum feature size of about 6nm, which is below that of state-of-art lithography. On the macroscale, metal-like anisotropic electrical conductivity has further been demonstrated over large areas and over a range of temperatures. The individual steps of this nanofabrication approach are completely compatible with existing nanomanufacturing practices and suggest that this approach could be extended more generally to other nanoparticle systems

Two-dimensional (2D) nanoparticle arrays or superlattices are of physical and chemical interest as analogs to their crystalline counterparts assembled from atoms. To date, well developed colloidal chemistry enables fast and facile synthesis of metallic¹⁰⁸, semiconductor^{109,110}, and magnetic nanoparticles¹¹¹ (NPs) with precise size and shape control. Further entropy driven self-assembly of monodisperse and binary NPs¹¹²⁻¹¹⁵ has resulted in ordered arrays in which collective electronic, magnetic and optical properties can be tuned through electron charging and quantum confinement of individual NPs mediated by coupling interactions with neighboring NPs. Despite considerable progress on developing structural perfection of NP arrays, their analogy to atomic solids breaks

down with respect to electron transport. Because NPs are stabilized with dielectric organic ligands, NP arrays are insulators and behave as an array of isolated Coulomb islands unless sufficient field strengths are applied to achieve electron tunneling (ref include Brinker et al.'s Science paper plus paper within it). To facilitate electron transport for optoelectronic applications, tremendous effort has been aimed at: modifying the insulating organic capping layer by ligand exchange, thermal annealing to neck adjacent nanoparticles¹¹⁶, or even metal chalcogenide complexation and conversion to semiconductor phases upon gentle heating, generating inorganic nanocrystal solids¹¹².

An alternative approach to achieve efficient and directed energy or electron transfer is the assembly of anisotropic low-dimensional nanoscale building blocks. However, to date, only limited successful examples have been reported. For example, externally applied fields¹¹³ or hydrodynamic/fluidic strategies¹¹⁴ have been employed for orientation of nanorods in solution, and individual nanoparticles have been oriented into 1D structures by preferential attachment in solution¹¹⁵ or pressure-driven assembly at an interface¹¹⁷ or within a polymer matrix¹¹⁸. Despite recent advances, precise control of alignment and fabrication of dense nanorod assemblies remains a significant challenge especially over large length scales.

Here we report the formation of a large scale ordered and oriented Au nanorod array by transformation and coalescence of an ordered close-packed gold nanoparticle/polymer monolayer¹¹⁹ via constrained uniaxial deformation and room temperature sintering induced by electron beam irradiation. This approach results in high densities of integrated single crystal like nanowires that exhibit directional metallic conductivity on the macroscale.

2D Au NP/polymethylmethacrylate (PMMA) monolayer arrays (e.g. Fig 4.27A) were prepared by dispersion of 5.5-nm diameter, 12C alkanethiol stabilized NPs dissolved in a solution of toluene plus PMMA on a water surface. Briefly, 50~150 mg of nanoparticles were dissolved in 6 mL of toluene containing 100 mg of poly (methyl methacrylate) (PMMA, Mw = 996000, Aldrich). To prepare the NP/polymer monolayer, one drop (about 7-10 μ L) of the NP/PMMA/toluene solution was carefully dispensed onto the surface of de-ionized water contained in an uncovered 5-inch Petri dish. After drying for minutes, monolayer arrays were transferred onto a half piece of 100 mesh copper grids by vertical Langmuir-Shaefer lifting of substrate, to minimize tearing of the sample in plane. The as-assembled nanoparticles array was hexagonal close-packed, with d-spacing between 1L and 2L (L is the length of 1-dodecanethiol as capping ligand on surface of Au nanoparticles). Nanoparticle layer are sitting on top of the supporting polymer layer, without polymer among the interdigitating ligands. The films have a thickness in the range of 70-100 nm determined by profilometry and ellipsometry.

Evaporation induced self-assembly confined to a fluid interface results in a large area ordered NP/PMMA monolayer¹⁸ that was transferred¹²⁰ to a trenched structure, resulting in a

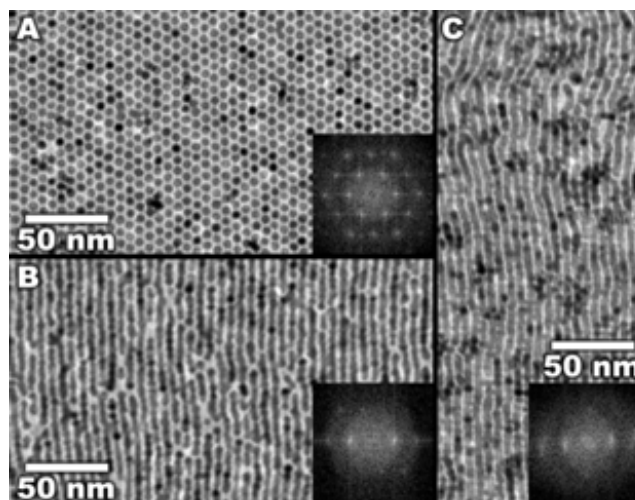


Figure 4.27) (A) TEM image showing large-area hexagonal close-packed Au NP/PMMA monolayer array prepared by interfacial assembly. (B) Typical chain-like nanostructure formed by irradiating the free-standing NP/PMMA monolayer array under E-beam for 1 min. (C) Ordered Au nanowire array formed after further aging at RT for 7 days.

constrained, freely suspended film with one free edge (schematic in Fig 4.29A). AFM and x-ray reflectivity experiments showed the NPs to reside exclusively at the original polymer/air interface (as opposed to within the 50-nm thick polymer film or at the original polymer/water interface). The suspended films were then subjected to E-beam irradiation employing current densities in the range of 30-200 pA/cm² and an accelerating voltage of 200 kV (See supporting information). TEM imaging (Fig. 4.27) showed that E-beam irradiation causes uniaxial contraction in the direction normal to the free edge, accompanied by only a modest expansion in the corresponding normal direction (Fig. 4.27B). After about 1 min, the NP d-spacing was reduced by 20% in the unconstrained direction, forming chain-like aggregates (Fig. 4.27B, sometimes proceeding through a square planar intermediate, depending on the NP orientation, as shown in Fig. S2). Further aging at room temperature without E-beam irradiation resulted in a more uniform and fused nanowire-like array, with rod lengths extending up to several hundred micrometers (Fig. 4.27C).

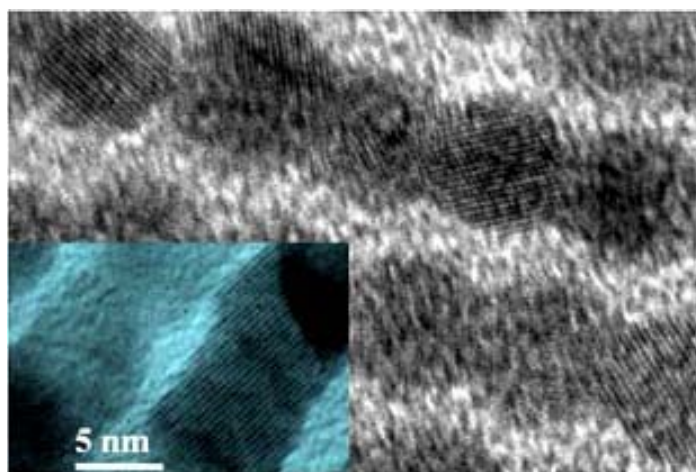


Figure 5.28) High resolution TEM images demonstrating the initial random configuration of the chainlike aggregates and the single crystal like rods (inset) that form upon room temperature aging.

High resolution TEM imaging showed that the nascent NP aggregates were randomly oriented (Fig. 4.28), but upon aging they coalesced and re-oriented into single-crystal-like nanorods (Fig. 4.28 inset). In comparison, for completely unconstrained free-standing films, similar retraction was observed, but the d-spacing decreased uniformly in all directions, preserving the hexagonal arrangement of the NPs. For unsupported oleic acid-stabilized CdSe/PMMA monolayer arrays formed as for Au and E-beam irradiated in a similar fashion, linear aggregation occurred but without any observable NP fusion.

To explain our experimental results, we propose that E-beam irradiation of PMMA, a positive tone E-beam resist, results in chain scission, reducing its molecular weight and modulus of elasticity. The reduced modulus allows residual stresses that develop upon drying of the transferred film and capillary stresses acting on the protruding NPs to direct aggregation in the unconstrained direction normal to the free edge. Conservation of volume is achieved by expansion in the interchain spacing and material transfer to the underlying polymer film. Given such a short irradiation time, mass loss of polymer is negligible¹²¹.

Films resting on the substrate and free standing films with a free edge (while the other three edges are immobilized on support) behaved differently under a series of E-beam irradiation. Thin film sample was irradiated by e-beam with current density in the range of 30-200 pA/cm² and accelerating voltage of 200 kV for minutes. The e-beam irradiation dose thus applied is comparable to that utilized in regular positive-tone patterning of PMMA. The E-beam dose effect has also been investigated. When we focused the beam and irradiate the film with high current intensity above 1000 pA/cm², random coalescence took place and generally network structure formed.

Finite element simulations of the bench-scale process (Figs 4.29 A and B) reveal a substantial area of uniform, constrained uniaxial compression, with edge effects (where substantial mixed, shear deformation occurs) confined to the outer perimeter. The simulations were of a quasi-static elastic solid material of the dimensions of the pre-irradiated film (100 nm x 3 mm x 5 mm). The process of drying and residual stress redistribution was predicted using pre-stress and mass-loss terms in a Lagrangian framework. The mesh, being Lagrangian in nature, follows the motion of the elastic network, indicating a uniform compression over a large portion of the film (as shown is Fig. 4.29B). Because the Au NPs reside at the polymer surface we expect their trajectories to be well predicted by the simulation.

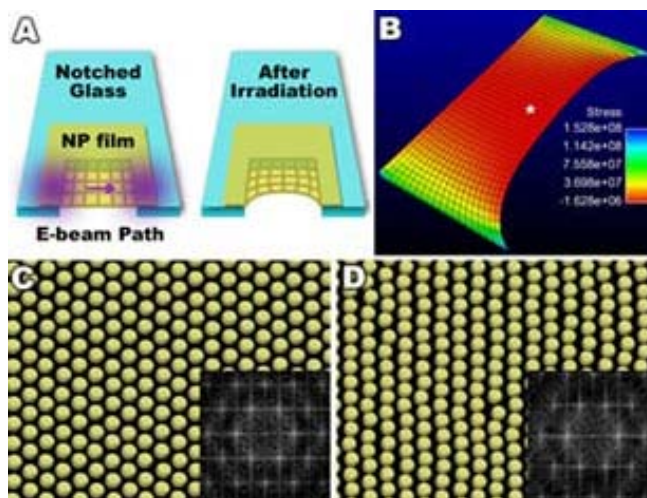


Figure 4.29) (A) Schematic shows original film configuration and the retraction (upon E beam irradiation) of suspended nanoparticle/polymer monolayer array with a free edge. (B) In plane axial normal stress in receding direction as predicted from a Lagrangian finite element simulation of residual stress relief due to volume change. The white star on this plot indicated the relative position of the micro-domains modeled in LAMMPS in the polymer film (C) Molecular dynamics simulation of original NP/polymer array and (D) Formation of nanowires by anisotropic Poisson compression.

To visualize the one-dimensional deformation of the close-packed NP monolayer at the NP scale, we used a molecular dynamics code LAMMPS⁸³ with polymer/solvent/particle interactions incorporated in the Vincent potential, based on Flory-Huggins theory derived for spherical, polymer-coated particles, that accounts for 1) bulk-polymer induced depletion, 2) polymer-polymer steric repulsion, and 3) polymer-polymer elastic repulsion. DLVO,

polymer, and lubrication forces are all coarse-grained to enable multi-scale simulations much larger than DFT or molecular methods can permit; in order to simulate the aspect of sintering, particle diffusivity is artificially restricted and maximum inter-particle force is limited during compression such that the particles are forced to overlap slightly. Fig. 4.29C shows a simulated 2D close-packed array of 5.5-nm diameter alkanethiolated Au nanoparticles formed from a dilute solution of NPs in toluene/PMMA by solvent removal and equilibration at 298K. Subjecting the closed packed monolayer to a simulated one dimensional Poisson compression with Poisson ratio= 0.1 (based on the aspect ratio of the deformed Lagrangian mesh) and corresponding to that of a near-perfectly compressible solid, results in the formation of chain-like aggregates whose orientation depends on that of the parent close packed array. Comparison of TEM and FFT of both the experimental and simulated systems (Figs 4.27 and 4.29) show good agreement, suggesting that the simulation captures the essential physical parameters of self-assembly and one dimensional deformation into chain-like aggregates.

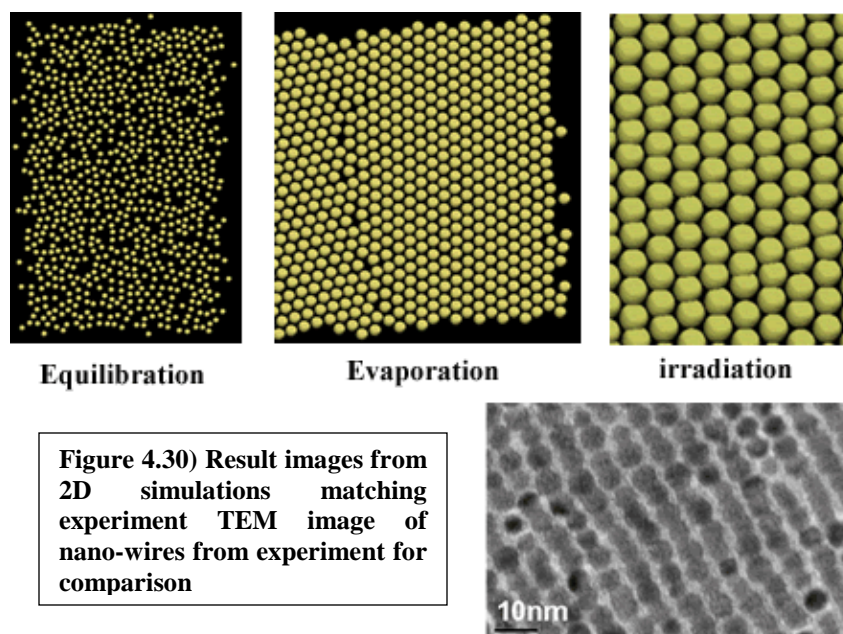


Figure 4.30 shows the results from 2D simulations of soft-particles run on up to 32 processors in parallel on the ‘nano’ Linux cluster at the UNM Center for Advanced Research Computing. The particles were started in hexagonal order and given 2 million time steps (10 picoseconds per time step) to equilibrate in solution. The domain was then slowly compressed up to 75% area fraction under changing solvent conditions to simulate the drying process (increasing viscosity, increasing bulk polymer concentration, increasing Flory chi parameter). Irradiation and pre-sintering of the gold particles was achieved by a slow uniaxial compression (with particle remapping) of the simulation box, while the maximum force the particles could exert on each other was set artificially low and the solvent viscosity artificially high. Under these conditions, final linear structures are formed which match the results of the thin-film experiment. In order to more closely visually match the experiments, it was found necessary to tune the Poisson ratio of the 2D simulations to 0.1 as shown in Fig. 4.29D, as opposed to the system with Poisson ration 0 as shown in Figure 4.30, and also to allow the particles to very slightly “coalesce” by compressing them into oblong shapes uniaxially, in a transverse direction to the film compression.

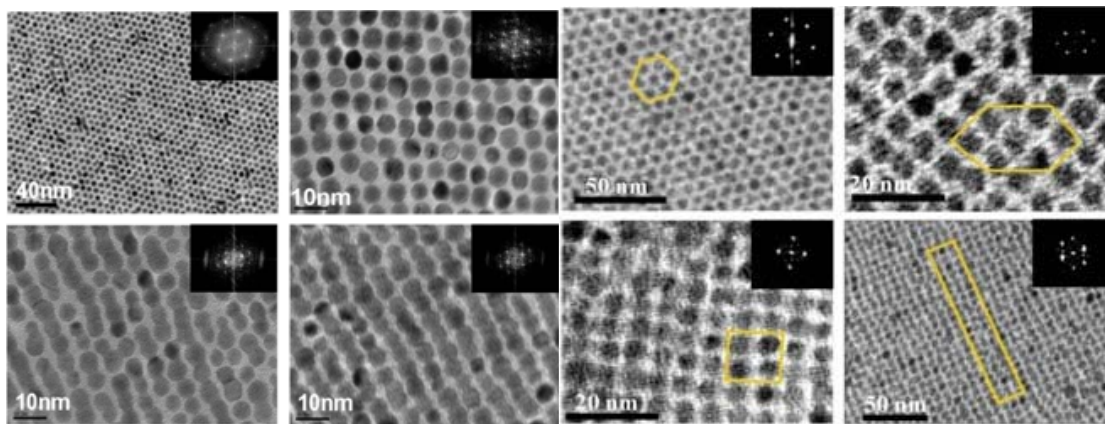


Figure 4.31) Left: Evolution of Au NP/PMMA monolayer array under E-beam irradiation. Right: Evolution of PbS/PMMA monolayer array under E-beam irradiation (PbS capped with oleic acid, 5nm core size). The insets show the FFT of respective TEM images.

To understand this phase (arrangement) transformation induced by external stimulus, a simple mechanical model can be applied. Well known as a positive E-beam resist, high molecular weight PMMA has been scissored into short chain and low molecular weight PMMA, with Young's modulus significantly lowered during the E-beam irradiation. If a force is to be thought of as holding a section of the film taught due to pre-strain in the film there will be a stress throughout this section of the film. This film will therefore have some amount of strain due to the applied force. Since stress and strain are related through the following equation: $\sigma = E\varepsilon$, if the young's modulus (E) of the film is reduced then the longitudinal strain in the film will increase if the stress in the film is to remain constant and due to this longitudinal elongation, the film will experience a lateral contraction.

PbS QD/PMMA monolayer arrays were also prepared using the same method as Au NP/PMMA monolayer arrays and then transferred onto a trenched glass slide, then irradiated under E-beam. The arrangement of PbS QDs changed accordingly. Hexagonal close-packed (HCP), deformed HCP, and quasi-cubic close-packed, as well as large area of pearl-chain structure were observed dependent on different compression angle, as shown in Figure 4.31. Unlike the Au NPs, there was no sintering evident due to higher melting point of PbS QDs.

To understand the further particle coalescence into single crystal-like nanorods at room temperature, we recognize that the location of the NPs at the polymer vapor interface facilitates depletion of thiol ligands from regions between the approaching particles¹²². Ligand depletion allows nascent particle-particle contact and ensuing sintering driven by the high curvature that increases surface tension of Au and

accordingly the sintering driving force¹¹⁹. The reduced mechanical constraints also enable concurrent NP reorientation needed to achieve a single crystal like interface between adjacent particles. Sintering and coarsening continue at room temperature until a rod-like structure evolves (Fig. 4.27C and 3 insets) that minimize differential curvature and interfacial energy. Capping ligand on Au NP surfaces was proposed to sublime before fusion of NPs¹²³, and thermogravimetric analysis verified the removal of thiol during annealing¹²⁴. However, the separation of nanorods indicates the preservation of stabilizers and excludes the thermal effect.

The anisotropic rod-like Au nanostructures formed by E-beam irradiation and room temperature aging as in Fig. 4.27C were characterized electronically with a linear four-probe setup over the temperature range from 80 to 300K. For these measurements the inside two probes were separated by about 50~200 μm . The I-V plot (Fig. 4.32 inset) acquired at room temperature shows linear, Ohmic behavior in the direction parallel to the rod orientation with resistivity determined to be 5k $\Omega\cdot\text{nm}$ (nearly comparable to that of polycrystalline Au nanowires¹²⁵: 1k $\Omega\cdot\text{nm}$)

while in the normal direction the array was insulating over the measured range of potential bias (for this probing distance, a much greater voltage needs to be applied to reveal the Coulomb blockade effect¹²⁶).

The irradiated sample showed a dramatic change in conductivity before and after the room temperature aging process. The

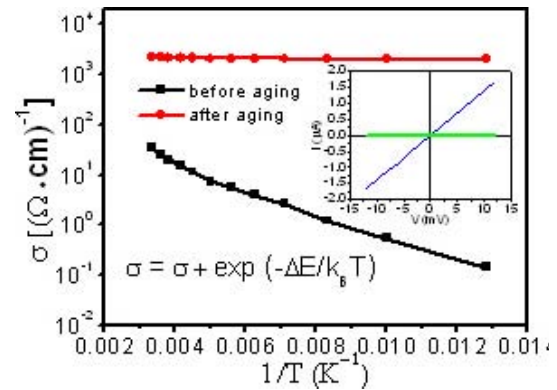


Figure 4.32) Temperature dependence of conductivity measured for E-beam treated NP film before and after aging process. Inset: I-V behavior (at 300K) for irradiated and aged film along the retracting direction (in blue) and in the normal direction (in green).

Ohmic I-V behavior and conductivity of the anisotropic nanostructure after complete sintering and coarsening is independent of temperature, as expected for a metal. However, for the as-irradiated sample without aging, $\log(\sigma)$ was found to vary nearly linearly with $1/T$, corresponding to an effective activation energy of 3.8 meV. This is consistent with that of electrons hopping across the grain boundaries of the quantum islands¹²⁷.

Large scale ordered and oriented metallic nanorod arrays, exhibiting highly anisotropic electrical conductivity, were formed by one-dimensional deformation, re-orientation, and sintering of a free-standing close-packed gold NP/polymer monolayer at room temperature. As the individual unit operations, viz. self-assembly, transfer, and e-beam irradiation are all scalable and compatible with traditional semiconductor miniaturized platforms, this approach might be generally applicable for the fabrication and integration of dense, large area, anisotropic nanostructures.

The final part of the colloid assembly section will focus on some proposed devices that could theoretically be manufactured using EISA and directed-assembly via induced strain or stimuli-responsive materials, and some discussion of which experimental parameters could be tuned for future experiments aimed at building possible prototype devices. The first proposed possible device is a super-capacitor with nanoscale charge elements as shown in Figure 4.33. In this, and all of the devices proposed, a lithographic patterning step is performed on the particles while they

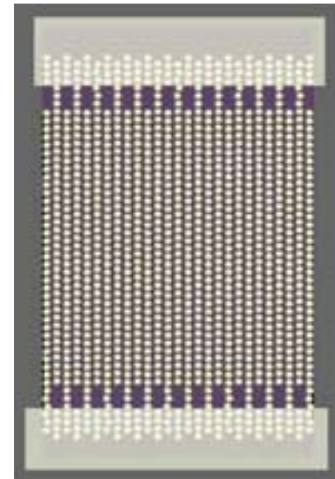


Figure 4.33) nanoscale super-capacitor

are in hexagonal order, to create an ordered pattern of particles that is then compressed into the final device during the irradiation deformation step. This capacitor device is somewhat unrealistic because it 1) assumes perfect long-range order in the particles, 2) permits no lateral “touching” between nanowires as per the electrical requirements of a capacitor, and 3) would require the ability to (lithographically or otherwise) create vacancies at almost the resolution of the particles themselves to produce the device. If we accept that we cannot get perfect long-range HCP ordering of the particles during evaporation (owing to dislocations and varying orientations of the hexagonally packed areas within the particle matrix), we can design devices that will not require such high resolution lithographic patterning or perfect ordering.

Figure 4.34 shows how an arbitrary wire work can be formed by irradiating a patterned gold nanoparticle film, producing a device with characteristic features at half the size of the resolution of the lithographic process. This method could be used to

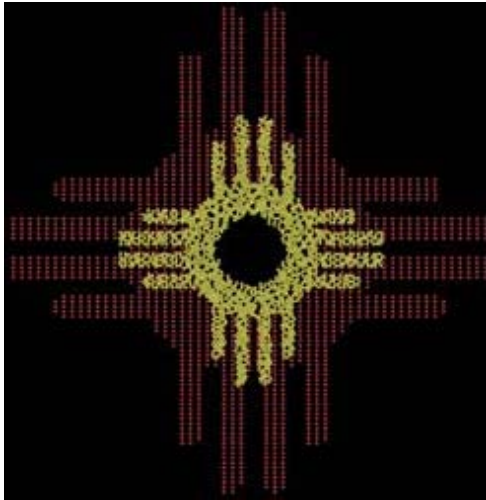


Figure 4.34) Zia pattern, red (post lithography), gold (post irradiation)

produce resistors, inductors, capacitors and complex interconnect networks for nanoelectronics devices. This method does not require perfect hexagonal ordering in the evaporated AUNP film (in fact it seems to work better with a small amount of disordering), and can improve on lithographic patterns of any size, since the particles themselves are scalable. These device images

are actually quite remarkable because they do not contain a scale bar: the technology itself is fully scalable down to 5nm or possibly even smaller.

Using this device production methodology as a guide, we see that the process could be improved with the ability to make the film shrink in two directions (as opposed to the uniaxial compression demonstrated), but this is a challenging goal because the shrinkage happens under the electron beam, which has to be in high vacuum, and the film is very fragile and can already barely gap the small notch in our glass cover slip. Finding a method of supporting the film in a way that it can contract freely, or finding a substitution for the PMMA (polymethyl-methacrylate) that could contract in more amenable conditions could be considered, yet we need to retain the property that our substrate polymer matrix still be a photoresist for our lithographic patterning step. Another aspect of the experiment we could change is to try to make the film contract more either by using a different polymer, activation method, or possibly simply by induced physical stresses (physical stretching/relaxation or compression). More contraction means the final device will be smaller compared to the lithographic resolution in the patterning process, and also ensures that the device has full connectivity in all areas where the particles are supposed to compress together into wires. Finally, the ability to increase the biopolymer length in relation to the particle radius would mean a greater long-range order in the evaporation step, and again improve the device feature size ratio to the lithographic resolution in the patterning step, however this will sacrifice the final connectivity of the structure if the longer biopolymer coatings prevent the particles from compressing into wires.

In conclusion, a directed-assembly experiment was described and the underlying physical processes discussed. A comprehensive theoretical model was chosen and implemented into a high-performance simulation engine, and physical parameters of the experiment used as inputs. Two-dimensional simulations of equilibration, evaporation, and irradiation NEMD dynamics yielded ordered structured nearly identical to those seen in the experiment. Three-dimensional simulations performed represent a first step towards a more complete simulation regime, and highlight the need for more explicit treatment of advanced flow and vapor-liquid-solid interface dynamics. Simulation outcomes were analyzed with simple spatial distribution statistics, and more advanced analysis methods are in production. New types of devices and manufacturing methodologies were proposed, with a focus on how current experiments can be altered or improved towards the end of producing a prototype device. This research shows incredible potential for the production of devices with highly controlled nanoscale features, and a clear path for improving device resolution to less than the size that any lithographic process alone can achieve.

IV. vi. Characterization of Binary Nanoparticle Superlattices

Recent work on nanoparticle superlattices, and notable recent publications by Murray et al. on binary nanoparticle superlattice (BNSL) geometries⁷⁵, represents a new step forward in soft-colloid processing and the field of “bottom-up” or directed-assembly in general. Colloidal nanoparticle superlattices can theoretically be used to tailor the directed-assembly of scalable, arbitrarily complex and interconnected multi-layered structures composed of a multiple particle types each having custom chemical, biologically or environmentally-responsive, electronic, or optical properties^{75,76}. Tuning the sizes, shapes, and particle compositions in BNSLs has been shown to be a fast and inexpensive path for interface-driven order in NP colloids, and many lattice geometries have been demonstrated corresponding to various ratios of nanoparticle radii (for spherical particles) or variety in the NP shapes. Colloidal nanoparticle lattice geometries can be partially predicted by classical crystallographic space-filling and space-group theory, while simulation of soft-particle colloids, clustering and order analysis, FFT plots, and GISAXS experiments and simulations are all valuable characterization tools which can yield insight into underlying physical processes and possible device design avenues. We demonstrate a matching of experimental and simulated GISAXS intensity and FFT plots for a BNSL formed by EISA of 14.5nm diameter Fe_3O_4 and 5.3nm diameter Ag particles in a toluene/PMMA solvent. Linear analysis (plots across row or column) of the GISAXS intensity data can be used to match theorized structures to experimental structures to verify and characterize particle lattice geometries. The software tools we use for our visualizations, simulated GISAXS⁹⁷ and FFT⁹⁶ plots are widely available, and

demonstrated to be applicable for research involving nanoparticle superlattices, and directed-assembly in general.

In an EISA experiment performed by Dunphy and Xiong (2010), 14.5nm diameter Fe_3O_4 and 5.3nm diameter Ag particles coated with alkanethiol in a toluene/PMMA solvent were deposited by pipette onto a water surface and the PMMA set up into a thin film as the toluene evaporated from the system. The Fe_3O_4 and Ag particles are known to be located at or near the solvent-air interface, and are thought to be trapped from diffusing away from the interface once they reach it because of evaporative/convective flow as the toluene leaves the system, polar/non-polar hydrophobic-like repulsive mixing interactions between the alkane coatings and the toluene, and capillary forces. GISAXS experiments were conducted on colloids containing just the Fe_3O_4 particles, and colloids containing the mixture of Fe_3O_4 and Ag particles. The structures are thought to form the AB2 crystallographic lattice geometry.

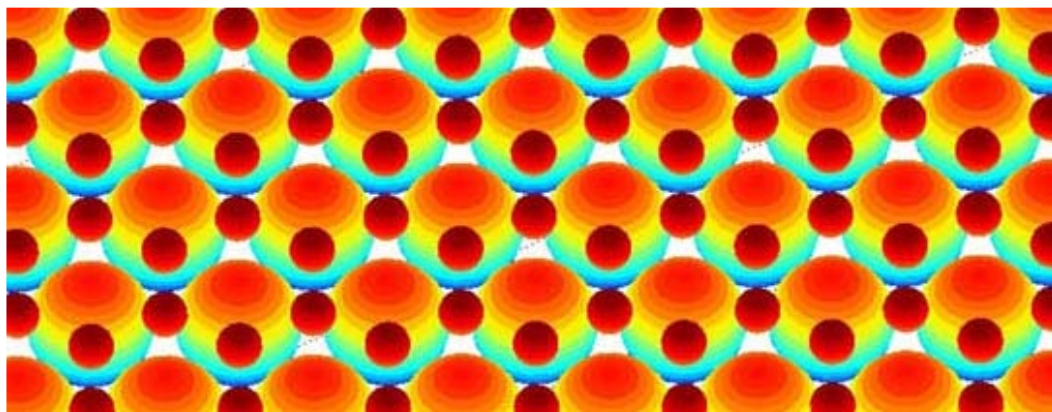


Figure 4.35) MATLAB ‘bubble plot’ of the 3D geometry of an AB2 lattice composed of 14.5nm particles and 5.3nm particles with 1.8nm particle spacing

Figure 4.35 shows a 3D visualization (made using MATLAB) of the Fe_3O_4 / Ag BNSL structure, where the particle spacing between each neighboring Fe_3O_4 particle pair has been set to 1.8nm, a reasonable approximation for a such a soft-particle colloid assuming a 12C alkanethiol particle coating. The particle spacing between neighboring Fe_3O_4 / Ag particle pairs has also been set to 1.8nm under the same approximation. The distribution of the Ag particles is not defined by a single distance, but by their positions in the interstices of the underlying hexagonally-packed lattice of larger Fe_3O_4 particles (according to the AB2 crystallographic unit-cell geometry). Our goal is to confirm the AB2 lattice geometry and approximate particle spacing via matching of simulated GISAXS and experimental GISAXS. It is instructive to start with the simpler case of the system containing just the Fe_3O_4 particles, shown in Figure 4.36.

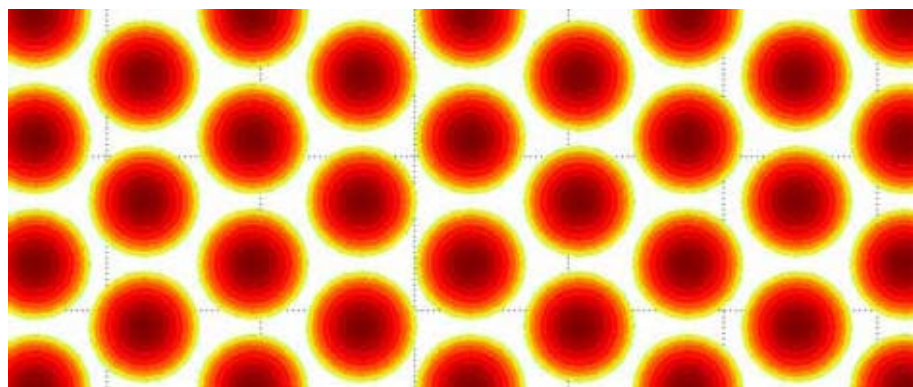


Figure 4.36) MATLAB ‘bubble plot’ of the 3D geometry of a hexagonally-packed monolayer of 7.5nm diameter Fe_3O_4 particles with 1.8nm interparticle spacing

Figure 4.36 represents the approximate geometry that the Fe_3O_4 particles are theorized to assume during the EISA experiments, whether or not the Ag particles are present. Figure 4.37 is the simulated GISAXS plot for the structure (shown in Fig 4.36), generated using the NANODIFT extension to Mathematica and some custom C++ scripts by Molecke. A qualitative agreement can be observed between figure 4.37 and 4.38,

which is the actual plot of experimentally measured GISAXS intensities for this system. The experimental system shows more ‘noise’ because, presumably because the particles are not in perfect order whereas our simulated particles are set in perfect order. The main features, such as relative peak heights and intensity gradations, indicate that our simulation represents the correct lattice geometry and approximate spacing between the particles.

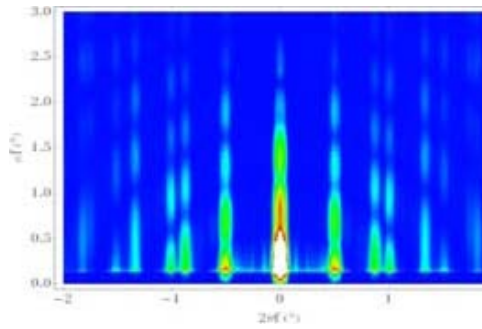


Figure 4.37) Simulated GISAXS of a hexagonally-packed monolayer of 7.5nm diameter Fe₃O₄ particles with 1.8nm interparticle spacing

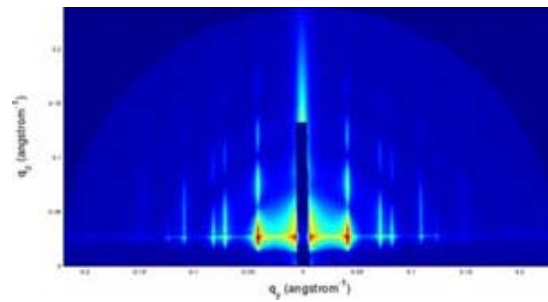


Figure 4.38) Experimental GISAXS from Dunphy and Xiong’s EISA experiment with alkanethiolated 7.5nm diameter Fe₃O₄ particles in toluene/PMMA solvent

Figures 4.39 is a row plot of the simulated GISAXS intensities from the simple hexagonally-packed structure (shown in Fig. 4.36), taken at the value of $\alpha f(^{\circ})$ corresponding to the bright ‘baseline’ in the GISAX intensity plot. Figure 4.40 is a column plot taken at the value of $2\theta f(^{\circ})$ corresponding to the first intensity peak right of center. The extension of our graphical analysis to include these linear “cuts” from the GISAXS intensity data allows us better precision and another graphically intuitive tool for matching theorized and experimental geometries and interparticle distances.

Figures 4.39 and 4.40 illustrate linear plots through horizontal rows and vertical columns of the simulated GISAXS intensity plot, which are useful for analysis of

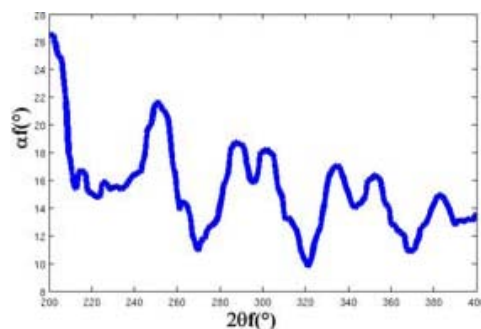


Figure 4.39) row slice from the 'baseline' of the simulated GISAXS of a hexagonally-packed monolayer of 7.5nm diameter Fe₃O₄ particles with 1.8nm interparticle spacing

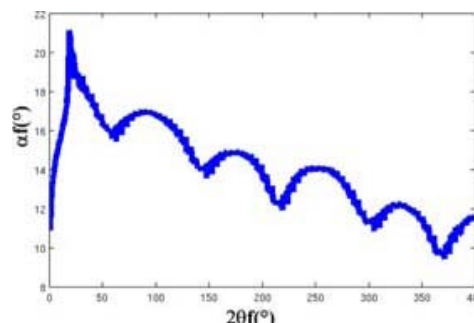


Figure 5.40) column slice from the first intensity peak right of center in the simulated GISAXS of a hexagonally-packed monolayer of 7.5nm diameter Fe₃O₄ particles with 1.8nm interparticle spacing

GISAXS intensities and close comparison between actual and simulated GISAXS intensity plots.

Figure 4.41 demonstrate the geometry of just the Ag particles, where we have composed the particle coordinates according to the AB₂ lattice geometry with 1.8nm interparticle spacing and we subsequently removed the larger Fe₃O₄ particles. Figure 4.42 demonstrates that we can also simulated GISAXS intensities from such theoretical particle coordinate sets.

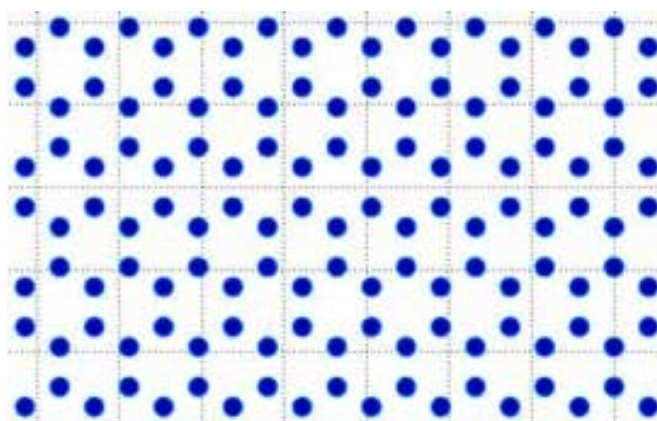


Figure 4.41) MATLAB 'bubble plot' of the 3D geometry of the 5.3nm diameter Ag particles from an AB₂ lattice with complementary (but removed) 7.5nm Fe₃O₄ particles and 1.8nm interparticle spacing.

Note the distinct lack of intensity gradation in the peaks (in figure 4.42) characteristic of smaller particle size relative to interparticle spacing.

When it comes to characterizing the full AB2 structure with both Fe_3O_4 particles and Ag particles, we have three choices for how to set up our virtual GISAXS simulation. We can let the layer of Ag particles layer rest above the Fe_3O_4 particle layer, below the Fe_3O_4 particle layer, or create layers of Ag particles both above *and* below the Fe_3O_4 particle layer. Each yields slightly differing GISAXS plots, and the intensity variations can be

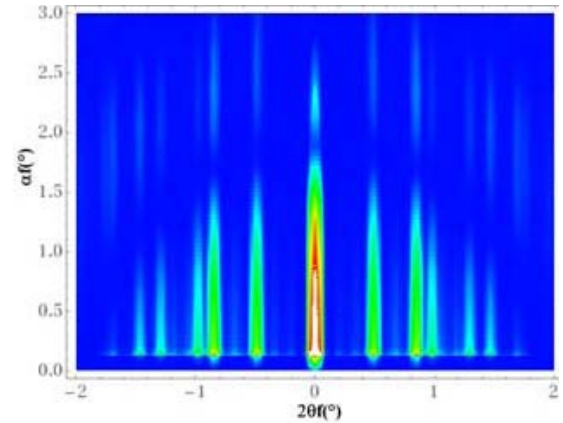


Figure 4.42) (left) Simulated GISAXS of 5.3nm diameter Ag particles from an AB2 lattice with complementary (but removed) 7.5nm Fe_3O_4 particles and 1.8nm interparticle spacing.

used to postulate on the actual physical structure, which may be hard to characterize via TEM in this case because of the potentially multi-layer nature of the structure. Precise matching of structure is achieved via linear analysis of simulated versus experimental GISAXS intensities, as described above. For brevity we show only the MATLAB visualizations of the structures, Figures 4.35 (repeated), 4.43, and 4.44, and the best-match simulated GISAXS and experimental GISAXS in this case, Figures 4.45 and 4.46, which represent the “ternary” case with layers of Ag particles above *and* below the Fe_3O_4 particle layer.

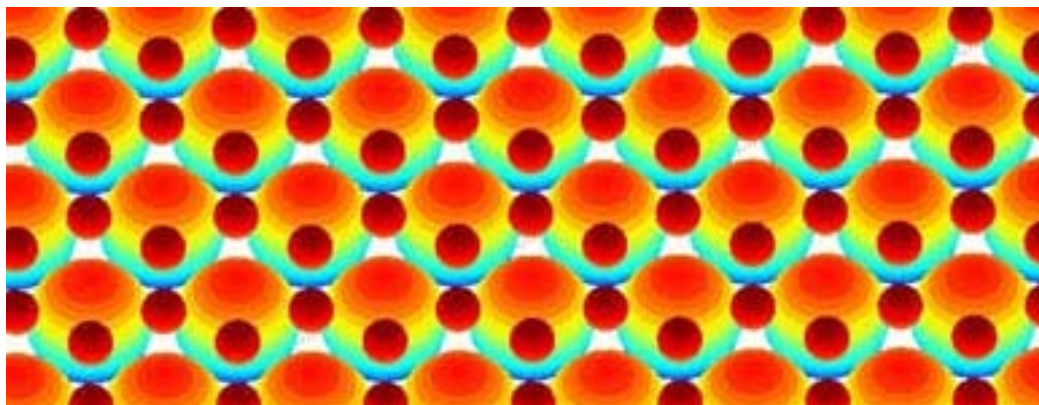


Figure 4.35) MATLAB 'bubble plot' of the 3D geometry of an AB2 lattice, with Ag particle layer ABOVE the Fe3O4 particle layer (repeated for graphical comparison)

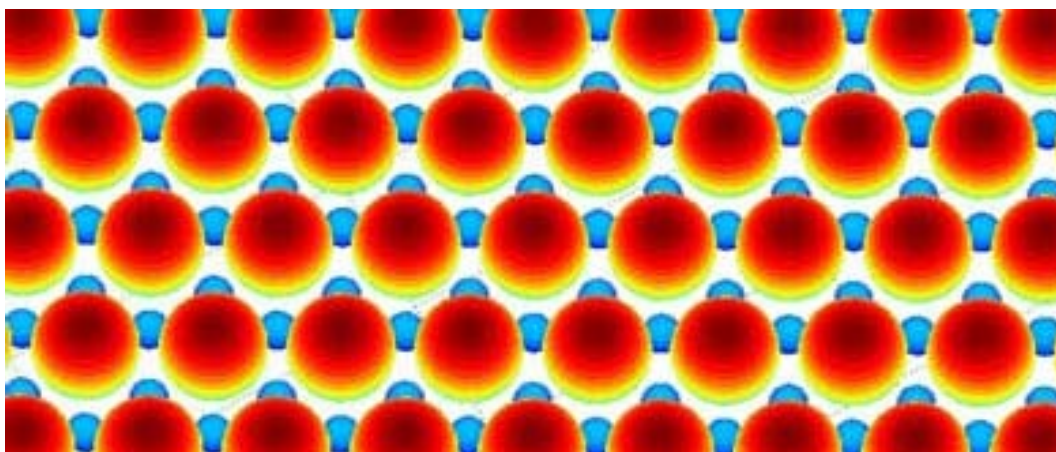


Figure 4.43) MATLAB 'bubble plot' of the 3D geometry of an AB2 lattice, with Ag particle layer BELOW the Fe3O4 particle layer

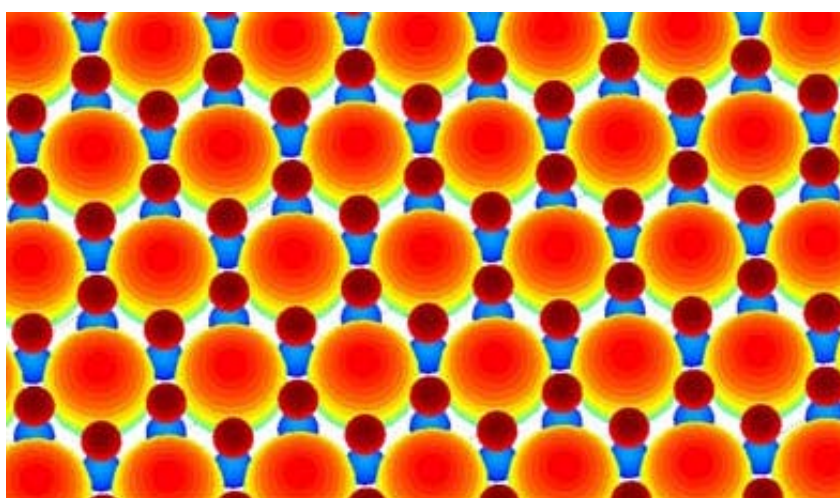


Figure 4.44) MATLAB 'bubble plot' of the 3D geometry of an AB2 lattice, with Ag particle layers ABOVE and BELOW the Fe3O4 particle layer

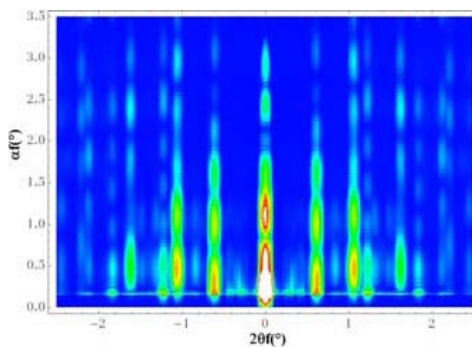


Figure 4.45) Simulated GISAXS of an AB2 lattice, with Ag particle layers ABOVE and BELOW the Fe₃O₄ particle layer

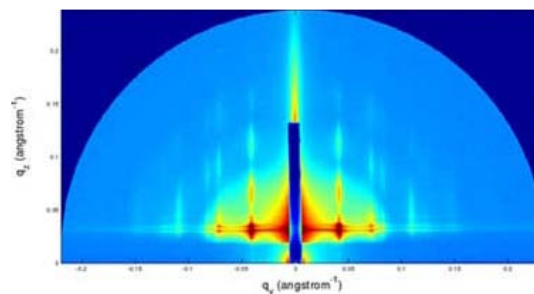


Figure 4.46) Experimental GISAXS from Dunphy and Xiong's EISA experiment with alkanethiolated 7.5nm Fe₃O₄ particles and 5.3nm Ag particles in toluene/PMMA solvent

The correspondence between simulated and experimental GISAXS of AB2 BNSL structures is not quite as close as for the simpler case of a monolayer of hexagonally packed particles, but still close enough that we can confirm that the AB2 lattice geometry, and we can say that there are most likely layers of Ag particles in the interstices above *and* below the Fe₃O₄ particle layer, and our approximation of 1.8nm interparticle spacing is not necessarily extremely precise but generally valid. Thus we have successfully verified the crystallographic order and geometry of several nanoparticle lattices and a general approximation by matching simulated GISAXS of theorized structures to experimental GISAXS of actual structures. This demonstrates the use (and usefulness) of the NANODIFT GISAXS simulator and FFT calculator (extension to Mathematic) and the method of linear analysis of GISAXS intensity plots for characterizing nanoparticle superlattices, and for research in direct-assembly via interface-driven order in soft-particle colloids in general.

Chapter V. Summary and Conclusion

V. i. Summary

New nanotechnologies may eventually replace many of the devices we currently use and even change our very lifestyles. Formative research showing how nanoscale principles can be used to our advantage in device design is the first step in advancing these technologies, and multiscale directed-assembly is an area with unlimited potential. In this work thus far, we have demonstrated that the application of classical crystallographic theory can help guide directed-assembly experiments by elucidating the underlying physical system dynamics involved. In crystal growth, an understanding of the surface energy shape of a material and the influence of substrate / beam direction can help crystal growers produce crystals of a desired shape at the nanoscale, and a great depth of new information can be extracted from TEM images using this new mastery of the theory. In colloid processing, an entirely new computational tool for simulating colloids was developed, and new devices and updates to experimental methods proposed. In both the crystal and colloid case, simulations successfully matched to experiment and advanced modeling tools were employed to analyze the results. This work shows that multiscale directed-assembly systems are not some future, far-off technology, but one that is already in place in laboratories and which can be systematically studied and modeled in the real world.

V. ii. Conclusion

Research tasks completed since Ryan Molecke's Comprehensive Exam include to 1) enabling simulated GISAXS on LAMMPS output coordinate files and performing simulated GISAXS analysis, 2) implementing clustering and randomness analysis on

LAMMPS output files, 3) completion of non-equilibrium “soft-colloid” LAMMPS simulations characterizing interfacial potentials, 4) the development of the method of surface extrapolation by reverse-plotting of energy trajectories (SERPENT) for plotting Wulff shapes and simulation of the evolution of solvated nanoparticle morphology, 5) submission of the Vincent “force-field” source code for inclusion into LAMMPS, 6) documentation of code tools, 7) peer-reviewed journal-article submission.

I believe that my research and dedication to the nanoscience program at UNM merits a successful completion of my dissertation defense and graduation with a Ph.D. in Nanoscience and Microsystems engineering, with a concentration in Bio-Nano Interfaces, at the University of New Mexico. I have completed all coursework required with a 3.7 GPA. I have completed three lab rotations and a research internship, while performing community outreach and tutoring in completion of the requirements for the Integrated Graduate Education and Research Traineeship fellowship sponsored by the National Institutes of Health and the National Cancer Research Institute. I have widely varied lab experience and have proven that I am a competent group and valuable productive group member in several teams. I have been published in a peer-reviewed research journal, and I am nearing submission on several more articles, all for first-author publication. My research tasks and optional coursework have been specifically geared towards my concentration in nano-bio interfaces, and the current work in soft-particle colloids clearly falls into this category.

Ryan Molecke

April 13th, 2011

BIBLIOGRAPHY

- 1 Hidalgo, P., Méndez, B. & Piqueras, J. High aspect ratio GeO₂ nano- and microwires with waveguiding behaviour. *Nanotechnology* **18**, 155203 (2007).
- 2 Borri, P., Schneider, S., Langbein, W. & Bimberg, D. Ultrafast carrier dynamics in InGaAs quantum dot materials and devices. *Journal of Optics A: Pure and Applied Optics* **8**, S33-S46 (2006).
- 3 Chen, A., Chua, S. J., Chen, P., Chen, X. Y. & Jian, L. K. Fabrication of sub-100 nm patterns in SiO₂ templates by electron-beam lithography for the growth of periodic III–V semiconductor nanostructures. *Nanotechnology* **17**, 3903-3908 (2006).
- 4 Scott, J. F. Applications of modern ferroelectrics. *Science* **315**, 954-959 (2007).
- 5 Liao, W. M., Li, P. W., Kuo, David M. T., Lia, W. T. Room-temperature transient carrier transport in germanium single-hole/electron transistors. *Applied Physics Letters* **88**, 182109 (2006).
- 6 Horsell, D. W. *et al.* Spontaneous current generation in gated nanostructures. *Europhysics Letters (EPL)* **71**, 658-664 (2005).
- 7 Galiana, B., Rey-Stolle, I., Baudrit, M., García, I. & Algora, C. A comparative study of BSF layers for GaAs-based single-junction or multijunction concentrator solar cells. *Semiconductor Science and Technology* **21**, 1387-1392 (2006).
- 8 Greenberg, M. R., Smolyakov, G. A., Boyle, T. J. & Osiski, M. Synthesis and characterization of ZnO and ZnO/ZnS colloidal nanocrystals. *Proc. SPIE* **6448**, 644806-644811 (2007).
- 9 Rapuano, R. Supported Bilayers On Silica. *Journal of Colloid and Interface Science* **226**, 299-307 (2000).
- 10 Sharma, M. K. & Gilchrist, M. L. Templated Assembly of Biomembranes on Silica Microspheres Using Bacteriorhodopsin Conjugates as Structural Anchors. *Langmuir* **23**, 7101-7112 (2007).
- 11 Buranda, T. *et al.* Biomimetic Molecular Assemblies on Glass and Mesoporous Silica Microbeads for Biotechnology. *Langmuir* **19**, 1654-1663 (2003).

- 12 Granéli, A., Rydström, J., Kasemo, B. & Höök, F. Formation of Supported Lipid Bilayer Membranes on SiO₂ from Proteoliposomes Containing Transmembrane Proteins. *Langmuir* **19**, 842-850 (2003).
- 13 Xu, Y. & Szoka, F. C. Mechanism of DNA Release from Cationic Liposome/DNA Complexes Used in Cell Transfection^{†,‡}. *Biochemistry* **35**, 5616-5623 (1996).
- 14 Atif, S. M., Hasan, I., Ahmad, N., Khan, U. & Owais, M. Fusogenic potential of sperm membrane lipids: Nature's wisdom to accomplish targeted gene delivery. *FEBS Letters* **580**, 2183-2190 (2006).
- 15 Liu, J., Stace-Naughton, A., Jiang, X. & Brinker, C. J. Porous Nanoparticle Supported Lipid Bilayers (Protocells) as Delivery Vehicles. *Journal of the American Chemical Society* **131**, 1354-1355 (2009).
- 16 Brinker, C. J. & Scherer, G. W. *Sol-gel science : the physics and chemistry of sol-gel processing*. (Academic Press, 1990).
- 17 Walcarius, A. & Collinson, M. M. Analytical Chemistry with Silica Sol-Gels: Traditional Routes to New Materials for Chemical Analysis. *Annual Review of Analytical Chemistry* **2**, 121-143 (2009).
- 18 Pang, J. *et al.* Free-Standing, Patternable Nanoparticle/Polymer Monolayer Arrays Formed by Evaporation Induced Self-Assembly at a Fluid Interface. *Journal of the American Chemical Society* **130**, 3284-3285 (2008).
- 19 Baca, H. K. *et al.* Cell-directed assembly of lipid-silica nanostructures providing extended cell viability. *Science* **313**, 337-341 (2006).
- 20 Israelachvili, J. N. *Intermolecular and surface forces* / Jacob N. Israelachvili. (Academic Press, 1991).
- 21 Moore, G. E. Cramming more components onto integrated circuits. *Proceedings of the IEEE* **86**, 82-85 (1998).
- 22 Wu, Y. & Yang, P. Direct Observation of ~~Maped~~-Solid Nanowire Growth. *Journal of the American Chemical Society* **123**, 3165-3166 (2001).
- 23 Dobrushin, R., Koteck'y, R. & Shlosman, S. Wulff construction. A global shape from local interaction. Translated from the Russian by the authors. Translations of Mathematical Monographs, 104. *American Mathematical Society, Providence, RI*, 0-8218 (1992).

- 24 Nielsen, J. R. (Amsterdam: North-Holland, 1976).
- 25 Parr, R. G. & Yang, W. *Density-functional theory of atoms and molecules*. (Oxford University Press, USA, 1994).
- 26 Wong, P. S., Liang, B., Molecke, R., Tatebayashi, J. & Huffaker, D. L. Controlled Formation and Dynamic Wulff Simulation of Equilibrium Crystal Shapes of GaAs Pyramidal Structures on Nanopatterned Substrates. *Crystal Growth & Design* **10**, 2509-2514 (2010).
- 27 Derjaguin, B. & Landau, L. A theory of the stability of strongly charged lyophobic sols and the coalescence of strongly charged particles in electrolytic solution. *Acta Phys.-Chim. USSR* **14**, 633-662 (1941).
- 28 Verwey, E. & Overbeek, J. Th. G.(1948) Theory of the stability of lyophobic colloids. *Elsevier Publ. Co. Inc., London* **8**, 9.
- 29 Bybee, M. Hydrodynamic Simulations of Colloidal Suspensions with Short-Range Attraction and Long-Range Repulsion.
- 30 Peng, D., Osher, S., Merriman, B. & Zhao, H. K. 251 (Amer Mathematical Society).
- 31 Umeda, T., Kumakura, K., Motohisa, J. & Fukui, T. InAs quantum dot formation on GaAs pyramids by selective area MOVPE. *Physica E: Low-dimensional Systems and Nanostructures* **2**, 714-719 (1998).
- 32 Hahn, C. K., Motohisa, J. & Fukui, T. Formation of single and double self-organized InAs quantum dot by selective area metal-organic vapor phase epitaxy. *Applied Physics Letters* **76**, 3947 (2000).
- 33 Wong, P., Balakrishnan, G., Nuntawong, N., Tatebayashi, J. & Huffaker, D. Controlled InAs quantum dot nucleation on faceted nanopatterned pyramids. *Applied Physics Letters* **90**, 183103 (2007).
- 34 Wong, P. *et al.* Fabrication and characteristics of broad-area light-emitting diode based on nanopatterned quantum dots. *Nanotechnology* **20**, 035302 (2009).
- 35 Chithrani, D., Williams, R., Lefebvre, J., Poole, P. & Aers, G. Optical spectroscopy of single, site-selected, InAs/InP self-assembled quantum dots. *Applied Physics Letters* **84**, 978 (2004).

- 36 Hsieh, T. P. *et al.* Single photon emission from an InGaAs quantum dot precisely positioned on a nanoplane. *Applied Physics Letters* **90**, 073105 (2007).
- 37 Lee, J. *et al.* Selective growth of InGaAs/GaAs quantum dot chains on pre-patterned GaAs (100). *Nanotechnology* **17**, 2275 (2006).
- 38 Moll, N., Kley, A., Pehlke, E. & Scheffler, M. GaAs equilibrium crystal shape from first principles. *Physical Review B* **54**, 8844 (1996).
- 39 Lee, S. & Brueck, S. Equilibrium crystal shape of GaAs in nanoscale patterned growth. *Journal of applied physics* **96**, 1214 (2004).
- 40 Gadewar, S. B., Hofmann, H. M. & Doherty, M. F. Evolution of crystal shape. *Crystal Growth & Design* **4**, 109-112 (2004).
- 41 Zangwill, A. *Physics at surfaces*. (Cambridge Univ Pr, 1988).
- 42 Omar, M. A. *Elementary solid state physics: principles and applications*. (Addison-Wesley, 1993).
- 43 Guide, M. U. The MathWorks. *Inc., Natick, MA* **5** (1998).
- 44 Schmidt, W. (4× 2) and (2× 4) reconstructions of GaAs and InP (001) surfaces. *Applied Physics A: Materials Science & Processing* **65**, 581-586 (1997).
- 45 Lee, S. H., Moritz, W. & Scheffler, M. GaAs (001) surface under conditions of low As pressure: Evidence for a novel surface geometry. *Physical Review Letters* **85**, 3890-3893 (2000).
- 46 Ashkin, A., Dziedzic, J., Bjorkholm, J. & Chu, S. Observation of a single-beam gradient force optical trap for dielectric particles. *Optical angular momentum*, 196 (2003).
- 47 Vale, R. D. *et al.* Direct observation of single kinesin molecules moving along microtubules. *Nature* **380**, 451 (1996).
- 48 Koch, S. J., Shundrovsky, A., Jantzen, B. C. & Wang, M. D. Probing protein-DNA interactions by unzipping a single DNA double helix. *Biophysical journal* **83**, 1098-1105 (2002).
- 49 Dzyaloshinskii, I., Lifshitz, E. & Pitaevskii, L. P. GENERAL THEORY OF VAN DER WAALS'FORCES. *Physics-Uspekhi* **4**, 153-176 (1961).

- 50 Good, N. E. *et al.* Hydrogen Ion Buffers for Biological Research*. *Biochemistry* **5**, 467-477 (1966).
- 51 Burrows, S., Patterson Kane, J., Becker, D. & Fleck, R. Fluorescence Recovery After Photobleaching. *Imaging & Microscopy* **8**, 62-64 (2006).
- 52 Osinski, M., Jovin, T. M. & Yamamoto, K. Biomedical applications of colloidal nanocrystals. *Journal of Biomedicine and Biotechnology* **2007** (2007).
- 53 Osinski, M., Jovin, T. M. & Yamamoto, K. (Society of Photo-Optical Instrumentation Engineers (SPIE)).
- 54 Ito, A., Shinkai, M., Honda, H. & Kobayashi, T. Medical application of functionalized magnetic nanoparticles. *Journal of bioscience and bioengineering* **100**, 1-11 (2005).
- 55 Zhang, L. *et al.* Nanoparticles in medicine: therapeutic applications and developments. *Clinical Pharmacology & Therapeutics* **83**, 761-769 (2007).
- 56 Michalet, X. *et al.* Quantum dots for live cells, in vivo imaging, and diagnostics. *Science* **307**, 538 (2005).
- 57 Luo, X., Morrin, A., Killard, A. J. & Smyth, M. R. Application of nanoparticles in electrochemical sensors and biosensors. *Electroanalysis* **18**, 319-326 (2006).
- 58 Medintz, I. L. *et al.* Self-assembled nanoscale biosensors based on quantum dot FRET donors. *Nature materials* **2**, 630-638 (2003).
- 59 Medintz, I. L., Uyeda, H. T., Goldman, E. R. & Mattoussi, H. Quantum dot bioconjugates for imaging, labelling and sensing. *Nature materials* **4**, 435-446 (2005).
- 60 Westcott, S. L., Oldenburg, S. J., Lee, T. R. & Halas, N. J. Formation and adsorption of clusters of gold nanoparticles onto functionalized silica nanoparticle surfaces. *Langmuir* **14**, 5396-5401 (1998).
- 61 Krenn, J. *et al.* Surface plasmon micro and nano optics. *Journal of microscopy* **209**, 167-172 (2003).
- 62 Ozbay, E. Plasmonics: merging photonics and electronics at nanoscale dimensions. *Science* **311**, 189 (2006).

- 63 Ko, S. H. *et al.* Direct nanoimprinting of metal nanoparticles for nanoscale electronics fabrication. *Nano letters* **7**, 1869-1877 (2007).
- 64 Avnir, D., Coradin, T., Lev, O. & Livage, J. Recent bio-applications of sol-gel materials. *Journal of Materials Chemistry* **16**, 1013-1030 (2006).
- 65 Nayak, S. & Lyon, L. A. Soft nanotechnology with soft nanoparticles. *Angewandte chemie international edition* **44**, 7686-7708 (2005).
- 66 Binder, W. H. & Sachsenhofer, R. 'Click'Chemistry in Polymer and Materials Science. *Macromolecular rapid communications* **28**, 15-54 (2007).
- 67 Sun, Y. & Xia, Y. Shape-controlled synthesis of gold and silver nanoparticles. *Science* **298**, 2176 (2002).
- 68 Couto, D. S., Alves, N. M. & Mano, J. F. Nanostructured multilayer coatings combining chitosan with bioactive glass nanoparticles. *Journal of Nanoscience and Nanotechnology* **9**, 1741-1748 (2009).
- 69 Chen, W., Zhang, J. Z. & Joly, A. G. Optical properties and potential applications of doped semiconductor nanoparticles. *Journal of Nanoscience and Nanotechnology* **4**, 919-947 (2004).
- 70 Reddy, G. R. *et al.* Vascular targeted nanoparticles for imaging and treatment of brain tumors. *Clinical Cancer Research* **12**, 6677 (2006).
- 71 Singh, S. *et al.* Intravenous transferrin, RGD peptide and dual-targeted nanoparticles enhance anti-VEGF intrareceptor gene delivery to laser-induced CNV. *Gene therapy* **16**, 645-659 (2009).
- 72 Niidome, T. *et al.* Poly (ethylene glycol)-modified gold nanorods as a photothermal nanodevice for hyperthermia. *Journal of Biomaterials Science, Polymer Edition* **20**, 1203-1215 (2009).
- 73 Morpurgo, M., Kirschner, M. & Radu, A. An approach to increased polyplex gene delivery by peptides selected from a phage display library. *Journal of biochemical and biophysical methods* **52**, 31-43 (2002).
- 74 Destito, G., Schneemann, A. & Manchester, M. Biomedical nanotechnology using virus-based nanoparticles. *Viruses and Nanotechnology*, 95-122 (2009).
- 75 Shevchenko, E. V., Talapin, D. V., Kotov, N. A., O'Brien, S. & Murray, C. B. Structural diversity in binary nanoparticle superlattices. *Nature* **439**, 55-59 (2006).

- 76 Schmitt, J. *et al.* Metal nanoparticle/polymer superlattice films: Fabrication and control of layer structure. *Advanced Materials* **9**, 61-65 (1997).
- 77 Coffey, J. L. *et al.* Dictation of the shape of mesoscale semiconductor nanoparticle assemblies by plasmid DNA. *Applied Physics Letters* **69**, 3851 (1996).
- 78 Ripley, B. D. The second-order analysis of stationary point processes. *Journal of Applied Probability* **13**, 255-266 (1976).
- 79 Dixon, P. M. Ripley's K function. (2002).
- 80 Hopkins, B. & Skellam, J. A new method for determining the type of distribution of plant individuals. *Annals of Botany* **18**, 213 (1954).
- 81 Byth, K. & Ripley, B. On sampling spatial patterns by distance methods. *Biometrics* **36**, 279-284 (1980).
- 82 Hoover, W. G. Nonequilibrium molecular dynamics. *Nuclear Physics A* **545**, 523-536 (1992).
- 83 Plimpton, S. Fast parallel algorithms for short-range molecular dynamics. *Journal of Computational Physics* **117**, 1-19 (1995).
- 84 Hairer, E., Lubich, C. & Wanner, G. Geometric numerical integration illustrated by the Störmer–Verlet method. *Acta Numerica* **12**, 399-450 (2003).
- 85 Jones, J. On the determination of molecular fields. I. From the variation of the viscosity of a gas with temperature. *Proceedings of the Royal Society of London. Series A, Containing Papers of a Mathematical and Physical Character* **106**, 441-462 (1924).
- 86 Heisenberg, W. Mehrkörperproblem und Resonanz in der Quantenmechanik. *Zeitschrift für Physik A Hadrons and Nuclei* **38**, 411-426 (1926).
- 87 Dirac, P. A. M. On the theory of quantum mechanics. *Proceedings of the Royal Society of London. Series A* **112**, 661 (1926).
- 88 London, F. *Z Phys Chem B* 1930, 11, 222; Eisenschitz, R.; London, F. *Z Phys* **60**, 491 (1930).
- 89 Luijten, E., Goldbart, P. M., Lewis, J. A. & Schweizer, K. S. Structural properties and phase behavior in colloidal suspensions. (2010).

- 90 Hamaker, H. The London--van der Waals attraction between spherical particles. *physica* **4**, 1058-1072 (1937).
- 91 Vincent, B., Edwards, J., Emmett, S. & Jones, A. Depletion flocculation in dispersions of sterically-stabilised particles. *Colloids and Surfaces* **18**, 261-281 (1986).
- 92 Everaers, R. & Ejtehadi, M. Interaction potentials for soft and hard ellipsoids. *Physical Review E* **67**, 041710 (2003).
- 93 Flory, P. J. *Principles of polymer chemistry*. (Cornell Univ Pr, 1953).
- 94 Huggins, M. L. Solutions of long chain compounds. *Journal of Chemical Physics* **9**, 440 (1941).
- 95 Brigham, E. O. *The fast Fourier transform and its applications*. (1988).
- 96 Rasband, W. & ImageJ, U. National Institutes of Health. *Bethesda, Maryland, USA* **2007** (1997).
- 97 Tate, M. P. & Hillhouse, H. W. General method for simulation of 2D GISAXS intensities for any nanostructured film using discrete Fourier transforms. *The Journal of Physical Chemistry C* **111**, 7645-7654 (2007).
- 98 Weisstein, E. W. *CRC concise encyclopedia of mathematics*. (CRC Pr I Llc, 2003).
- 99 Harris, F. J. Spectral analysis windowing.
- 100 Ewald, P. Introduction to the dynamical theory of X-ray diffraction. *Acta Crystallographica Section A: Crystal Physics, Diffraction, Theoretical and General Crystallography* **25**, 103-108 (1969).
- 101 Humphrey, W., Dalke, A. & Schulten, K. VMD: visual molecular dynamics. *Journal of molecular graphics* **14**, 33-38 (1996).
- 102 Bragg, W. L. 43–57.
- 103 Ashcroft, N. W. & Mermin, N. D. *Solid State Physics* (Holt, Rinehart and Winston, New York, 1976).

- 104 Widom, B. *Statistical mechanics: a concise introduction for chemists*. (Cambridge Univ Pr, 2002).
- 105 Patankar, S. V. *Numerical heat transfer and fluid flow*. (Hemisphere Pub, 1980).
- 106 Mathematica, V. 6, Wolfram Research. Inc., Champaign, IL, USA (2007).
- 107 Vosko, S. H., Wilk, L. & Nusair, M. Accurate spin-dependent electron liquid correlation energies for local spin density calculations: a critical analysis. *Canadian Journal of Physics* **58**, 1200-1211 (1980).
- 108 Brust, M., Walker, M., Bethell, D., Schiffrin, D. J. & Whyman, R. Synthesis of thiol-derivatised gold nanoparticles in a two-phase liquid-liquid system. *J. Chem. Soc., Chem. Commun.*, 801-802 (1994).
- 109 Murray, C., Norris, D. & Bawendi, M. G. Synthesis and characterization of nearly monodisperse CdE (E= sulfur, selenium, tellurium) semiconductor nanocrystallites. *Journal of the American Chemical Society* **115**, 8706-8715 (1993).
- 110 Talapin, D. V., Rogach, A. L., Kornowski, A., Haase, M. & Weller, H. Highly luminescent monodisperse CdSe and CdSe/ZnS nanocrystals synthesized in a hexadecylamine-trioctylphosphine oxide-trioctylphosphine mixture. *Nano letters* **1**, 207-211 (2001).
- 111 Sun, S. *et al.* Controlled synthesis and assembly of FePt nanoparticles. *The Journal of Physical Chemistry B* **107**, 5419-5425 (2003).
- 112 Kovalenko, M. V., Scheele, M. & Talapin, D. V. Colloidal nanocrystals with molecular metal chalcogenide surface ligands. *Science* **324**, 1417 (2009).
- 113 Ryan, K. M., Mastroianni, A., Stancil, K. A., Liu, H. & Alivisatos, A. Electric-field-assisted assembly of perpendicularly oriented nanorod superlattices. *Nano letters* **6**, 1479-1482 (2006).
- 114 Huang, Y., Duan, X., Wei, Q. & Lieber, C. M. Directed assembly of one-dimensional nanostructures into functional networks. *Science* **291**, 630 (2001).
- 115 Cho, K. S., Talapin, D. V., Gaschler, W. & Murray, C. B. Designing PbSe nanowires and nanorings through oriented attachment of nanoparticles. *Journal of the American Chemical Society* **127**, 7140-7147 (2005).

- 116 McDonald, S. A. *et al.* Solution-processed PbS quantum dot infrared photodetectors and photovoltaics. *Nature materials* **4**, 138-142 (2005).
- 117 Acharya, S. & Efrima, S. Two-dimensional pressure-driven nanorod-to-nanowire reactions in Langmuir monolayers at room temperature. *Journal of the American Chemical Society* **127**, 3486-3490 (2005).
- 118 Wu, H. *et al.* Pressure Driven Assembly of Spherical Nanoparticles and Formation of 1D Nanostructure Arrays. *Angewandte chemie international edition* **49**, 8431-8434 (2010).
- 119 Chen, Y., Palmer, R. E. & Wilcoxon, J. P. Sintering of passivated gold nanoparticles under the electron beam. *Langmuir* **22**, 2851-2855 (2006).
- 120 Xiong, S. *et al.* Integration of a close-packed quantum dot monolayer with a photonic-crystal cavity via interfacial self-assembly and transfer. *Small* **6**, 2126-2129 (2010).
- 121 Finch, D. & Vesely, D. The evaluation of polymers for electron resists by mass loss measurements. *Polymer* **28**, 675-679 (1987).
- 122 Lane, J. M. D. & Grest, G. S. Spontaneous Asymmetry of Coated Spherical Nanoparticles in Solution and at Liquid-Vapor Interfaces. *Physical Review Letters* **104**, 235501 (2010).
- 123 Huang, D., Liao, F., Molesa, S., Redinger, D. & Subramanian, V. Plastic-compatible low resistance printable gold nanoparticle conductors for flexible electronics. *Journal of the electrochemical society* **150**, G412 (2003).
- 124 Wu, Y., Li, Y., Liu, P., Gardner, S. & Ong, B. S. Studies of gold nanoparticles as precursors to printed conductive features for thin-film transistors. *Chemistry of materials* **18**, 4627-4632 (2006).
- 125 Song, J. H., Wu, Y., Messer, B., Kind, H. & Yang, P. Metal Nanowire Formation Using Mo₃Se₃-as Reducing and Sacrificing Templates. *Journal of the American Chemical Society* **123**, 10397-10398 (2001).
- 126 Fan, H. *et al.* Self-assembly of ordered, robust, three-dimensional gold nanocrystal/silica arrays. *Science* **304**, 567 (2004).
- 127 Efros, A. & Shklovskii, B. Coulomb gap and low temperature conductivity of disordered systems. *Journal of Physics C: Solid State Physics* **8**, L49 (1975).

VII. Appendices

VII	Appendices	137 - 176
(A)	Cellspan: A Graphical User Interface to Protein-Pathway Mapping via Statistical Tests for Spatial Randomness	138 - 154
	Appendix (B) Table of Contents	155
(B)	LAMMPS software source code	
(C)	MATLAB software source code	
(D)	Mathematica software source code	
(E)	C++ tools software source code	
(F)	TCL/TK/R/Expect software source code	

* See Chapter IV for bibliography references for Appendix (A)

** contact Ryan Molecke at Reason@unm.edu or Ryan@Molecke.com for software versions of the source code and/or accompanying data files, or questions/comments on the operation of any included software

Appendix A

Cellspan: A Graphical User Interface to Protein-Pathway Mapping via Statistical Tests for Spatial Randomness

Colloidal suspensions of particles are chemical mixtures of solvent and particles which occur in nature and can be created artificially by mixing custom solvents and particles. Thin-film and colloid processing is an established industry in which soft-colloids, i.e. those containing nanoparticles with grafted polymer coatings (and often free polymer in the solvent), are studied as precursor solutions to which controlled non-equilibrium dynamics can be applied as a method for the directed-assembly of multiscale devices, via processing methods such as evaporation-induced self-assembly (EISA), self-supporting thin-film transfer, and electron beam irradiation. Such processes can produce thin-films with nanoparticle distributions featuring long-range order and, theoretically, scalable device technologies with arbitrary complexity and interconnectedness and composed of a multiple particle types each having custom electronic, magnetic, optical, stimuli-responsive, and/or bio-active properties.

Nanoparticle colloids and thin-films can be characterized by classical spatial statistics tests such as the Ripley's' K univariate test for clustering versus randomness, Ripley's K bivariate test for co-clustering, and the Hopkins test for clustering versus spatial randomness. These three tests were integrated into a graphical user interface (GUI) written in the TCL, Tk, EXPECT programming languages (by Ryan Molecke), which controls (feeds parsed commands to) the R statistics engine as a sub-process in order, under a software project titled "CellSpan" sponsored by the UNM Center for the Spatio-Temporal Modeling of Cell-Signaling Networks. Cellspan is used to characterize

clustering and co-clustering among nanoparticle-bound proteins (in lysed human cancer cells) to investigate diagnostic and therapeutic avenues based on catalogs of protein interactions and chain reactions, or “protein pathways”. Protein pathways are chain-reactions among proteins which occur in cells which regulate the cell life-cycle and responses to the local environment, often including kinases which pass into and out of the nuclear envelope of the cell and regulate activation and deactivation of specific segments of DNA. In cancer cells, these pathways are often over / under-expressed, resulting in typical cancer symptoms including local physiological tissue response (such as angiogenesis), non-standard cell life-cycle activity (including immortality), non-standard cell respiration (respiration by glycolysis), and cell death. By characterizing these pathways, we hope to help discovery and testing of new drugs which act to regulate these protein-pathways or the corresponding kinase-DNA/RNA activity. We describe the Ripley’s K and Hopkins’ tests and provide a mathematical introduction, along with “screen-capture” images of the output from the Cellspan software which show the protein positions, the boundary of the cell wall, and the corresponding graphs generated by the applied spatial statistics algorithms.

See Appendix F for a printed copy of the Cellspan source code. Visit <http://stmc.health.unm.edu/> for a copy of the Cellspan source code, executable file for either Microsoft Windows or Debian Linux operating systems, and additional project background and information on the development of the Cellspan software.

The Ripley’s K Univariate test is also known as the reduced second moment function of a stationary point process. The function $K(t)$ is calculated from the data and compared to what we would expect $K(t)$ to be if the data has complete spatial

randomness (CSR). If the data is a completely random Poisson point process the true value for $K(t)$ would then be $K(t) = \rho t^2$, where ρ is the intensity of a homogenous Poisson point process. The calculated value of $K(t)$ is then plotted against the theoretical $K(t)$ for comparison.

Ripley's bivariate test looks at the distances between two sets of particles to determine if the data is co-clustered. A plot of this test is enclosed in between two lines known as tolerance envelopes. If the data line stays inside the envelopes then the two particles are not considered to be co-clustered, if the data line is above the envelopes then the data is considered to be co-clustered.

The Hopkins' test is a ratio of point-to-event distances over event-to-event distances. Random points are selected from the data area and compared to the actual data points. Our version repeats this test 1000 times and then plots the results. If the plot is shaped like a normal "Bell" curve then the test is considered to show CSR. If the plot is skewed then the data is considered clustered.

We include a brief mathematical summary of the Ripley's K functions. The K function is:

$$K(t) = \lambda^{-1} E[n] \quad (7.1)$$

where E is the expectation value of n , the number of "extra" events within distance t of a randomly chosen coordinate in the system (over $\lambda_0 = \rho t^2$, the intensity of a homogenous point process), and λ is the density (number per unit area) of events in a given particle process. The multivariate form of the Ripley's function is then:

$$K_{ij}(t) = \lambda_j^{-1} E[n] \quad (7.2)$$

for particle types $i \neq j$. Processes where the events (i.e. pairs of particles with a certain distance of separation) cannot occur within some minimum distance of each other can be described by “Matern hard-core processes”. In the Matern algorithm, events with spatial separation less than critical distance δ are deleted, and the remaining events are the realization of the “hard-core” process, representing a system of particles which cannot overlap. The K function for this process (implemented in Cellspan) is:

$$K(t) = \frac{2\rho\pi}{\exp(-\rho\pi\delta^2)} \int_0^t uk(u)du \quad (7.3)$$

where $k(u)$ describes the probability of retaining a pair of events separated by a distance u :

$$k(u) = \begin{cases} 0, & h < \delta \\ \exp[-\rho V(h, \delta)], & h \geq \delta \end{cases} \quad (7.4)$$

with $V(h, \delta)$ the area of intersection of two circles of radius δ , with centers separated by distance h . Ripley also described several forms for calculating the K-function of “soft-core” particles, those with particles that may overlap, however since this was not applicable to the case of nanoparticle-bound proteins it was not included in Cellspan. Edge-effects on the statistical test, which arise from finite bounding geometries and can significantly affect test results, are accommodated for in Cellspan using the method described by Ripley for hard-core process (not included here).

The UNM Center for Spatio-Temporal Modeling of Cell-Signaling Networks, acting under the auspices of the UNM Cancer Research Facility, contracted Ryan Molecke to develop Cellspan, a “cellular statistics calculator”, in 2005/2006. We

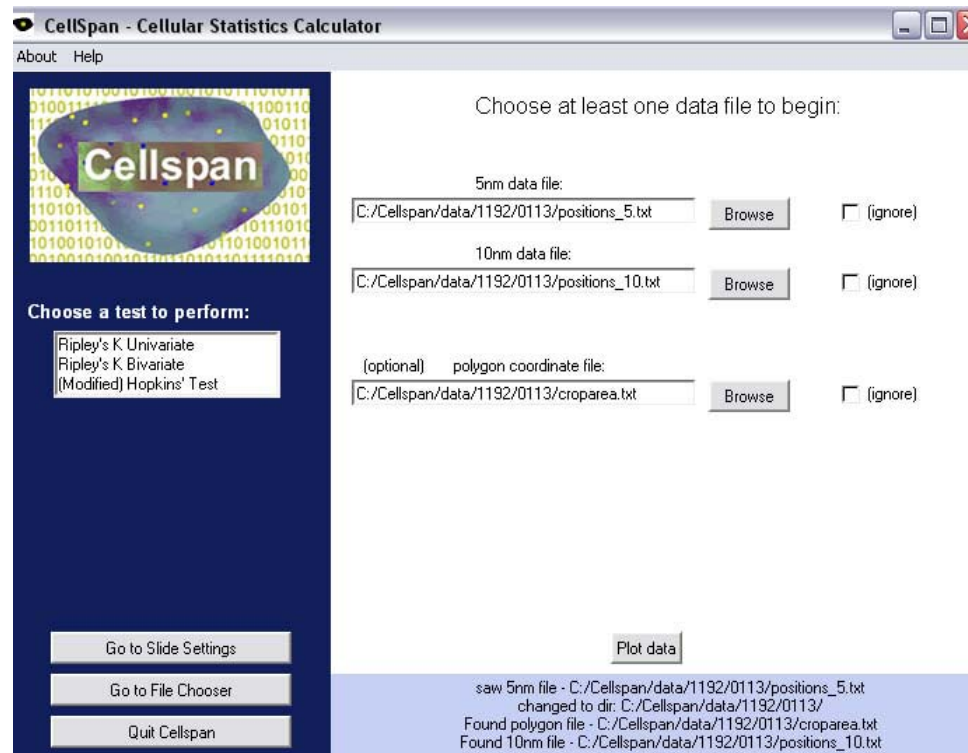


Figure 7.1) Screenshot of the DATA FILE CHOOSER SCREEN within Cellspan, after a set of data files have been selected for processing

illustrate the interface to this software and the plots of particle position and graphs of spatial statistics functions that Cellspan produces.

Figure 7.1 illustrates the first screen that is displayed when the Cellspan program is executed, which allows users to select data files for processing. This screen also allows the user to plot the coordinates of the particles against data files which hold polygon edge data which represents the edge of the cells, for visual inspection and verification of the data before it is processed. Once a single data file is chosen, Cellspan attempts to find accompanying particle position and polygon data files for user convenience. A feedback

area (text over light blue section) is included in each screen to allow the user to see each sub-process Cellspan is performing, alert the user to the success or failure of those sub-processes, or instruct the user to wait during processing periods which are expected to take a noticeable amount of time.

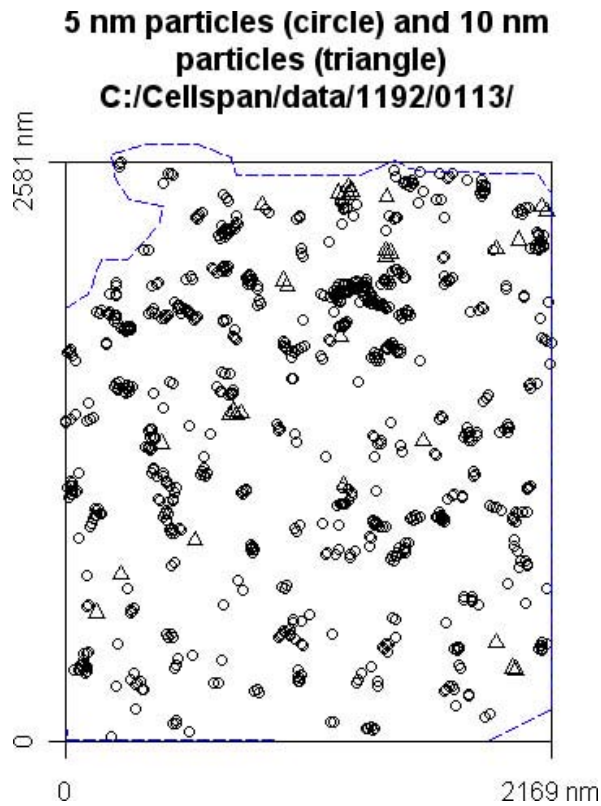


Figure 7.2) Schematic plot of the particle positions from a processed image of a lysed human cancer cell, showing the positions of the 5 nm particles (circles), the 10 nm particles (triangles), and the bounding polygon representing the cell edge (blue line).

Figure 7.2 the plot generated by Cellspan by pressing the “plot” button (from Figure 7.1) once data input files have been selected, which Cellspan generates by sending parsed commands to the R engine as a sub-process. It is a schematic representation of an image, taken on an ultra-high-resolution microscope, of a freshly-lysed human cancer cell containing 5 nm gold nanoparticles (AuNPs) bound to one protein, and 10 nm AuNPs bound to another protein of interest in protein-pathway mapping, a field within spatiotemporal modeling of cell signaling networks. This plotting capability was incorporated into Cellspan in order to allow the user to quickly inspect/verify data files before the spatial statistics tests are run. The axes of such plots (as Figure 7.2), which indicate the dimensions of the system, can be used to tune the magnification factor, image

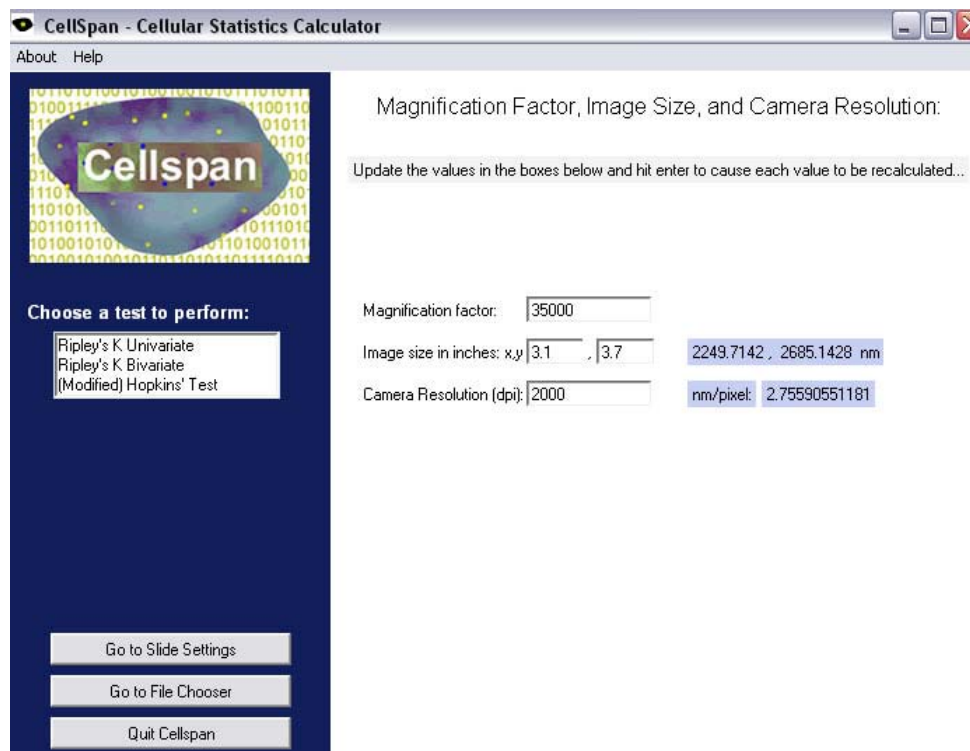


Figure 7.3) SLIDE SETTINGS panel within Cellspan, which allows the user to tune the effective magnification factor, image size, and camera resolution variables used to calculate the actual physic dimensions of the system from the image (i.e. calculate meters/pixel and system dimension in meters)

size, and camera resolution settings within Cellspan.

Figure 7.3 shows the “slide settings” panel within Cellspan, which allows the user to set magnification factor, image size, and camera resolution variables used to calculate the actual physical dimensions of the system, in meters, corresponding to the raw image and (data file coordinates) which are represented by an arbitrary unitless number of pixels. This allows the user to graph the spatial statistics test results with accurate axis dimensions, and to set graph ranges and spatial resolution for those graphs. Once the user has selected data files, verified the slide settings, and (optionally) plotted the data, they will choose one of the statistical tests to perform by clicking on the name of the test (center left of the Cellspan GUI). Three spatial statistics tests are available: the Ripley’s K univariate, the Ripley’s K bivariate, and the Hopkins’ test. These tests are implemented by sending parsed commands to the R engine as a sub-process, resulting in graphical output of the statistical test results to the screen (which can then be saved in common file formats). Cellspan parses the code for the spatial statistical tests, written in R language code (by Diana Roberts), and includes the locations of the data files to send to the R engine sub-process. This parsing process was refined over several years for operating-system independence and to increase stability (eliminate bugs). Ryan Molecke completed five versions of Cellspan over a period of six years, with sixteen total “revisions”, up to the date of this publication, and revisions under version 5 (one for each operating system) are very stable and fully tested.

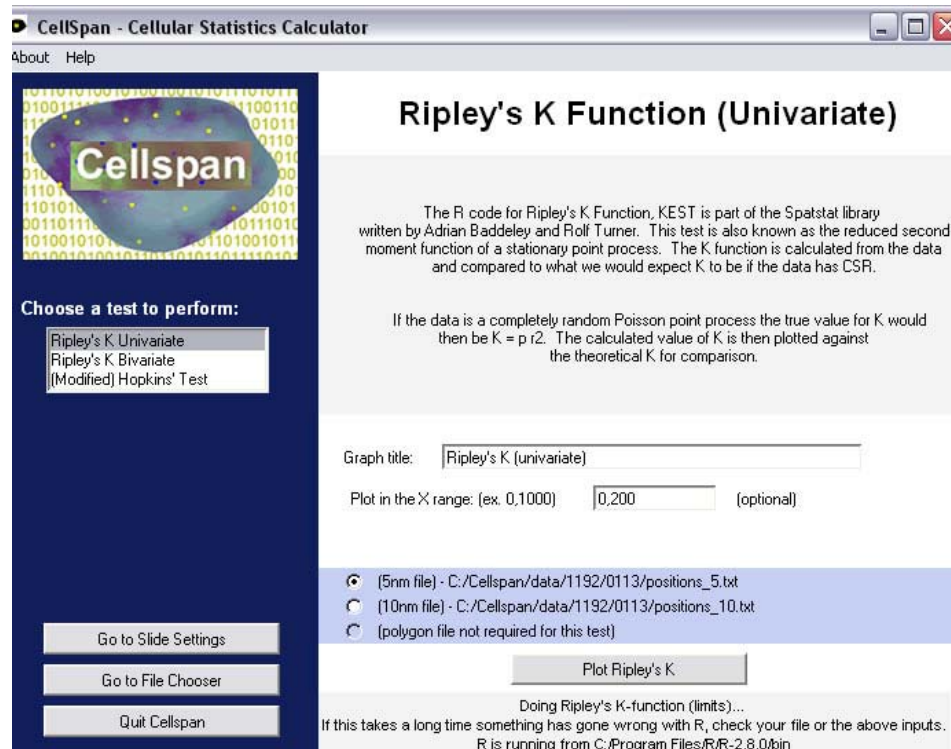


Figure 7.4) Ripley's K Univariate SETTINGS SCREEN.

Figure 7.4 shows the settings screen that Cellspan displays when the user clicks on the name of the Ripley's K univariate test. Cellspan provides a brief description of the Ripley's K test and provides an option to set the horizontal range of the graphical output produced by the R engine. The user may choose to perform the test on either of the two particle datasets (Cellspan can store the "path", or file location, of up to two coordinate data files at once to accommodate the bivariate test). Note the text in the feedback area informing the user that this test shouldn't take very long, and that if it does, something has probably gone wrong. The feedback area also shows the system directory from which Cellspan is running the R-engine. Cellspan automatically finds the installation directory of the R engine on Windows and Debian Linux systems, as long as the user has

performed a standard installation of the R engine (otherwise it displays an error warning in the feedback area).

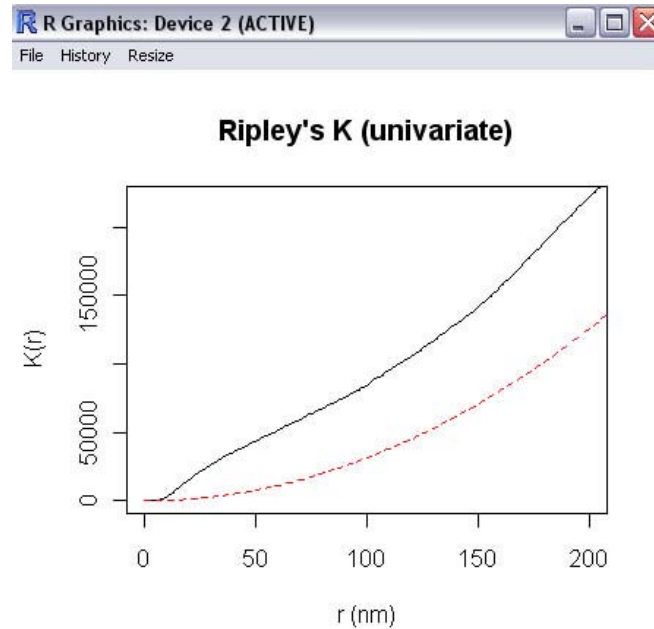


Figure 7.5) Graph of the results of Ripley's K univariate test, generated by the R-engine running as a sub-process of Cellspan

Figure 7.5 is a graph of the output produced by clicking the “plot Ripley's K” button (in Figure 7.4). The black line represents $K(t)$ for the coordinated in the specified data file, where the red line represents the $K(t)$ for a homogenous Poisson point process. The amount of clustering in a given system is related to how far the black line lies above the red line, and is measured by a visual comparative process unique to a given experimental system. Systems are considered more or less clustered by how far the black line lies above the red line, which represents the K function for a system with complete spatial randomness. Clustering at certain specific distance ranges is indicated by local upwards curvatures in the black line. Using the above rules, we can say the above graphs shows that the 5 nm particles (plotted in Figure 7.2) would be considered clustered

relative to a homogenous Poisson point process (and in general), specifically in the range of 10-20 nm (center-to-center particle separation).

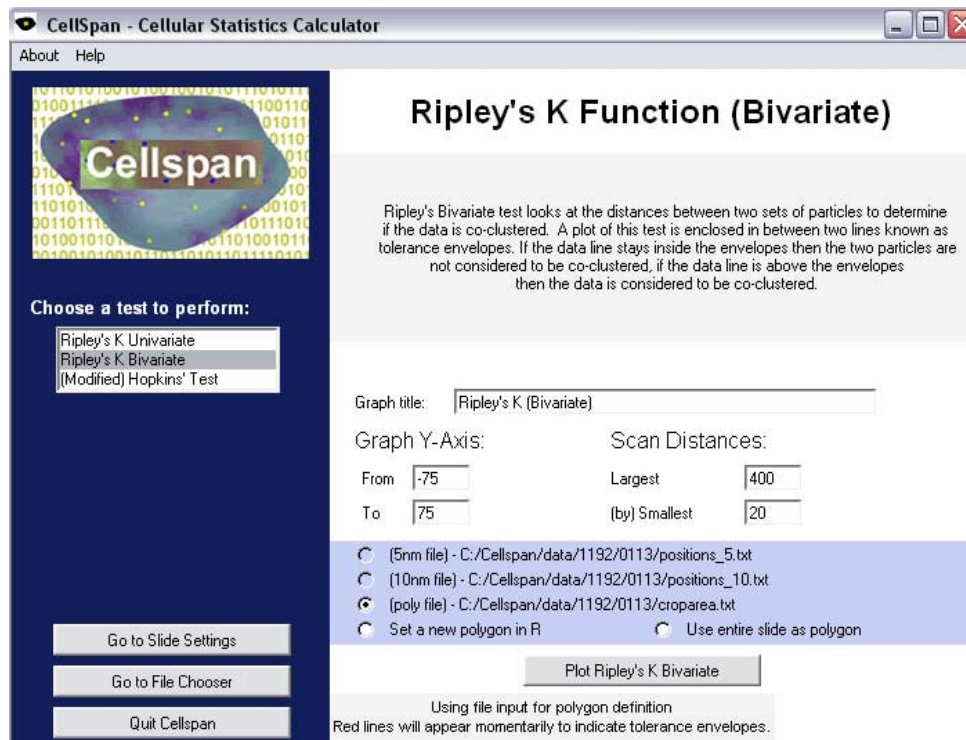


Figure 7.6) Ripley's K bivariate settings screen

Figure 7.6 shows the Cellspan settings screen for the Ripley's K bivariate test. Cellspan presents a brief summary of the test, and allows the user to specify the vertical and horizontal ranges for the graph of the test output. Cellspan incorporates an option here for the user to (optionally) define a new polygon by entering mouse-clicks on top of a plot of the particle positions defining a bounding polygon (in case there is no polygon file or the polygon file has been corrupted), and the option to use the entire slide boundaries as the bounding polygon. These polygon bounding shapes are incorporated into edge-correction algorithms within the code for the statistical functions so that the tests meter clustering versus spatial randomness in a more accurate way. Note the alert in the feedback area warning the user that this test may take an appreciable amount of time,

and that they should wait for red lines (tolerance envelope) to appear over-layed on top of the graph of the Ripley's K function. This test takes approximately 20 seconds on a modern computer, and produces the graphical output of the test results shown in Figure 7.7.

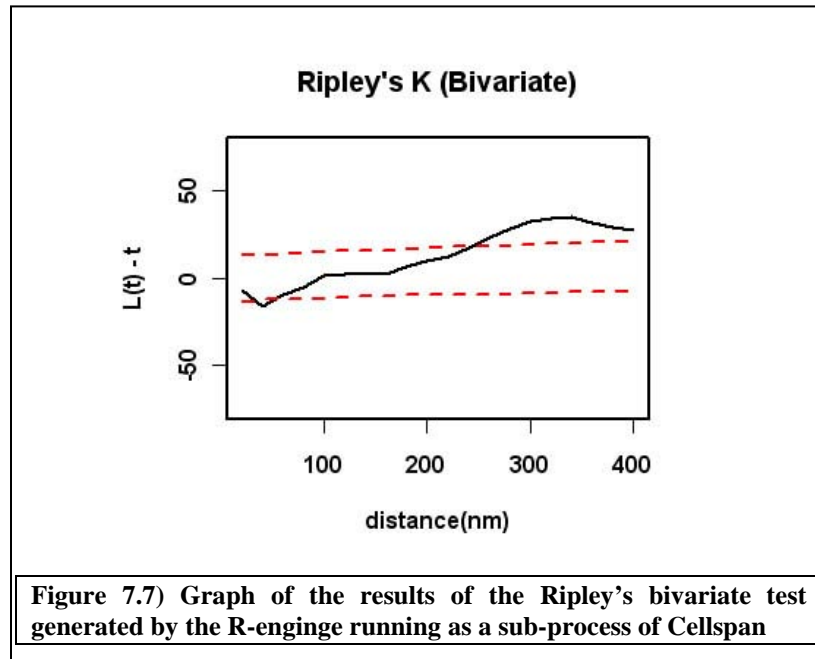


Figure 7.7 shows the graph of the results of the Ripley's K bivariate test applied to the particle positions with bounding polygon (shown in Fig. 7.2). In the bivariate case of the Ripley's K test, the data is considered 'co-clustered' if $K(t)$ (black line) lies above the tolerance envelope (above the top red line). If the particles show co-clustering, then the proteins which they are attached to are posited to be binding and/or interacting within the cell. Confirming such protein interactions and quantifying them in a statistically complete way (via the Ripley's K bivariate test) is a valuable tool for mapping protein pathways. In this example, we observe a general lack of co-clustering among the 5 and 10 nm particles at relevant length scales which are on the order of the particle radii. The fact that the black K-function line is above the tolerance envelope at particle separations

(distances) greater than 200 nm merely indicates that the particles are within the boundaries of the cell, in this instance.

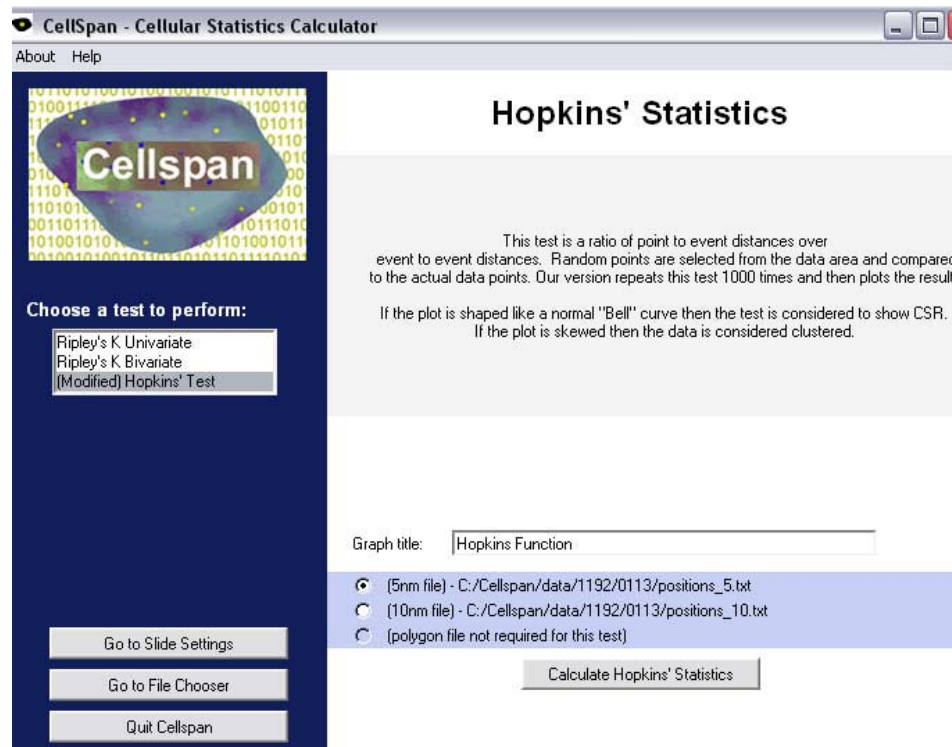


Figure 7.8) Hopkin's test SETTINGS SCREEN

Figure 7.8 shows the Cellspan settings screen for the Hopkins' test. Cellspan provides a brief description of the test and allows the user to select either particle coordinate data file to perform the test on. The bounding polygon data is not relevant in this case. In this settings screen, and the others, Cellspan provides a text box so that the user can enter a custom graph title.

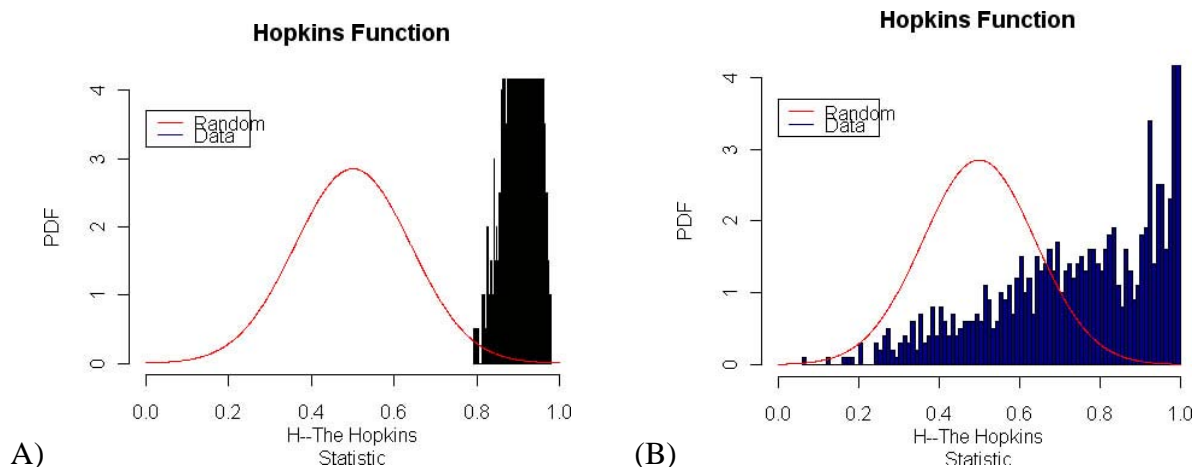


Figure 7.9) Graph of the results of the Hopkins' test for 5 nm particle (A) and 10 nm particle (B) coordinates shown in Fig. 7.2. The Hopkin's statistics is displayed as a normalized histogram (blue in black boxes). The vertical axis is the value of the partial distribution function (PDF) of the point process

Figure 7.9 shows the graphs of results of the Hopkins' test applied to the particle coordinates shown in Fig. 7.2. Cellspan produces histogram plots of “Hopkins' statistic”, a type of partial distribution function. The red, bell-shaped curve represents shape of the Hopkins' statistic histogram for a homogenous Poisson point process, i.e. random particle positions fitting the rules for a hard-core system. When the shape of the histogram is right-shifted relative to the red bell-curve, this indicated the particles are clustered. We observe from the two histograms in Fig. 7.9 that while the 10 nm particles would be considered somewhat clustered, the 5 nm particles would be considered strongly clustered according to the Hopkins' test. The test results displayed in this summary are produced from data chosen which strongly indicate clustering and co-clustering among the 5 nm and 10 nm particles used in this set of coordinate data provided by the UNM Cancer Research Facility (used for Cellspan development / control data / example data). Cellspan can be used to perform statistical tests on any spatial coordinate data, not just cancer cell nanoparticle experiment data, as long as the coordinate and bounding polygon

data files are in the same format (as the example data files provided on the Cellspan website). Cellspan is, however, limited to performing these spatial tests on 2-dimensional datasets.

We have extended the Ripley's K univariate test (using MATLAB) to three dimensions for application to coordinate data from simulations of colloids performed with the *Large-scale Atomic Molecular Massively-Parallel Simulator* (LAMMPS). We instruct LAMMPS to generate coordinate output files (in the .xyz format) at intervals during discrete-element simulations of soft-particle colloids including electrostatic, vdW, hydrodynamic, and polymer/solvent potentials and Brownian thermostating.

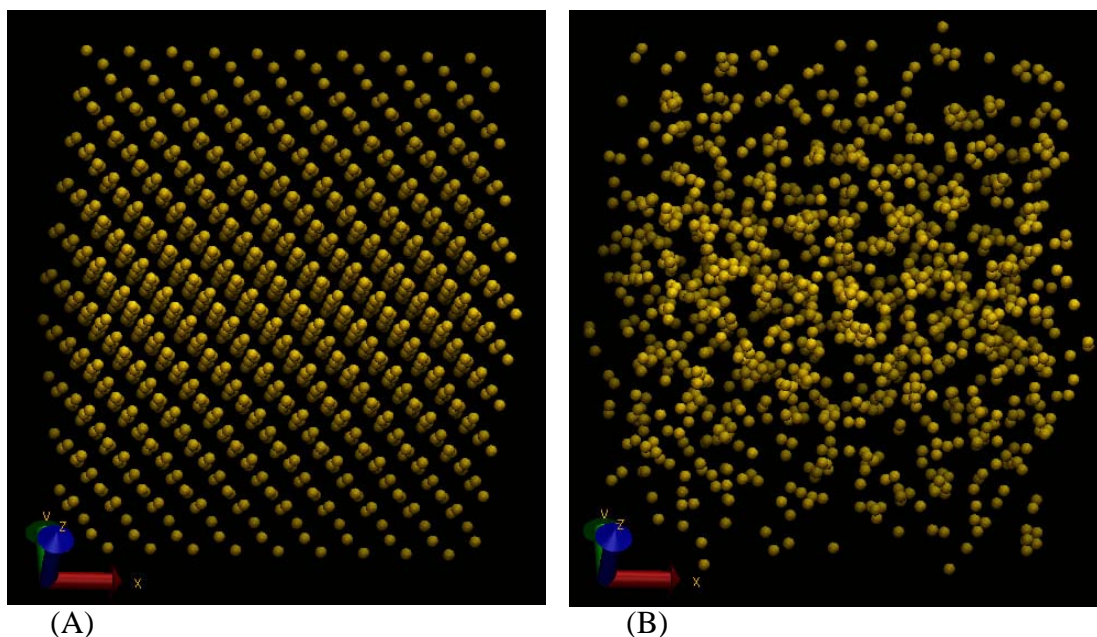


Figure 7.10) Visualization of LAMMPS soft-colloid simulations. The particles are initially set in hexagonally-close packed lattice (HCP) crystal geometry (A), and then allowed to equilibrate at room temperature within a periodic simulation box.

Figure 7.10 shows a visualizations from a soft-colloid equilibration simulation in which particles are allowed to interact with each other and the solvent, where particle motion is driven by Brownian thermal agitation. Figure 7.10 (A) shows the particles in

perfect their initial hexagonally-close-packed geometry, while Figure 7.10 (B) shows that the particles have lost their perfect long-range order and become more randomly oriented. We might postulate from Fig. 7.10 (B) that the particles might be clustered, but the 3D Ripley's K test will allow us to quantify the clustering and make definitive statements about particle clustering in response to simulation dynamics, a useful tool in the field of multiscale directed-assembly of nanoparticle colloids.

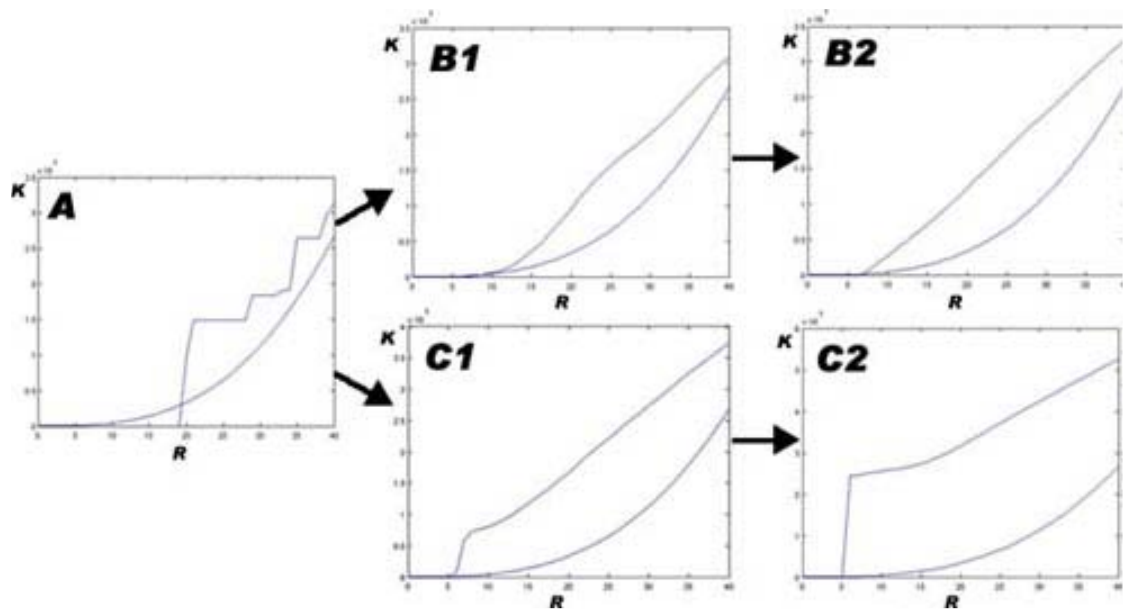


Figure 7.11) A. Ripley K plot for HCP array of NPs B1. Plot for semi-equilibrated system. B1. Plot for equilibrated system. C1. Plot for semi-clustered system. C2. Plot for strongly clustered system

Figure 7.11 (a) illustrates how the K-value (top line) varies in magnitude for radial distances out to 40nm, for the hexagonally close-packed (HCP) array of 6nm particles in periodic 3-space with a lattice constant of 20nm (the system shown in Fig 7.10). The HCP crystal geometry among the particles at the beginning of the simulation is reflected in the jagged K-value line, which indicates regularly spaced neighbors and

absences of neighbors among the particles as would be expected in a system with crystalline order. When this system is allowed to equilibrate, it follows path (b) in Figure 7.11, eventually losing the original form and becoming a straight line upwards, indicating a negligible amount of clustering. When this same simulation is run with the conditions of increasing bulk polymer fraction and increasing viscosity (strong attractive interparticle force, limited mobility), it follows path (c) in Figure 7.11, and the K-values become left-shifted and sharply curved, indicating strong clustering of the particles at 6-7nm.

Appendix (B)

LAMMPS software source code

File Name (Description)		Pages
pair_vincent.h	(Vincent force field header)	156 - 157
pair_vincent.cpp	(Vincent force field)	158 - 167
fix_adapt.h	(variable Adapt command header)	168
fix_adapt.cpp	(variable Adapt command)	169 - 174
in.equil_65	(soft-colloid equilibration simulation deque, 2D, 65% area fract.)	175 - 177

```

/*----- PAIR_VINCENT.h -----*/
/*-----
LAMMPS - Large-scale Atomic/Molecular Massively Parallel Simulator
www.cs.sandia.gov/~sjplimp/lammps.html
Steve Plimpton, sjplimp@sandia.gov, Sandia National Laboratories

Copyright (2003) Sandia Corporation. Under the terms of Contract
DE-AC04-94AL85000 with Sandia Corporation, the U.S. Government retains
certain rights in this software. This software is distributed under
the GNU General Public License.

See the README file in the top-level LAMMPS directory.
----- */
#ifdef PAIR_CLASS

PairStyle(vincent,PairVincent)

#else

#ifndef PAIR_VINCENT_H
#define PAIR_VINCENT_H

#include "pair.h"

namespace LAMMPS_NS {

class PairVincent : public Pair {
public:
  PairVincent(class LAMMPS *);
  ~PairVincent();
  void compute(int, int);
  void settings(int, char **);
  void coeff(int, char **);
  void change(char *, int);
  double init_one(int, int);
  void write_restart(FILE *);
  void read_restart(FILE *);
  void write_restart_settings(FILE *);
  void read_restart_settings(FILE *);
  int pre_adapt(char *, int, int, int, int);
  void adapt(int, int, int, int, double);
  // double single(int, int, int, int, double, double, double, double &);

private:
  double cut_global;
  double **cut,**cut_inner;
  double **a12,**d1,**d2,**diameter,**a1,**a2,**offset;
  double **sigma,**sigma3,**sigma6;
  double **lj1,**lj2,**lj3,**lj4;
  int **form;

  // Here we list the Vincent-force related variables
  // length in m, volume in m^3, molecular weight in g, molecular volume in m^3, density = kg/m^3,
  pressure in J/m^3 (Pa)
  double radi;
  double surfSep;

```

```

double adsorbedLayerThickness; // = 20e-9;      // (m) assume 20 nm adsorbed thickness (for testing)
(should be much less than the particle radius)
double adsorbedSegVolFract; // = 0.14;          // (unitless average vol fract) assumed in Vincent paper to
be approx 0.14
double adsorbedSegMolecWeight; // = 202.397;    // (g/mol) this would be about the molecular weight of
an alkanethiol with 12 carbon, 26 hydrogen, 1 sulfur
double bulkPolyVolFract; // = 0.03;             // (unitless) assumed for some graphs in Vincent paper
double polyDensity; // = 749;                  // (kg/m^3) approximate density of C12H26S alkanethiol
double bulkPolyPenLength; // = 7e-10;          // (m) assume 7 angstrom free polymer penetration length
(for testing)
double solventMolecVol; // = 1.77e-28;         // (m^3) assumed in Rabideau & Bonnecaze (about .177
nm^3, near to the .2 nm^3 assumed in some graphs in Vincent)
double floryChi; // = .3;                      // (unitless) should usually be <= 0.5
double depletionRange; // = 30e-9;            // (m) should be estimate ~ 1.4 times radius of
gyration of polymer (shorter than polymer)
double bulkOsmPress; // = -1168.8156;         // (J/m^3) back-of-envelope calculation given above vars
using eq. (17) from Vincent
double Fdep; // = 0;                          // (J/m) force of depletion effect
double Fsmix; // = 0;                         // (J/m) force of steric mixing
double Fsel; // = 0;                          // (J/m) force of steric elastic repulsion
double FVincent; // = 0;                      // total soft particle potential force
double f1, f2, f3, f4, f5, f6, f7, f8, f9;    // dummy variables used in computing forces
double tempVincent;                          // local temp variable used in computing Vincent forces
double bufferDist;

// not used but mentioned in Vincent's paper, taken care of by Flory-Huggins solution theory
// double bulkPolyMolecWeight; // = 202.397;    // (g/mol) in our test system this will be approx equal
to adsorbed polymer molecular weight

void allocate();
};

}

#endif
#endif

```

```

/*----- PAIR_VINCENT.cpp -----*/
/*-----
LAMMPS - Large-scale Atomic/Molecular Massively Parallel Simulator
http://lammps.sandia.gov, Sandia National Laboratories
Ryan Molecke, reason@unm.edu

Copyright (2003) Sandia Corporation. Under the terms of Contract
DE-AC04-94AL85000 with Sandia Corporation, the U.S. Government retains
certain rights in this software. This software is distributed under
the GNU General Public License.

See the README file in the top-level LAMMPS directory.

test compilation with following line:
mpic++ -O -I/Users/Reason/bin/fftw-2.1.5/include -MMD -MG -DFFT_FFTW -DOMPI_SKIP_MPICXX -
c pair_vincent.cpp

----- */

/*-----
Contributing author: Randy Schunk, prschun@sandia.gov
----- */

#include "math.h"
#include "stdio.h"
#include "stdlib.h"
#include "string.h"
#include "pair_vincent.h"
#include "atom.h"
#include "comm.h"
#include "force.h"
#include "neigh_list.h"
#include "memory.h"
#include "error.h"

using namespace LAMMPS_NS;

#define MIN(a,b) ((a) < (b) ? (a) : (b))
#define MAX(a,b) ((a) > (b) ? (a) : (b))

enum{SMALL_SMALL,SMALL_LARGE,LARGE_LARGE};

/*----- */

PairVincent::PairVincent(LAMMPS *lmp) : Pair(lmp) {
    single_enable = 0;
}

/*----- */

PairVincent::~PairVincent()
{
    if (allocated) {
        memory->destroy_2d_int_array(setflag);
    }
}

```

```

memory->destroy_2d_double_array(cutsq);
memory->destroy_2d_double_array(cut_inner);
memory->destroy_2d_double_array(cut);
memory->destroy_2d_double_array(offset);
// memory->destroy_2d_int_array(form);
// memory->destroy_2d_double_array(a12);
// memory->destroy_2d_double_array(sigma);
// memory->destroy_2d_double_array(d1);
// memory->destroy_2d_double_array(d2);
// memory->destroy_2d_double_array(a1);
// memory->destroy_2d_double_array(a2);
// memory->destroy_2d_double_array(diameter);

// memory->destroy_2d_double_array(sigma3);
// memory->destroy_2d_double_array(sigma6);
// memory->destroy_2d_double_array(lj1);
// memory->destroy_2d_double_array(lj2);
// memory->destroy_2d_double_array(lj3);
// memory->destroy_2d_double_array(lj4);

}
}

/* ----- */

void PairVincent::compute(int eflag, int vflag)
{
    double PI = 3.14159265358979323846; // why do I need this line?
    double Kb = 1.3806503e-23; // (J/K) the Boltzmann constant
    double Avagadro = 6.0214179e23; // (/ mol) the Avagadro constant

    int i,j,ii,jj,inum,jnum,itype,jtype;
    double xtmp, ytmp, ztmp, delx, dely, delz, evdwl, fpair;
    double r, factor_lj;
    int *ilist, *jlist, *numneigh, **firstneigh;

    evdwl = 0.0;
    if (eflag || vflag) ev_setup(eflag, vflag);
    else evflag = vflag_fdotr = 0;

    // fprintf(stderr, "evflag = %d\n", evflag);

    double **x = atom->x;
    double **f = atom->f;
    int *type = atom->type;
    int nlocal = atom->nlocal;

    int nall = nlocal + atom->nghost;
    double *special_lj = force->special_lj;
    int newton_pair = force->newton_pair;

    inum = list->inum;
    ilist = list->ilist;
    numneigh = list->numneigh;

```



```

firstneigh = list->firstneigh;

// fprintf(stderr,"saw inum: %d\n",inum);
// loop over neighbors of my atoms

for (ii = 0; ii < inum; ii++) {
    i = ilit[ii];
    xtmp = x[i][0];
    ytmp = x[i][1];
    ztmp = x[i][2];
    itype = type[i];
    jlist = firstneigh[i];
    jnum = numneigh[i];
    radi = atom->shape[itype][0];
    radi += bufferDist; //this allows you to push force curve in or outwards
    fprintf(stderr,"particle %d (jnum = %d) at %g %g %g\n",i,jnum,x[i][0],x[i][1],x[i][2]);

    for (jj = 0; jj < jnum; jj++) {
        j = jlist[jj];

        if (j < nall) factor_lj = 1.0;
        else {
            factor_lj = special_lj[j/nall];
            j %= nall;
        }

        delx = xtmp - x[j][0];
        dely = ytmp - x[j][1];
        delz = ztmp - x[j][2];
        r = sqrt(pow(delx,2) + pow(dely,2) + pow(delz,2)); // distance between particle centers
        jtype = type[j];

        fprintf(stderr,"r: %g, cutoff: %g\n",r,cut[jtype][jtype]);
        // if (r >= cut[jtype][jtype]) continue; // cutoff distance exceeded?

        //////////////////////////////////////
        //
        // computation of soft particle "Vincent" potential begins here (RM)
        //
        //////////////////////////////////////

        Fdep = 0;
        Fsmix = 0;
        Fsel = 0; // distance between particle centers, r
        surfSep = r - 2*radi; // surface-to-surface separation between particles i,j

        if ( adsorbedLayerThickness < surfSep && surfSep < 2*adsorbedLayerThickness) {
            // use derivative of potential eq. 26 from Vincent '86 for steric mixing force
            // steric elastic force is zero in this case

            f1 = 3*PI*radi*Kb*tempVincent/(5*solventMolecVol);
            f2 = adsorbedSegVolFract/pow(adsorbedLayerThickness,4);
            f3 = 0.5 - floryChi;
            f4 = 2*adsorbedLayerThickness - surfSep;
            f5 = pow(f4,5);

```

```

Fsmix = f1*f2*f3*f5;

} else if (0 < surfSep && surfSep <= adsorbedLayerThickness){
    // use derivative of potential eq. 28 from Vincent '86 for steric mixing force
    // use derivative of potential eq. 29 from Vincent '86 for steric elastic repulsive force

    f1 = -4*PI*radi*pow(adsorbedLayerThickness,2)*Kb*tempVincent/solventMolecVol;
    f2 = pow(adsorbedSegVolFract,2)*(0.5 - floryChi);
    f3 = 1/(2*adsorbedLayerThickness) - 1/surfSep;
    Fsmix = f1*f2*f3;
    //fprintf(stderr,"surfSep: %g, f1: %g, f2: %g, f3: %g, Fsmix: %g\n",surfSep,f1,f2,f3,Fsmix);

    f1 = -
2*PI*radi*Kb*tempVincent*polyDensity*adsorbedSegVolFract*adsorbedLayerThickness/adsorbedSegMolWeight;
    f2 = log(surfSep*pow(3-surfSep/adsorbedLayerThickness,2)/(4*adsorbedLayerThickness));
    Fsel = 1000*Avagadro*f1*f2;
    //fprintf(stderr,"      f1: %g, f2: %g, Fsel: %g\n",f1,f2,Fsel);
}

if ( bulkPolyPenLength <= adsorbedLayerThickness){
    if ( 2*(adsorbedLayerThickness - bulkPolyPenLength) < surfSep && surfSep <
2*(adsorbedLayerThickness + depletionRange - bulkPolyPenLength)){
        //use derivative of potential eq. 23 from Vincent '86 for depletion force

        f1 = 2*PI*radi;
        f2 = bulkOsmPress;
        f3 = depletionRange + adsorbedLayerThickness - bulkPolyPenLength - surfSep/2;
        Fdep = f1*f2*f3;

    } else if ( 0 < surfSep && surfSep <= 2*(adsorbedLayerThickness - bulkPolyPenLength)) {
        //assume depletion force levels out here - modeled for accuracy in Matlab

        f1 = 2*PI*radi;
        f2 = bulkOsmPress;
        f3 = depletionRange;
        Fdep = f1*f2*f3;
    //      fprintf(stderr,"Fdep static region, f1: %g, f2: %g, f3: %g, Fdep: %g\n", f1, f2, f3, Fdep);

    }
} else { // in the case bulkPolyPenLength > adsorbedLayerThickness, different condition for depletion
range
    if ( 0 < surfSep && surfSep < 2*depletionRange) {
        //use derivative of potential eq. 23 from vincent '86 for depletion force (with
adsorbedLayerThickness set = to bulkPolyLength)

        f1 = 2*PI*radi;
        f2 = bulkOsmPress;
        f3 = depletionRange - surfSep/2;
        Fdep = f1*f2*f3;

    }
}
FVincent = Fsmix + Fsel + Fdep;

```

```

        if (FVincent > 1e-9) FVincent = 1e-9;    // THIS IS THE FORCE CUTOFF (can optionally be set by
the user)
        FVincent /= r;
////////////////////////////////////
//
// computation of soft particle "Vincent" potential ends here (RM)
//
////////////////////////////////////

        fpair = FVincent;
//fprintf(stderr,"surfSep: %g, FVincent: %g\n",surfSep,fpair);
//
fprintf(stderr,"evtally(%d,%d,%d,%d,%g,%g,%g,%g,%g,%g)\n",i,j,nlocal,newton_pair,evdwl,0.0,fpair,dex,
dely,delz);

        if (eflag) evdwl *= factor_lj;

        f[i][0] += dex*fpair;
        f[i][1] += dely*fpair;
        f[i][2] += delz*fpair;
//fprintf(stderr,"parrticle %d, x: %g,y: %g,z: %g\n",i,x[i][0],x[i][1],x[i][2]);
//fprintf(stderr,"particle force (particle %d) Fx: %g, Fy: %g, Fz: %g\n",i,f[i][0],f[i][1],f[i][2]);
        if (newton_pair || j < nlocal) {
                f[j][0] -= dex*fpair;
                f[j][1] -= dely*fpair;
                f[j][2] -= delz*fpair;
//fprintf(stderr,"parrticle %d, x: %g,y: %g,z: %g\n",j,x[j][0],x[j][1],x[j][2]);
//fprintf(stderr,"particle force (particle - %d) Fx: %g, Fy: %g, Fz: %g\n",j,f[j][0],f[j][1],f[j][2]);
        }

//fprintf(stderr,"evflag = %d\n",evflag);
        if (evflag){
                ev_tally(i,j,nlocal,newton_pair,evdwl,0.0,fpair,dex,dely,delz);
//                ev_tally(i,j,nlocal,1,evdwl,0.0,fpair,dex,dely,delz);
//
fprintf(stderr,"evtally(%d,%d,%d,%d,%g,%g,%g,%g,%g,%g)\n",i,j,nlocal,newton_pair,evdwl,0.0,fpair,dex,
dely,delz);
        }

        }

        }

        if (vflag_fdotr) virial_compute();
}

/* -----
allocate all arrays
----- */

void PairVincent::allocate()
{
        allocated = 1;
        int n = atom->ntypes;

        setflag = memory->create_2d_int_array(n+1,n+1,"pair:setflag");
        for (int i = 1; i <= n; i++)

```

```

    for (int j = i; j <= n; j++)

setflag[i][j] = 0;
cutsq = memory->create_2d_double_array(n+1,n+1,"pair:cutsq");
cut = memory->create_2d_double_array(n+1,n+1,"pair:cut");
cut_inner = memory->create_2d_double_array(n+1,n+1,"pair:cut_inner");
offset = memory->create_2d_double_array(n+1,n+1,"pair:offset");

}

/* -----
   global settings
   ----- */

void PairVincent::settings(int narg, char **arg)
{
    if (narg != 1 && narg != 0){
//    fprintf(stderr,"saw %d args, %s, %s, %s\n",narg,arg[0],arg[1],arg[2]);
        error->all("Illegal pair style command: wrong number of args for settings() in pairVincent.");
    }
    if (narg == 1){
        tempVincent = atof(arg[0]);
    } else {
        tempVincent = 298;
    }
}

/* -----
   set coeffs for one or more type pairs
   ----- */

void PairVincent::coeff(int narg, char **arg)
{
    double Kb = 1.3806503e-23;           // (J/K) the Boltzmann constant
    if (narg != 12) {
        fprintf(stderr,"saw %d args, %s, %s, %s, %s, %s, %s, %s, %s, %s\n",narg,arg[0],arg[1],arg[2],arg[3],arg[4],arg[5],arg[6],arg[7],arg[8]);
        error->all("Incorrect args for pair coefficients: wrong num coefficient arguments");
    }
    if (!allocated) allocate();

    int ilo,ihi,jlo,jhi;
    force->bounds(arg[0],atom->ntypes,ilo,ihi);
    force->bounds(arg[1],atom->ntypes,jlo,jhi);

//    fprintf(stderr,"saw %d args, %s, %s, %s\n",narg,arg[0],arg[1],arg[2]);
    adsorbedLayerThickness = atof(arg[2]);
    adsorbedSegVolFract = atof(arg[3]);
    adsorbedSegMolecWeight = atof(arg[4]);
    bulkPolyVolFract = atof(arg[5]);
    polyDensity = atof(arg[6]);
    bulkPolyPenLength = atof(arg[7]);
    solventMolecVol = atof(arg[8]);

```

```

floryChi = atof(arg[9]);
depletionRange = atof(arg[10]);
bufferDist = atof(arg[11]);

fprintf(stderr,"thickn: %g, segvolfrac: %g, segmolwgt: %g\nbpolyvolfrac: %g, polydens: %g\nbpolyplen:
%g, solvmvol: %g, fchi: %g, drange: %g, bulkOsmPress:
%g\n",adsorbedLayerThickness,adsorbedSegVolFract,adsorbedSegMolecWeight,bulkPolyVolFract,polyDe
nsity,bulkPolyPenLength,solventMolecVol,floryChi,depletionRange,bulkOsmPress);

// bulkOsmPress = (Kb*tempVincent/solventMolecVol)*(log(1-bulkPolyVolFract) + bulkPolyVolFract -
floryChi*pow(bulkPolyVolFract,2));
// osmotic pressure can be calculated directed (J / m^3)

double cut_one = fmax(adsorbedLayerThickness + depletionRange -
bulkPolyPenLength,2*depletionRange);
int count = 0;
for (int i = ilo; i <= ihi; i++) {
    for (int j = MAX(jlo,i); j <= jhi; j++) {
        cut[i][j] = cut_one;
//printf(stderr,"cut[%d][%d] = %g\n",i,j,cut_one);
        setflag[i][j] = 1;
        count++;
    }
}

if (count == 0) error->all("Incorrect args for pair coefficients (vincent)");
}
/* -----
Hook function for fix_change
----- */
void PairVincent::change(char *arg, int scale)
{
    fprintf(stderr,"fix_change called with args: %s, %d\n",arg,scale);
}

/* -----
init for one type pair i,j and corresponding j,i
----- */

double PairVincent::init_one(int i, int j)
{
    if (setflag[i][j] == 0) {
        cut_inner[i][j] = mix_distance(cut_inner[i][i],cut_inner[j][j]);
        cut[i][j] = mix_distance(cut[i][i],cut[j][j]);
    }

    cut_inner[j][i] = cut_inner[i][j];

    return cut[i][j];
}

/* -----
proc 0 writes to restart file
----- */

```

```

void PairVincent::write_restart(FILE *fp)
{
    write_restart_settings(fp);

    int i,j;
    for (i = 1; i <= atom->ntypes; i++)
        for (j = i; j <= atom->ntypes; j++) {
            fwrite(&setflag[i][j],sizeof(int),1,fp);
            if (setflag[i][j]) {
                fwrite(&cut[i][j],sizeof(double),1,fp);
            }
        }
}

/* -----
   proc 0 reads from restart file, bcasts
   ----- */

void PairVincent::read_restart(FILE *fp)
{
    read_restart_settings(fp);
    allocate();

    int i,j;

    for (i = 1; i <= atom->ntypes; i++)
        for (j = i; j <= atom->ntypes; j++) {
            if (comm->me == 0) fread(&setflag[i][j],sizeof(int),1,fp);
            MPI_Bcast(&setflag[i][j],1,MPI_INT,0,world);
            if (setflag[i][j]) {
                if (comm->me == 0) {
                    fread(&cut[i][j],sizeof(double),1,fp);
                }
                MPI_Bcast(&cut[i][j],1,MPI_DOUBLE,0,world);
            }
        }
}

/* -----
   proc 0 writes to restart file
   ----- */

void PairVincent::write_restart_settings(FILE *fp)
{
    fwrite(&cut_global,sizeof(double),1,fp);
    fwrite(&offset_flag,sizeof(int),1,fp);
    fwrite(&mix_flag,sizeof(int),1,fp);
}

/* -----
   proc 0 reads from restart file, bcasts
   ----- */

void PairVincent::read_restart_settings(FILE *fp)
{

```

```

int me = comm->me;
if (me == 0) {
    fread(&cut_global,sizeof(double),1,fp);
    fread(&offset_flag,sizeof(int),1,fp);
    fread(&mix_flag,sizeof(int),1,fp);
}
MPI_Bcast(&cut_global,1,MPI_DOUBLE,0,world);
MPI_Bcast(&offset_flag,1,MPI_INT,0,world);
MPI_Bcast(&mix_flag,1,MPI_INT,0,world);
}

/* ----- */

// double PairVincent::single() {}

/* -----
check if name is recognized, return integer index for that name
if name not recognized, return -1
if type pair setting, return -2 if no type pairs are set
----- */

int PairVincent::pre_adapt(char *name, int ilo, int ihi, int jlo, int jhi)
{
    int count = 0;
    for (int i = ilo; i <= ihi; i++)
        for (int j = MAX(jlo,i); j <= jhi; j++)
            count++;
    if (count == 0) return -2;
    if (strcmp(name,"adsorbedLayerThickness") == 0) return 2;
    if (strcmp(name,"adsorbedSegVolFract") == 0) return 3;
    if (strcmp(name,"adsorbedSegMolecWeight") == 0) return 4;
    if (strcmp(name,"bulkPolyVolFract") == 0) return 5;
    if (strcmp(name,"polyDensity") == 0) return 6;
    if (strcmp(name,"bulkPolyPenLength") == 0) return 7;
    if (strcmp(name,"solventMolecVol") == 0) return 8;
    if (strcmp(name,"floryChi") == 0) return 9;
    if (strcmp(name,"depletionRange") == 0) return 10;
    if (strcmp(name,"bufferDist") == 0) return 11;
    return -1;
}

/* -----
adapt parameter indexed by which
change all pair variables affected by the reset parameter
if type pair setting, set I-J and J-I coeffs
----- */

void PairVincent::adapt(int which, int ilo, int ihi, int jlo, int jhi, double value)
{
    double Kb = 1.3806503e-23;          // (J/K) the Boltzmann constant
    switch ( which ) {
        case 2:
            adsorbedLayerThickness = value;
            break;
        case 3:
            adsorbedSegVolFract = value;

```

```

break;
case 4:
    adsorbedSegMolecWeight = value;
break;
case 5:
    bulkPolyVolFract = value;
    bulkOsmPress = (Kb*tempVincent/solventMolecVol)*(log(1-bulkPolyVolFract) + bulkPolyVolFract -
floryChi*pow(bulkPolyVolFract,2));
    break;
case 6:
    polyDensity = value;
break;
case 7:
    bulkPolyPenLength = value;
break;
case 8:
    solventMolecVol = value;
    bulkOsmPress = (Kb*tempVincent/solventMolecVol)*(log(1-bulkPolyVolFract) + bulkPolyVolFract -
floryChi*pow(bulkPolyVolFract,2));
    break;
case 9:
    floryChi = value;
    bulkOsmPress = (Kb*tempVincent/solventMolecVol)*(log(1-bulkPolyVolFract) + bulkPolyVolFract -
floryChi*pow(bulkPolyVolFract,2));
    break;
case 10:
    depletionRange = value;
break;
case 11:
    bufferDist = value;
break;
}
}

```



```

/*----- FIX_ADAPT.h -----*/
/* -----
LAMMPS - Large-scale Atomic/Molecular Massively Parallel Simulator
http://lammps.sandia.gov, Sandia National Laboratories
Steve Plimpton, sjplimp@sandia.gov

Copyright (2003) Sandia Corporation. Under the terms of Contract
DE-AC04-94AL85000 with Sandia Corporation, the U.S. Government retains
certain rights in this software. This software is distributed under
the GNU General Public License.

See the README file in the top-level LAMMPS directory.
----- */

#ifdef FIX_CLASS

FixStyle(adapt,FixAdapt)

#else

#ifndef LMP_FIX_ADAPT_H
#define LMP_FIX_ADAPT_H

#include "fix.h"

namespace LAMMPS_NS {

class FixAdapt : public Fix {
public:
  FixAdapt(class LAMMPS *, int, char **);
  ~FixAdapt();
  int setmask();
  void init();
  void pre_force(int);

private:
  int nadapt;
  int *which;
  char **pair,**param,**var;
  int *ilo,*ihi,*jlo,*jhi;

  int *ivar;
  class Pair **pairptr;
  int *pairindex;
  int *awhich;
};

}

#endif
#endif

```

```

/*----- FIX_ADAPT.cpp -----*/
/* -----
LAMMPS - Large-scale Atomic/Molecular Massively Parallel Simulator
http://lammps.sandia.gov, Sandia National Laboratories
Steve Plimpton, sjplimp@sandia.gov

Copyright (2003) Sandia Corporation. Under the terms of Contract
DE-AC04-94AL85000 with Sandia Corporation, the U.S. Government retains
certain rights in this software. This software is distributed under
the GNU General Public License.

See the README file in the top-level LAMMPS directory.
----- */

#include "math.h"
#include "string.h"
#include "stdlib.h"
#include "fix_adapt.h"
#include "atom.h"
#include "force.h"
#include "pair.h"
#include "input.h"
#include "variable.h"
#include "error.h"

using namespace LAMMPS_NS;

enum{PAIR,ATOM};
enum{DIAMETER};

/* ----- */

FixAdapt::FixAdapt(LAMMPS *lmp, int nargs, char **arg) : Fix(lmp, nargs, arg)
{
  if (nargs < 4) error->all("Illegal fix adapt command1");
  nevery = atoi(arg[3]);
  if (nevery <= 0) error->all("Illegal fix adapt command2");

  // count # of adaptations

  nadapt = 0;

  int iarg = 4;
  while (iarg < nargs) {
    if (strcmp(arg[iarg],"pair") == 0) {
      if (iarg+6 > nargs) error->all("Illegal fix adapt command: wrong number of args");
      nadapt++;
      iarg += 6;
    } else if (strcmp(arg[iarg],"atom") == 0) {
      if (iarg+3 > nargs) error->all("Illegal fix adapt command");
      nadapt++;
      iarg += 3;
    } else error->all("Illegal fix adapt command3");
  }

  // allocate per-adapt vectors

```

```

which = new int[nadapt];
pair = new char*[nadapt];
param = new char*[nadapt];
ilo = new int[nadapt];
ihi = new int[nadapt];
jlo = new int[nadapt];
jhi = new int[nadapt];
var = new char*[nadapt];
ivar = new int[nadapt];
pairptr = new Pair*[nadapt];
pairindex = new int[nadapt];
awhich = new int[nadapt];

// parse keywords

nadapt = 0;

iarg = 4;
while (iarg < nargs) {
  if (strcmp(arg[iarg], "pair") == 0) {
    if (iarg+6 > nargs) error->all("Illegal fix adapt command: didn't see pair declaration");
    which[nadapt] = PAIR;
    int n = strlen(arg[iarg+1]) + 1;
    pair[nadapt] = new char[n];
    strcpy(pair[nadapt], arg[iarg+1]);
    n = strlen(arg[iarg+2]) + 1;
    param[nadapt] = new char[n];
    strcpy(param[nadapt], arg[iarg+2]);
    fprintf(stderr, "param = %s\n", param[nadapt]);
    force->bounds(arg[iarg+3], atom->ntypes, ilo[nadapt], ihi[nadapt]);
    force->bounds(arg[iarg+4], atom->ntypes, jlo[nadapt], jhi[nadapt]);
    n = strlen(arg[iarg+5]) + 1;
    var[nadapt] = new char[n];
    strcpy(var[nadapt], arg[iarg+5]);
    nadapt++;
    iarg += 6;
  } else if (strcmp(arg[iarg], "atom") == 0) {
    if (iarg+3 > nargs) error->all("Illegal fix adapt command");
    which[nadapt] = ATOM;
    int n = strlen(arg[iarg+1]) + 1;
    param[nadapt] = new char[n];
    strcpy(param[nadapt], arg[iarg+1]);
    n = strlen(arg[iarg+2]) + 1;
    var[nadapt] = new char[n];
    strcpy(var[nadapt], arg[iarg+2]);
    nadapt++;
    iarg += 3;
  } else error->all("Illegal fix adapt command4");
}
}

/* ----- */

FixAdapt::~FixAdapt()
{

```

```

for (int i = 0; i < nadapt; i++) {
    if (which[i] == PAIR) delete [] pair[i];
    delete [] param[i];
    delete [] var[i];
}
delete [] which;
delete [] pair;
delete [] param;
delete [] ilo;
delete [] ihi;
delete [] jlo;
delete [] jhi;
delete [] var;
delete [] ivar;
delete [] pairptr;
delete [] pairindex;
delete [] awhich;
}

/* ----- */

int FixAdapt::setmask()
{
    int mask = 0;
    mask |= PRE_FORCE;
    return mask;
}

/* ----- */

void FixAdapt::init()
{
    // error checks

    for (int m = 0; m < nadapt; m++) {
        if (which[m] == PAIR) {
            pairptr[m] = force->pair_match(pair[m],1);
            if (pairptr[m] == NULL)
                error->all("Fix adapt pair style does not exist");
            pairindex[m] =
                pairptr[m]->pre_adapt(param[m],ilo[m],ihi[m],jlo[m],jhi[m]);
            if (pairindex[m] == -1)
                error->all("Fix adapt pair parameter is not recognized");
            if (pairindex[m] == -2)
                error->all("Fix adapt pair types are not valid");

        } else if (which[m] == ATOM) {
            if (strcmp(param[m],"diameter") == 0) {
                awhich[m] = DIAMETER;
                if (!atom->radius_flag)
                    error->all("Fix adapt requires atom attribute radius");
            } else error->all("Fix adapt atom attribute is not recognized");
        }
    }

    // fprintf(stderr,"var[m] = %s\n",var[m]);
    ivar[m] = input->variable->find(var[m]);
}

```

```

    if (ivar[m] < 0) error->all("Variable name for fix adapt does not exist");
    if (!input->variable->equalstyle(ivar[m]))
        error->all("Variable for fix adapt is not equal style");
}

// set params to values for initial force calculation
// needs to happen here in init() instead of setup()
// because modify->setup() is called after pre-Verlet forces are computed

pre_force(0);
}

/* ----- */

void FixAdapt::pre_force(int vflag)
{
    for (int m = 0; m < nadapt; m++) {
        double value = input->variable->compute_equal(ivar[m]);

        if (which[m] == PAIR)
            pairptr[m]->adapt(pairindex[m],ilo[m],ihi[m],jlo[m],jhi[m],value);

        else if (which[m] == ATOM) {

            // set radius from diameter
            // set rmass if both rmass and density are defined

            if (awhich[m] == DIAMETER) {
                int mflag = 0;
                if (atom->rmass_flag && atom->density_flag) mflag = 1;
                double PI = 4.0*atan(1.0);

                double *radius = atom->radius;
                double *rmass = atom->rmass;
                double *density = atom->density;
                int *mask = atom->mask;
                int nlocal = atom->nlocal;

                for (int i = 0; i < nlocal; i++)
                    if (mask[i] & groupbit) {
                        radius[i] = 0.5*value;
                        rmass[i] = 4.0*PI/3.0 * radius[i]*radius[i]*radius[i] * density[i];
                    }
            }
        }
    }
}

```

```

#----- in.equil_65 -----#
# Colloidal 5.5nm diameter Gold coated with 12C alkane in Toluene with solvated PMMA
# Ryan Molecke    <3 Feb 14, 2011 <3

dimension 2
boundary p p p
units      si
atom_style ellipsoid
neighbor   3e-8 bin
neigh_modify delay 5

lattice    hex 6.496592e-9 origin 0.25 0.25 0 #65% AF
##### lattice spacing = radius * sqrt( 2 * pi / ( area_fraction * sqrt(3) ) )

# 5% AF: 23.42379 nm lattice
# 10% AF: 16.56312 nm lattice
# 15% AF: 13.52373 nm lattice
# 20% AF: 11.71189 nm lattice
# 25% AF: 10.47544 nm lattice
# 30% AF: 9.562725 nm lattice
# 35% AF: 8.853363 nm lattice
# 40% AF: 8.281563 nm lattice
# 45% AF: 7.807932 nm lattice
# 50% AF: 7.407255 nm lattice
# 55% AF: 7.062540 nm lattice
# 60% AF: 6.761868 nm lattice
# 65% AF: 6.496592 nm lattice
# 70% AF: 6.260273 nm lattice
# 75% AF: 6.047998 nm lattice
# 80% AF: 5.855949 nm lattice

region      box prism 0 31 0 18 -0.25 0.25 0 0 0 # this needs to fill a 200x200 or 300x300 nm box for
GISAXS (NANODIFT)
create_box  1 box
create_atoms 1 box

# 4*pi*r^3/3*19.3*1e6 (density of gold is 19.3g/cc, factor of 1e6 converts to cancel m^3)
mass        1 1.6812953e-18

# Shape Definition (x,y,z diameters of ellipsoid)
# calculated to match DLVO "hard-sphere" and vincent potential at 0 surfsep
shape       1 4.8e-9 4.8e-9 4.8e-9

#Specification of pair Parameters
pair_style  hybrid/overlay vincent 298 colloid 8e-9 lubricate2 554.2e-5 0 5.5e-9 8e-9 brownian 554.2e-5 0
5.5e-9 8e-9 298 944821 # 5.5nm AUNP, 298K toluene
pair_coeff  * * vincent 1.6865e-9 0.13 202.397 0.08 202.397 749 3e-10 1.77e-28 0.45 1e-9 3.42e-10 #
12C alkanethiolated, in toluene/PMMA
pair_coeff  * * colloid 2.5e-19 1.7875e-9 4.8e-9 4.8e-9 8e-9
# yukawa/colloid 5.959e6 3e-8
#pair_coeff  * * yukawa/colloid 2.37e-15 8e-9 # calculated from Grahm equation (not working / not
relevant in this case)
pair_coeff  * * lubricate2
pair_coeff  * * brownian

communicate single vel yes

```

```

velocity    all create 298 97287
fix         1 all nve/asphere
fix         3 all rdf 500000 /nano/scratch/reason/rdf.equil_65 3e-8 30 1 1
fix         6 all enforce2d
thermo      50

thermo_style    custom step temp epair etotal press pxy

timestep 1e-11
dump      3 all xyz 4000 /nano/scratch/reason/equil_65.xyz
run       2000000

```

```

# Colloidal 5.5nm diameter Gold coated with 12C alkane in Toluene with solvated PMMA
# 3D simulation
# Ryan Molecke June 29, 2010

# from 001.jpg from shisheng: 10px = 5.5nm -> .55 nm/px
# image size = 432x302 = 237.6nm x 166.1nm -> 39,465.36 nm^2 total area -> 3.946536e-14 m^2
# image contains 1101 particles, each having area pi*(2.75nm)^2
# total area of particles = 2.615788e-14 m^2
# area fraction = 0.6628 or 66.28%

boundary p p f
units      si
atom_style ellipsoid
neighbor   8e-9 bin
neigh_modify delay 5

lattice    hcp 30e-9 origin 0.25 0.25 0.25
region     box prism 0 16 0 10 0 20 0 0 0
create_box 1 box
create_atoms 1 box

# 4*pi*r^3/3*19.3*1e6 (density of gold is 19.3g/cc factor of 1e6 converts to cancel m^3)
mass       1 1.6812953e-18

# Shape Definition (x,y,z diameters of ellipsoid)
# calculated to match DLVO "hard-shere" and vincent potential at 0 surfsep
shape      1 4.8e-9 4.8e-9 4.8e-9

#operating parameters
#variable   srate equal 1

#Specification of pair Parameters (see notes from lab notebook, June 8, 2010)
pair_style  hybrid/overlay vincent 298 colloid 8e-9 lubricate2 554.2e-5 0 5.5e-9 8e-9 brownian 554.2e-5 0
5.5e-9 8e-9 298 945821 # 5.5nm AUNP, 298K toluene
pair_coeff  * * vincent 1.6865e-9 0.1 202.397 0.08 202.397 749 3e-10 1.77e-28 0.1 1e-9 3.42e-10 # 12C
alkanethiolated, in toluene/PMMA
pair_coeff  * * colloid 2.5e-19 1.7875e-9 4.8e-9 4.8e-9 8e-9
# yukawa/colloid 5.959e6 3e-8
#pair_coeff  * * yukawa/colloid 2.37e-15 8e-9 # calculated from Grahm equation (not working / not
relevant in this case)
pair_coeff  * * lubricate2
pair_coeff  * * brownian

communicate single vel yes #enables ghost atoms to store velocity (for multiprocessor runs)
#####
#####

velocity    all create 298 97287
fix         1 all nve/asphere
fix         2 all wall/colloid zlo zlo 3.5e-19 0.48e-9 7e-9 zhi 980e-9 3.5e-19 0.48e-9 7e-9 units box
# this is the bottom (water) wall
dump        3 all xyz 20000 evap_test.xyz
fix         3 all rdfr 500000 rdf.evap_test 4e-8 400 1 1
compute     9 all msd
thermo_style custom step c_9[4] temp epair etotal
thermo      250

```



```

timestep      1e-11
run           1000000 # system equilibration

# now we set dynamically changing boundary, viscosity, bulk polymer vol fract, and chi params
# this simulates evaporation of toluene/PMMA into a thin film on the surface of water

# below lines set dynamic viscosity
#viscosity at beginning: 554.2e-6 kg/(m*s) or (Pa*s) => 554.2e-5 (p)
variable      visci equal 554.2e-5      #this is the reported viscosity value for toluene
variable      viscf equal 50*${visci}    #this is the desired final viscosity
variable      equilsteps equal 1000000   #set this value to the number of steps used above for equil.
variable      numsteps equal 20000000    #number of steps for next phase, used for all dynamic variables
variable      newvisc equal ${visci}+(step/${numsteps})*(${viscf}-${visci})
#parabolic progression of viscosity
fix           11 all adapt 1000 pair lubricate2 mu 1 1 newvisc pair brownian mu 1 1 newvisc

# below lines set dynamic bulk polymer volume fraction (bpvf)
variable      bpvfi equal 0.08
variable      bpvff equal 0.75
variable      newbpvf equal ${bpvfi}+(step-${equilsteps})*(${bpvff}-${bpvfi})/${numsteps} #linear
progression of bulk poly vol fract
fix           12 all adapt 1000 pair vincent bulkPolyVolFract 1 1 newbpvf

#below lines set dynamic Flory Chi
variable      chii equal 0.1
variable      chif equal 0.4
variable      newchi equal ${chii}+(step-${equilsteps})*($^{108}-${chii})/${numsteps} #linear progression
of chi
fix           13 all adapt 1000 pair vincent floryChi 1 1 newchi

#below line controls moving (top) air wall
fix           22 all wall/colloid zhi 980e-9 3.5e-19 0.48e-9 7e-9 vel 0.0046 units box # this is the
moving (air) wall

dump_modify   3 every 10000
run           20000000 # evaporation phase

```